12-2-2015

High Speed All Optical Switching and Encryption using Ultrafast Devices

Wenbo Li
University of Connecticut, liwenbo625@gmail.com

High Speed All Optical Switching and Encryption using Ultrafast Devices

Wenbo Li, Ph.D.
University of Connecticut, 2015

The next generation of fiber-optic communication system demands ultra-high speed data processing and switching components. Conventional electro-optical parts have reached their bottleneck both speed-wise and efficiency-wise. The idea of manipulating high speed data in all-optical domain is gaining more popularity. In this PhD dissertation, I showed the design and performance analysis of two kinds of ultra-fast all-optical latches, Set-Reset latch and D-flip-flop, based on two different schemes: (1) cross gain and phase modulation (XGM and XPM) in quantum dot semiconductor optical amplifiers (QD-SOA) and (2) two-photon absorption (TPA) in bulk semiconductor optical amplifiers. Design and simulation of a scheme to realize high speed all-optical encryption and decryption using key-stream generators and XOR gates based on QD-SOA are included in this dissertation. We also proposed and simulated all-optical Boolean logic functions with improved output quality using binary phase shift keyed signal based on QD-SOA. A fiber ring laser system with charcoal nano-particles as saturable absorber inside the cavity has been designed and experimentally demonstrated. This fiber ring laser system can generate optical pulse train @ 20Gb/s with improved stability and smaller pulse width comparing with the system without nano-particles in the cavity.

High Speed All Optical Switching and Encryption using Ultrafast Devices

Wenbo Li

B.S., Harbin Institute of Technology, Harbin, China, 2009

M.S., Harbin Institute of Technology, Harbin, China, 2011

A Dissertation

Submitted in Partial Fulfillment of the

Requirements for the Degree of

Doctor of Philosophy

at the

University of Connecticut

2015

APPROVAL PAGE

Doctor of Philosophy Dissertation

High Speed All Optical Switching and Encryption using Ultrafast Devices

Presented by

Wenbo Li, B.S., M.S.

Major Advisor_____

Niloy K. Dutta

Associate Advisor_____

Gayanath Fernando

Associate Advisor_____

Boris Sinkovic

University of Connecticut

2015

Acknowledgement

I would like to first send my deepest gratitude to my major advisor, Dr. Niloy K. Dutta, for his guidance, encouragement and understanding during my graduate studies in the University of Connecticut. Not only had he taught me knowledge and skills crucial for my career, but the creativity and problem-solving ability as well. More importantly, Dr. Dutta showed me the importance of concentrating on what matters most at different stage of my life. What I learned from his sparking wit and cheerful nature will benefit my whole life.

I would like to thank my associate advisors Dr. Gayanath Fernando and Dr. Boris Sinkovic for their time, extreme patience, many motivational discussions and comments on my doctoral dissertation. I would also thank all my committee members Dr. William Hines and Dr. Peter Schweitzer.

I would like to thank the group members both current and former in Dr. Dutta's group. In particular, I would like to thank Dr. Shaozhen Ma who is my mentor. Working with him and all the discussion with him inspired me a lot in my own research. Without his help, I wouldn't be able to get started with the research quickly. I would also like to thank Mr. Hongyu Hu and Mr. Xiang Zhang. Working with you smart and hardworking scientists had been an unforgettable memory for me. It's always pleasure to discuss problems with these two excellent scientists.

I would like to thank all my friends in the physics department, Shu Di, Zhiwei zhang, Shiqi Yin, Yiteng Tian, Zhihai Zhu, Yi Li, Cheng Tu, Jia wang, and Marko Gacesa. My conversations with them, whether were personal or scientific, have also benefited me in many ways.

Finally and most importantly, I would like to thank my family for their support and care. In order for me to concentrate on my studies in the US, my parents took my part of family responsibilities all on their shoulders, I know I can never make up for their sacrifice and love they gave me. I also want to thank my girlfriend Shuai, for her love, encouragement and sacrifice. She was amazing.

TABLE OF CONTENTS

Chapter 1 Introduction

This introductory chapter is intended to provide an overview of fiber optic communication and optical switching technologies. Section 1.1, a brief history of fiber optic communications will be provided. Section 1.2 discussed the advance of optical switching technologies which are used in communication system. In section 1.3, a brief overview of the entire thesis work will be introduced.

1.1. A Brief History of Fiber Optic Communications

Fiber optic communication is a method of transmitting information from one place to another by sending pulses of light through an optical fiber. First developed in the 1970s, fiber optic communication systems have revolutionized the telecommunications industry and have played a major role in the advent of the information age.

In 1966 Charles K. Kao and George Hockham proposed optical fibers at STC Laboratories at Harlow, England and they showed the losses in existing glass was due to contaminants which could potentially be removed. Intrigued by Kao and Hockham's proposal, a breakthrough occurred in 1970 when the fiber loss could be reduced to about 20dB/km in the wavelength region near 1μm [1]. At about the same time, GaAs semiconductor lasers, operating continuously at room temperature, were demonstrated [2]. The simultaneous availability of a

compact optical source and a low-loss optical fiber led to a worldwide effort for developing fiber-optic communication systems. Fiber optic communication developed over the years in a series of generations that can be closely tied to wavelength. Figure 1.1 shows the transmission windows for fiber optic communication system and losses for the three generations of fibers. The top, dashed, curve corresponds to early 1980's; the middle, dotted, curve corresponds to late 1980's fiber, and the bottom, solid, curve corresponds to modern optical fibers.

Fiber optic communication systems have five generations of development since its first implementation. The first-generation lightwave systems operating near 0.8μm became available in 1980 [3]. They operated at a bit rate of 45Mb/s and allowed a repeater spacing of about 10km. The second generation of fiber optic communication system was developed for commercial use in the early 1980s, operated at 1.3μm, and used InGaAsP semiconductor lasers. However, the bit rate of early systems was limited to below 100Mb/s because of dispersion in multimode fibers [4]. This limitation was overcome by the use of single-mode fibers. By 1987, second-generation 1.3μm ligthwave systems, operating at bit rates up to 1.7Gb/s with a repeater spacing of about 50km, were commercially available. The introduction of third-generation optic communication system operating at 1.55μm with losses about 0.2dB/km was considerably delayed by larger fiber dispersion near 1.55μm. Scientists overcame this difficulty by using dispersion-shifted fibers designed to have minimal dispersion at 1.55μm or by limiting the laser spectrum to a single longitudinal mode. These developments eventually allowed third-generation systems to operate commercially at 2.5Gb/s with repeater spacing in excess of 100km. The fourth generation of optic

communication systems make use of optical amplification for increasing the repeater spacing and of wavelength-division multiplexing (WDM) for increasing the bit rate [5]. These two improvements caused a revolution that resulted in the doubling of system capacity every 6 months starting in 1992 until a bit rate of 10Tb/s was reached by 2001. The fifth generation of fiber-optic communication systems is concerned with extending the wavelength range over which a WDM system can operate and finding a solution to the fiber-dispersion problem. The conventional wavelength window convers the wavelength range 1.53-1.57μm and dry fiber has a low-loss window promising an extension of that range to 1.30-1.65μm. In addition, several dispersion-compensation techniques have been developed to solve fiber-dispersion problem. One solution is based on the concept of optical solitions, optical pulses that preserve their shape during propagation in a lossless fiber by counteracting the effect of dispersion through the fiber nonlinearity. The fiber transmission capacity has grown by a factor of 10^9 in the last three decades through technology breakthrough such as low loss single mode fiber, EDEA, WDM, coherent transmission and space-division multiplexing (SDM). Figure 1.2 illustrates this trend.

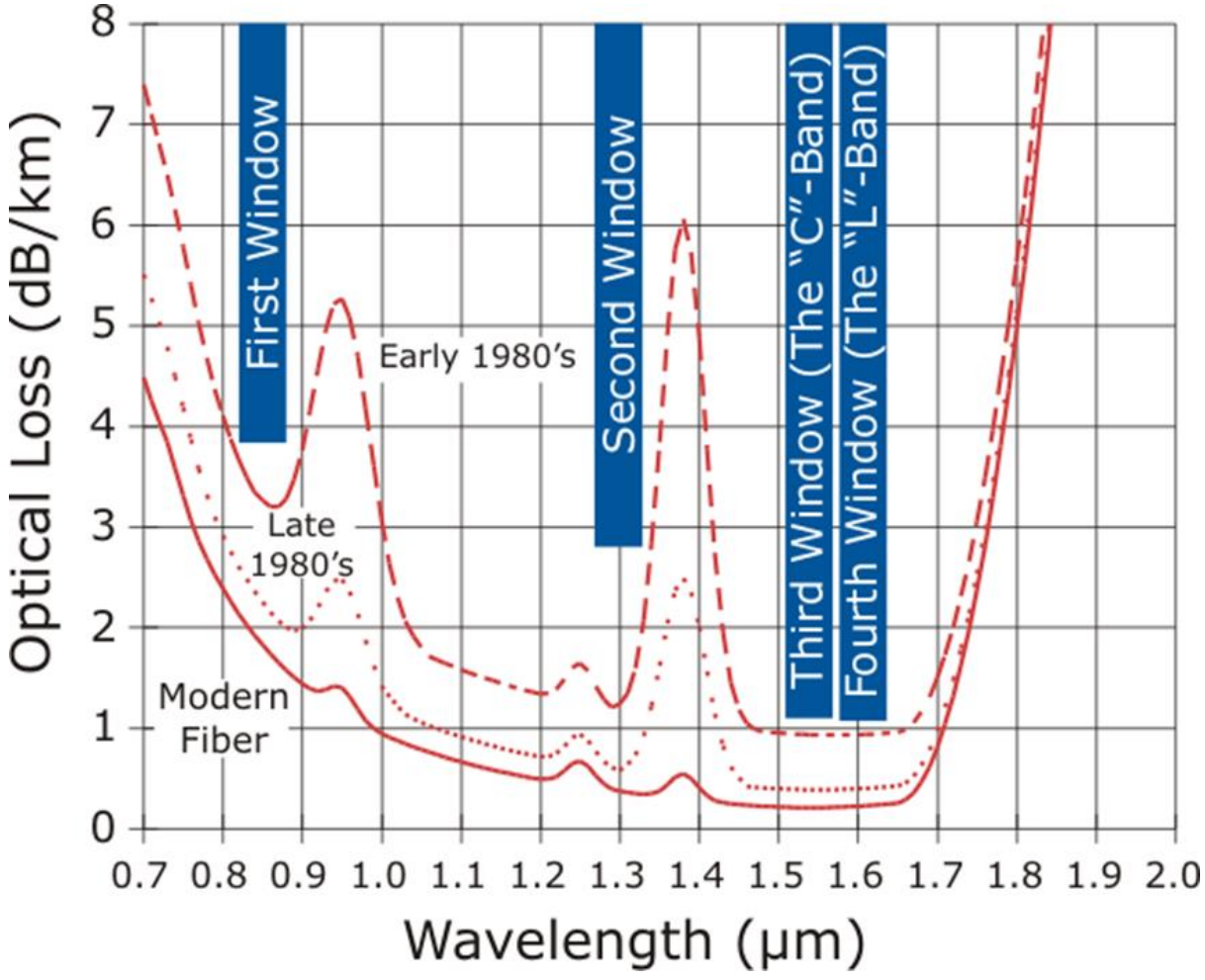

Figure 1.1 The transmission windows of silica optical fibers.

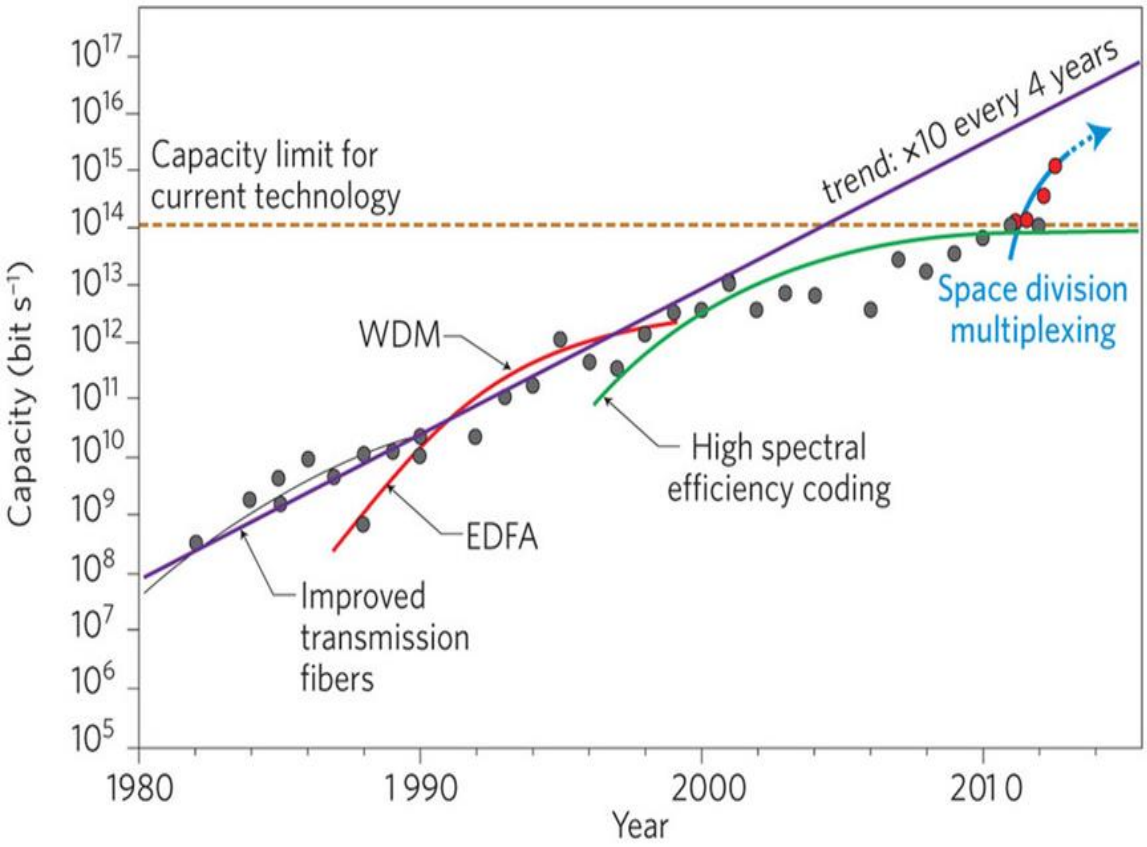

Figure 1.2 The increase of fiber capacity over the last three decades through key technology breakthrough

1.2. All-optical Switching and Encryption

The current optical communication system does not work entirely in optical domain. A larger amount of the switches and data processors are made of electrical circuits which limits the ultimate speed of the existing lightwave transmission system. One promising solution is all-optical packet switching networks in which the header recognizing, payload processing, buffering, and forwarding of optical packets are all carried out in the optical domain, bringing together the wide fiber bandwidth and high routers forwarding capacity [6]. In addition, the security of information is very important and all-optical encryption and decryption can be used to protect the information for future all-optical communication system.

The key building blocks of optical switching and encryption are the all-optical Boolean logic gates, include XOR, AND, OR, NAND, NOT and functional circuits built using these gates such as optical latches. It is important to build all-optical logic gates capable for high speed and high output quality. Previous attempts have been made to realize all-optical Boolean functions by using bulk or quantum well (QW) semiconductor optical amplifiers (SOA), whose operation data rate is usually limited to < 40Gb/s. The reason for this limitation is that bulk or QW SOAs have a relatively long carrier lifetime (~10 ps), making their gain and phase modulation response to ultrafast injection slow. This results in output distortion and errors.

In order to further enhance operation speed, we have two solutions. First, we can utilize quantum dot SOAs (QD-SOA) to realize all-optical logic gates. Because of their unique band structure and density of states, these kind of SOAs are more than 10 times faster in signal response time which suggests such devices are capable of handling data at speed up to 250Gb/s. The other method involves in the use of two-photon absorption (TPA) effect which is an ultrafast nonlinear process of SOA. With a high intensity pump light injected into SOA, a fast changing TPA induced phase shift becomes dominant in the total phase change experienced by a weak probe signal. As a result, the SOA will quickly respond to the injected short pulse in the active region which makes it suitable for high speed operation. In order to obtain better output quality, we can use binary phase shift keyed (BPSK) signal instead of on-off keyed (OOK) signal to realize all-optical logic gates. Because binary phase shift keyed (BPSK) signals carry information on the phase part while keeping the amplitude as a constant, the impairments from optical nonlinear effects and amplified spontaneous emission are greatly reduced.

1.3. Overview of This Thesis

In this doctoral dissertation, I present my research work on all-optical switching and encryption devices including logic gates, signal generators and short pulse generator. All these devices have been experimentally studied or numerically simulated. In chapter 2, I designed and simulated two kinds of optical latches: Set-Reset (S-R) latch and D-Flip-Flop. These all-optical latches are building blocks of all-optical packet switching networks. The latches

are built using two optical logic operations NAND and NOT which are realized by using Mach-Zhender interferometer (MZI) utilizing semiconductor optical amplifier with quantum dot active region (QD-SOA). Nonlinear dynamics including carrier heating and spectral hole-burning in the QD-SOA are taken into account together with the rate equations in order to realize the all-optical logic operations. Results show that this scheme can realize the functions of Set-Reset latch and D-Flip-Flop at high speeds (~ 250 Gb/s). The dependence of the output quality (Q factor) on QD-SOA parameters is also discussed in this chapter.

In chapter 3, another scheme to realize all-optical latches was presented. This scheme is based on ultrafast phase response in semiconductor optical amplifiers: the two-photon absorption process. Rate Equations for semiconductor optical amplifiers, for input data signals with high intensity, configured in the form of a Mach-Zehnder interferometer have been solved. The input intensities are high enough so that the two-photon induced phase change is larger than the regular gain induced phase change. The process is simulated similar to what is done in Chapter 2 and results show that optical latch can work at speed up to 250 Gb/s.

In chapter 4, I introduced the design of a scheme to realize high speed all-optical encryption and decryption using key-stream generators and XOR gate based on quantum-dot semiconductor optical amplifiers (QD-SOA). The key used for encryption and decryption is high speed all-optical pseudo random bit sequence (PRBS) which is generated by a linear feedback shift register (LFSR). Two other kinds of more secure key-stream generators, cascaded design and parallel design, have been designed and investigated in this chapter.

Results show that this scheme can realize the function of encryption and decryption at high speed (~ 250 Gb/s).

In chapter 5, I showed my design and simulation of a scheme to realize all-optical Boolean logic functions, XOR, AND and NAND operations using binary phase shift keyed (BPSK) signal instead of on-off keyed (OOK) signal with a pair of QD-SOA Mach-Zehnder interferometers based on QD-SOA. Results show that this scheme is suitable for high speed (@250Gb/s) all-optical Boolean logic operations and can improve the output quality comparing with the system using OOK signal.

In chapter 6, a fiber ring mode-locked laser system with charcoal nano-particles inside the cavity has been designed and experimentally demonstrated. The characterization of charcoal nano-particles and the setup of the experiment are also shown in this chapter. Both numerical simulation and experimental measurement are conducted. Results show that this fiber ring laser system can generate more stable and shorter pulse train at 20Gb/s through rational harmonic mode locking.

Chapter 2 All Optical Latches Using Quantum-Dot Semiconductor Optical Amplifier

2.1 Introduction

All-optical latches are important for a wide range of applications including communication systems, optical random access memory (RAM) and encryption. For communication system, it can be used for SONET scrambling and descrambling. The basic optical latches are the Set-Reset latch and the D-Flip-Flop. Both of these types of devices can be built using Boolean logic operations such as NAND and NOT. These operations are also important for all-optical signal processing such as bit pattern matching, pseudo random bit sequence (PRBS) generation and label swapping.

Researchers have demonstrated Boolean optical logic using different schemes, including using dual semiconductor optical amplifier (SOA) Mach-Zehnder interferometer (MZI) [1, 2], semiconductor laser amplifier (SLA) loop mirror [3], ultrafast nonlinear interferometer (UNI) [4], four-wave mixing (FWM) in SOA [5] and cross gain (XGM)/cross phase (XPM) modulation in nonlinear devices [6]. To the author's knowledge, optical logic gates have been demonstrated at 40 Gb/s [7] and demultiplexing at 160 Gb/s [8] using regular SOA based Mach-Zhender interferometer. In order to realize higher speed data processing, faster device

and schemes are needed. The emergence of semiconductor optical amplifiers with quantum dot active region, i.e. QD-SOA, in recent years, provides a faster device for signal processing. QD-SOAs have high saturated output power, low noise figure [9], fast carrier relaxation rate between QD energy states [10, 11] and a much smaller carrier heating impact on gain and phase recovery times [11] which makes them suitable for high speed Boolean logic operations.

In this chapter, I presented a model to simulate two basic all optical latches: Set-Reset Latch and D-Flip-Flop which are built using two optical logic operations NAND and NOT. Both the NAND and NOT operations are realized by using QD-SOA MZI in this model. The NAND gate is constructed using a series combination of AND and NOT gates. Results show that these all optical latches, Set-Reset and D-Flip-Flop, can be realized with a good output quality at high data rates (Q factor is about 7 @ ~ 250Gb/s). Other schemes to realize optical latches include vertical-cavity surface-emitting lasers (VCSELs) based optical switches and programmable optical logic [12] and optical logic operations in photonic crystal structure [13]. We believe, compared to the above schemes, the quantum dot SOA based MZI is capable of higher speed operation and relatively compact.

2.2 Schematic of All Optical Latches and QD-SOA Structure

The Set-Reset Latch can be considered as one of the most basic logic circuit possible. This simple latch is basically a one-bit memory bistable device that has two inputs, one of which

will "SET" the device (meaning the output = "1"), and another which will "RESET" the device (meaning the output = "0"). Then the SR description stands for "Set-Reset". The reset input resets the flip-flop back to its original state with an output Q that will be either at a logic level "1" or logic "0" depending upon this set/reset condition. The simplest way to make Set-Reset Latch is to connect together a pair of cross-coupled 2-input NAND gates. The schematic of Set-Reset Latch and the truth table for the Set-Reset function are showed in Figure 2.1.

The D-Flip-Flop is also widely used as the building block of a logic circuit. It is also known as a data or delay flip-flop. The D-Flip-Flop captures the value of the D-input at a definite portion of the gate cycle (such as the rising edge of the gate pulse). That captured value becomes the Q output. At other times, the output Q does not change. The D- Flip-flop can be viewed as a memory cell, a zero-order hold, or a delay line. We can use the NAND and NOT gates to make a D-Flip-Flop. The schematic of D-Flip-Flop and the truth table for D-Flip-Flop function are showed in Figure 2.2.

To meet the requirements for high speed switching and signal processing in the communication band, a quantum dot-based device needs to have high power gain over a spectral band covering 1.3–1.6 μm wavelength range. The device also needs compatible with a current-confining structure for a high current density. For these requirements, researchers have chosen InAs Stranski–Krastanow (SK) QDs in InGaAsP on an InP (100) substrate [14-15]. This material is also fully compatible with the well-established processing technique

on an InP substrate. The parameters I used throughout this dissertation were measured with a device having a tilted waveguide (8 degree off angle) and window structure to suppress lasing action. The waveguide length, stripe width, number of QD layers, and density of QDs are 6.15 mm, 2.2 μm, 22, and 9×10^{10} cm^{-2} , respectively [14]. The 22 stacks of QD layers were sandwiched between 160 nm thick InGaAsP separate confinement heterostructure layers. The structure of the waveguide is

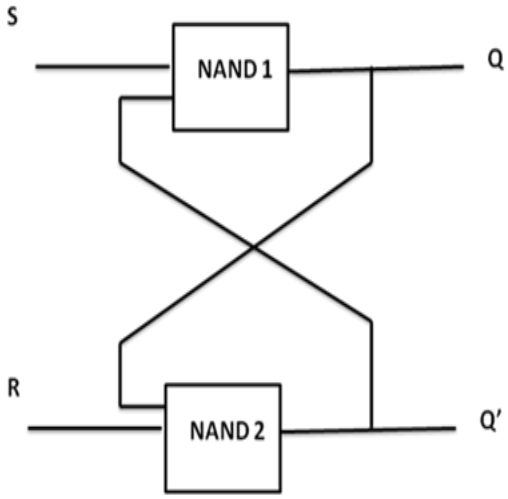

S	R	Action
0	0	Restricted Combination
0	1	Q=1, Q'=0
1	0	Q=0, Q'=1
1	1	No Change

Figure 2.1: The left figure is the schematic of the Set-Reset Latch. The right figure is the truth table for the Set-Reset function.

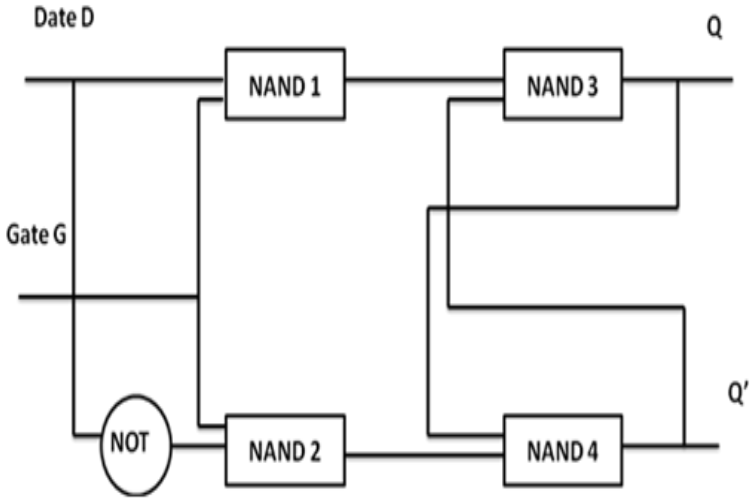

Gate	D	Q next
Rising edge (1)	0	0
Rising edge (1)	1	1
Non-Rising (0)	*	Q

Figure 2.2: The left figure is the schematic of the D-Flip-Flop. The right figure is the truth table for D-Flip-Flop function.

shown in figure 2.3 (a). The active layer of the device consists of alternately stacked InAs island layers and InGaAsP intermediate layers, as shown in figure 2.3(b). This type of dots configuration can significantly increase the modal gain of the SOA and has polarization-independent gain [15]. The device is anti-reflection coated at both facets.

2.3 Realization of all-optical logic gates using QD-SOA-MZI

The device we studied in this chapter is InAs/GaAs QD-SOA, with InAs Stranski-Krastanov (SK) quantum dots embedded in GaAs layer [16, 17]. This type of device can provide ~15dB gain at wavelength 1550nm with noise figure as low as 6-7dB. In this chapter, I used the two-level quantum dot (QD) model [18, 19] to simulate the carrier transitions [20-23] in the device. The QD model we use here is schematically illustrated in Figure 2.4. The GaAs layer is the "wetting layer" in Figure 2.4 which used to feed the ground state and excited state with

carriers through interstate recombination. External current is applied to the device and mostly accumulated in the wetting layer.

We use rate equations to describe gain and phase dynamics in QD device. The rate equations are as follows:

$$\frac{dN_w}{dt} = \frac{I}{eV} - \frac{N_w}{\tau_{wr}} - \frac{N_w}{\tau_{w-e}}(1-\frac{N_{es}}{N_{esm}}) + \frac{N_{es}}{\tau_{e-w}}(1-\frac{N_w}{N_{wm}}) \tag{3.1}$$

$$\frac{dN_{es}}{dt} = -\frac{N_{es}}{\tau_{esr}} + \frac{N_w}{\tau_{w-e}}(1-\frac{N_{es}}{N_{esm}}) - \frac{N_{es}}{\tau_{e-w}}(1-\frac{N_w}{N_{wm}}) + \frac{N_{gs}}{\tau_{g-e}}(1-\frac{N_{es}}{N_{esm}}) - \frac{N_{es}}{\tau_{e-g}}(1-\frac{N_{gs}}{N_{gsm}}) \tag{3.2}$$

$$\frac{dN_{gs}}{dt} = -\frac{N_{gs}}{\tau_{gsr}} - \frac{N_{gs}}{\tau_{g-e}}(1-\frac{N_{es}}{N_{esm}}) + \frac{N_{es}}{\tau_{e-g}}(1-\frac{N_{gs}}{N_{gsm}}) - \frac{\Gamma_d}{A_d}a(2\frac{N_{gs}}{N_{gsm}}-1)\frac{S(t)}{\hbar\omega} \tag{3.3}$$

where N_w, N_{es} and N_{gs} are the carrier density of the wetting layer, QD excited state and QD ground state, respectively. Γ_d is the ratio of the intensity of light coupled into the active layer to the total input light, referred to as the confinement factor. A_d is the effective cross-section area of the quantum dot effective layer, I is the injected current, V is the effective volume of the active layer, a is differential gain, S(t) is photon density in the active region. τ_{wr}, τ_{esr} and τ_{gsr} are the carrier lifetimes of the energy levels, respectively; $\tau_{a\text{-}b}$ is the carrier relaxation time from QD energy level a to level b (a, b being "w", "e" or "g" for wetting layer, excited state and ground state, respectively). We can simplify the equations (3.1-3.3) by normalizing all the terms using the maximum density of carriers in each of the states, N_w, N_{es} and N_{gs}.

$$w = \frac{N_w}{N_{wm}} \tag{3.4}$$

$$h = \frac{N_{es}}{N_{esm}} \tag{3.5}$$

$$f = \frac{N_{gs}}{N_{gsm}} \tag{3.6}$$

Thus the rate equations are simplified to:

$$\frac{dw}{dt} = \frac{I}{eVN_{wm}} - \frac{w}{\tau_{wr}} - \frac{w}{\tau_{w-e}}(1-h) + \frac{N_{esm}}{N_{wm}}\frac{h}{\tau_{e-w}}(1-w) \tag{3.7}$$

$$\frac{dh}{dt} = -\frac{h}{\tau_{esr}} + \frac{N_{wm}}{N_{esm}}\frac{w}{\tau_{w-e}}(1-h) - \frac{h}{\tau_{e-w}}(1-w) + \frac{N_{gsm}}{N_{esm}}\frac{f}{\tau_{g-e}}(1-h) - \frac{h}{\tau_{e-g}}(1-f) \tag{3.8}$$

$$\frac{df}{dt} = -\frac{f}{\tau_{gsr}} - \frac{f}{\tau_{g-e}}(1-h) + \frac{N_{esm}}{N_{gsm}}\frac{h}{\tau_{e-g}}(1-f) - \frac{\Gamma_d}{A_d}a(2f-1)\frac{1}{N_{gsm}}\frac{S(t)}{\hbar\omega} \tag{3.9}$$

where w, h and f are the occupation probabilities of the wetting layer, the QD excited state and ground state, respectively.

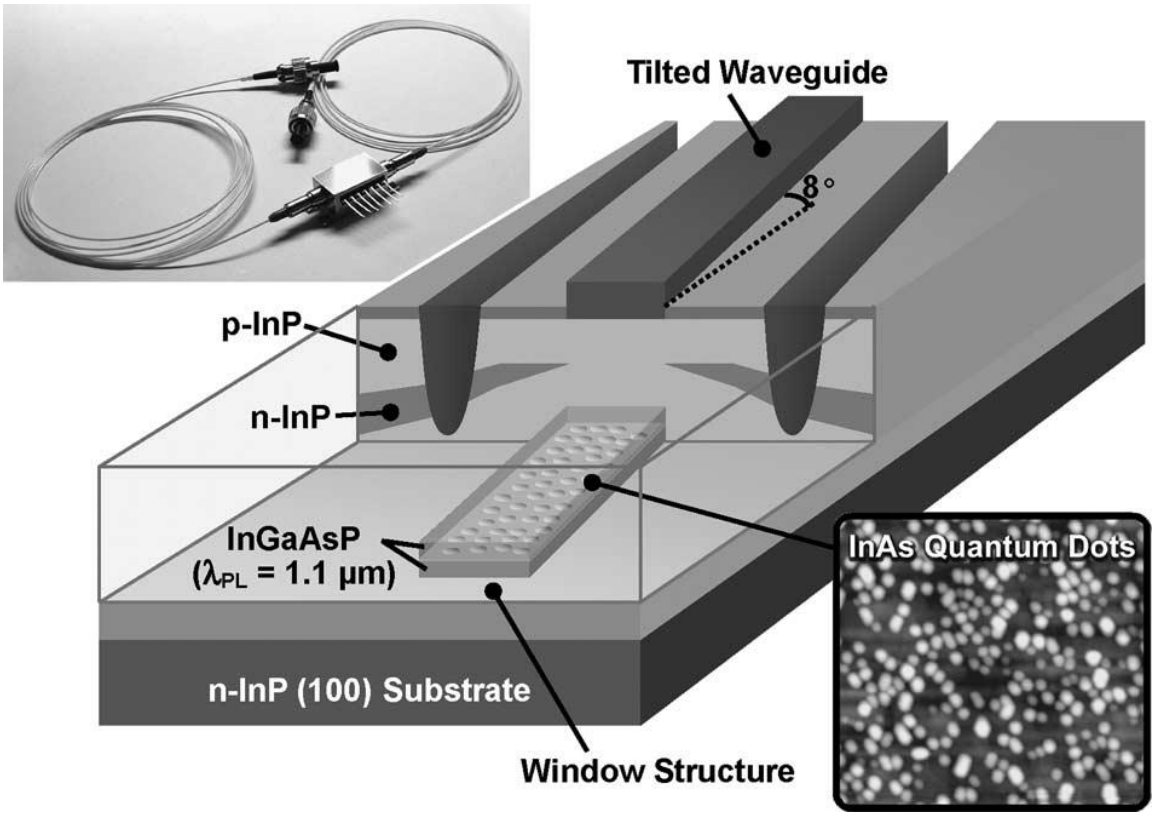

Figure 2.3 (a) Structure of an InAs/InGaAsP/InP semiconductor optical amplifier fabricated on an InP substrate [17]. The inset is a picture of fiber-pigtailed butterfly module with temperature controller.

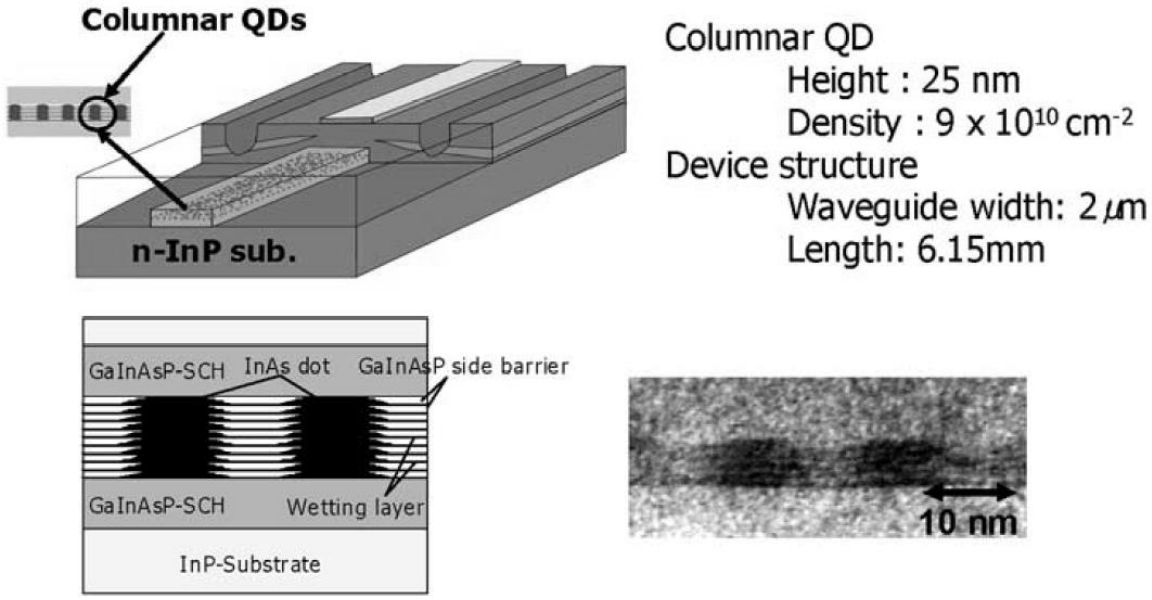

Figure 2.3 (b) Structure of columnar quantum dot (CQD) with a number of layers [19], SCH: separate confinement heterostructure.

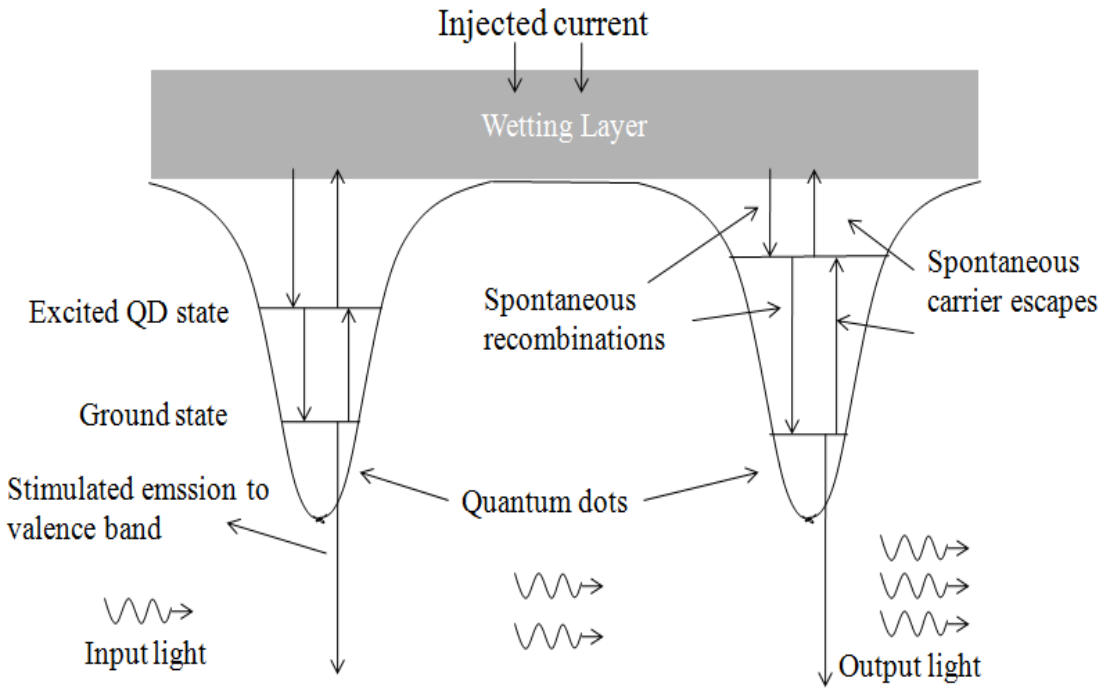

Figure 2.4: Schematic of QD states and carrier transitions of InAs/GaAs QD-SOA.

The gain dynamics in the QD-SOA include the contribution from the carrier density pulsation dynamics and nonlinear processes including carrier heating (CH) and spectral hole-burning (SHB) effect. Generally, the linear part of gain coefficient is based on the stimulated emission from the QD ground state to the valence band:

$$g_l = \Gamma_d a(N_g - N_t)$$

(3.10)

where N_t is the transparent carrier density of the QD ground state. The suppression of the gain coefficient brought by nonlinear CH and SHB effects can be expressed as:

$$g(t) = g_l + \Delta g_{CH} + \Delta g_{SHB} \tag{3.11}$$

To a first approximation, Δg_{CH} and Δg_{SHB} are proportional to instantaneous light intensity S(t).

$$\Delta g_{CH} = -\varepsilon_{CH} g S(t) \tag{3.12}$$

$$\Delta g_{SHB} = -\varepsilon_{SHB} g S(t) \tag{3.13}$$

where ε_{CH} and ε_{SHB} are the gain suppression factors of carrier heating and spectral hole burning effect, respectively. From (3.11 – 3.13) we can get [11, 22]:

$$g(t) = \frac{a(N - N_t)}{1 + (\varepsilon_{CH} + \varepsilon_{SHB}) S(t)} \tag{3.14}$$

The injected light and changed temperature result from carrier heating also changes the refractive index of the active region, and thus a phase change to any probe wave injected.

$$\phi(t) = -\frac{1}{2}(\alpha G_l(t) + \alpha_{CH} \Delta G_{CH}(t)) \tag{3.15}$$

where $G_l(t)=e^{g(t)l}$ is the gain factor of the device with l being the effective length of the active layer, α and α_{CH} are the linewidth enhancement factor of the device and that corresponding to carrier heating process, respectively. The linewidth enhancement factor due to spectral hole burning (SHB) is ~ 0.

We can use the QD-SOA MZI system to realize all-optical AND, NOT logic operations. As is shown in Figure 2.5, two identical QD-SOAs form the two arms of the Mach-Zhender interferometer (MZI), three optical data streams centered at two different wavelengths are coupled into these two arms, where the control beam at λ_2 is evenly split into two branches at port 3 and guided into the two QD-SOAs respectively. The two beams then interact with data stream A, B and will experience a modulated gain and phase via XGM and XPM processes. The two branches recombine at port 4, the phase shifters give the two arms an initial phase difference, after a band-pass filter which screen out wavelength components λ_1, the interference result which is at λ_2 is expressed as [2]:

$$P_{out}(t)=\frac{P_{cb}(t)}{4}\left[G_1(t)+G_2(t)+2\sqrt{G_1(t)G_2(t)}\cos\left(\phi_1(t)-\phi_2(t)+\phi_0\right)\right] \tag{3.16}$$

where $P_{cb}(t)$ is the time-dependent power of control beam. ϕ_1 and ϕ_2 are phases experienced by the control beam in each arm. We set the initial phase difference between the two arms ϕ_0 as π so the above equation becomes:

$$P_{out}(t)=\frac{P_{cb}(t)}{4}\left[G_1(t)+G_2(t)-2\sqrt{G_1(t)G_2(t)}\cos\left(\phi_1(t)-\phi_2(t)\right)\right] \tag{3.17}$$

In order to realize all –optical XOR logic gate, we can set control beam as clock wave at the same repetition rate as data A and B. When A = B = 0 or A = B = 1, the control beams in each arm will see the same cross gain or phase modulation as they go through the QD-SOA. And the output branches of the control beam will have a destructive interference pattern at output because of the initial π phase difference, and the output will be 0 at wavelength λ_2. When $A \neq B$, the branches of control beam will undergo different gain and phase modulation so we

can have a constructive interference at output port if we can change the power of modulating data streams A and B to make ϕ_1- $\phi_2=\pi$, in this case the output will be 1 for wavelength λ_2, which is the same as logic A XOR B. Similarly, if we use a clock signal as date B which is put into port 2, put data A into port 1, and use optical CW as control beam, we can get out of port 4 data pattern of A XOR "1", which is the same in terms of truth value as "INVERT A". We can also use a similar MZI scheme [24] to realize all-optical logic AND operation based on QD-SOA. By putting data A to port 1 and using data B as control beam, we can get gain modulated pattern of data B out of port 4 resembling logic A AND B. To make results better in quality, a low power CW light is used into port 2 to cancel out the background noise of date stream A.

Because the NAND operation is just a series combination of AND and NOT operations, then we can realize the logic NAND operation by using this QD-SOA-MZI scheme. As shown in Figure 2.6, the first QD-SOA-MZI serves in the system as an optical logic AND gate. After screening out all other wavelength components using a band-pass filter (BPF), the A AND B output data stream (λ_2) is amplified to desired power by an amplifier and guided into port 5 as data to one arm of the second MZI for INVERT operation. In this way, the result centered at λ_1 coming out of port 8 will be the INVERT of signal injected into port 5, which is the same as logic A NAND B. From section 2.2, we know NAND logic gate is the building block of all-optical latches such as Set-Reset and D-Flip-flop. Thus, we can use the above QD-SOA-MZI system to realize all-optical latches.

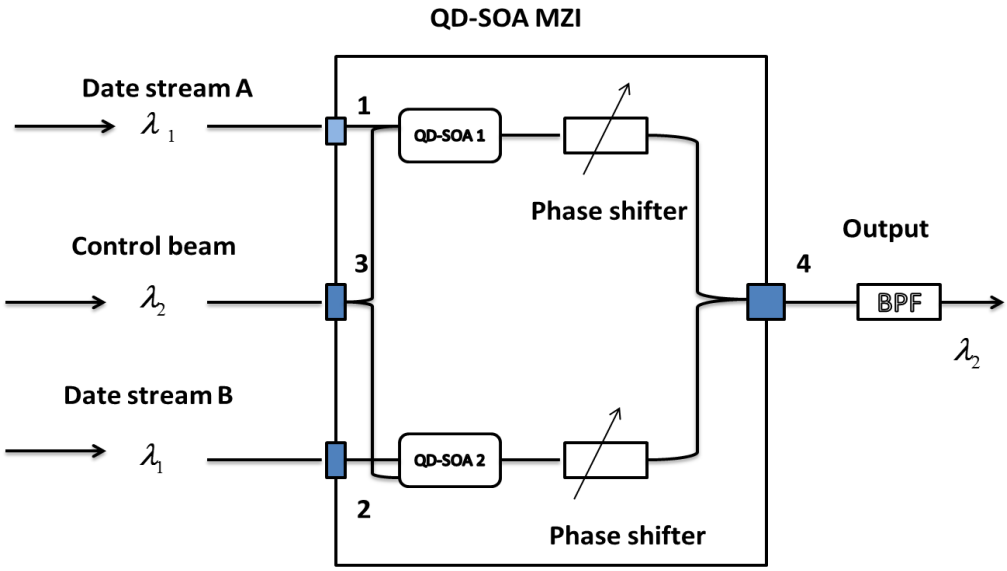

Figure 2.5: Schematic of QD-SOA Mach-Zehnder Interferometer. BPF: bandpass filter

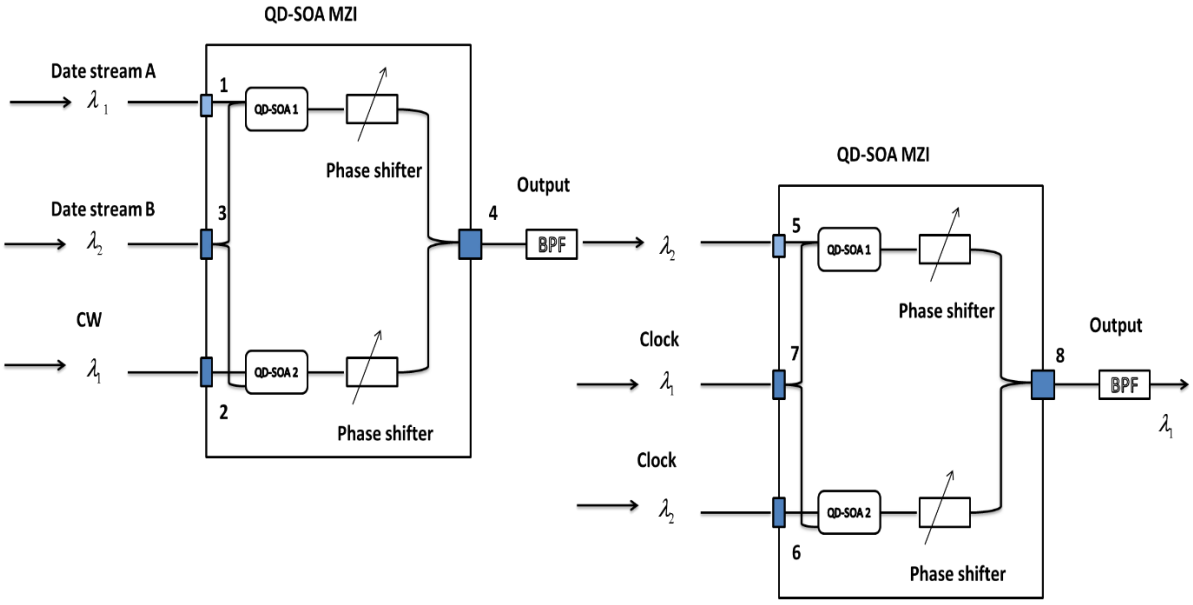

Figure 2.6: Schematic of all-optical NAND logic gate based on QD-SOA-MZI.

2.4 Simulation result and output quality evaluation

Parameters chosen for simulation in this chaper are experimental results on QD-SOAs for central wavelength: 1.55μm: $\tau_{wr}=\tau_{esr}$=200ps, τ_{gsr}=50ps, $\tau_{w\text{-}e}$=3ps, $\tau_{e\text{-}w}$=300ps [25], $\tau_{g\text{-}e}$=10ps, Γ_d=10%, linewidth enhancement factors α=4, α_{CH}=0.2 [26,27], QD energy levels' densities of states, $n_w=5.4\times10^{17}cm^{-3}$, $n_w:n_e:n_g\approx15:2:1$ [19], QD areal density is $7.5\times10^{10}cm^{-2}$, saturated output power is 18dBm at 1.55μm wavelength [8], device differential gain $a=8.6\times10^{-15}cm^2$ [17], effective length l=1.0mm, transparency pump current density is ~0.2kA/cm^2 [11], gain suppression factors are $\varepsilon_{CH}=0.5\times10^{-23}m^3$, $\varepsilon_{SHB}=7.5\times10^{-23}m^3$ [26], which correspond to threshold input pulse energy for both nonlinear effects ~0.47pJ. Value of time constant $\tau_{e\text{-}g}$ has been measured in many experiments, the smallest reported value is ~0.1ps [11] and the largest measured value goes up to several picoseconds [19]. We have not taken into account the inhomogeneous broadening associated with different dot sizes. But it is indirectly taken into account in the form spectral hole burning. In a QD the inhomogeneously broadened spectrum range could be small because it requires carrier transport among QDs: a QD has discrete transition wavelengths and carrier relaxation to another wavelength involves transition to another QD [22].

Spectral hole burning in the inhomogeneously broadened gain of QDs has been experimentally studied and is believed to be due to carrier transfer to another QD [22]. The

carrier relaxation mechanisms such as spectral hole burning (SHB) and carrier heating in QD amplifiers has been extensively studied both in the absorption (low injection current) and gain (high injection current) regime using pump–probe experiments [23]. These authors find that in QD amplifiers, the fast gain recovery is dominated by the ultrafast SHB process. They point out that the gain recovery in QD amplifiers involves several processes such as electron and hole transfer to another QD, two-photon absorption, Auger effect and carrier relaxation from excited to ground state; and one of the difficulties in interpreting the pump-probe data is that all of these processes occur simultaneously. When an optical pump pulse is injected, a depletion of gain occurs due to stimulated transitions induced by the input pulse. The gain recovery process involves carrier transfer from another QD, the carrier transfer from a higher QD level and carrier transfer from wetting layer. At high pump energy, additional gain change due to two-photon absorption (TPA) is present which also recovers by some of the above processes. It has been suggested that the carrier relaxation corresponding to the fast SHB related gain recovery occurs probably via Auger scattering from the quantum dot excited states [23]. The spectral hole burning and carrier heating in our model represents these fast carrier transitions. The transition from the excited state to the ground state is a fast mechanism for repopulation of the ground state (and hence nearly complete gain recovery) of a QD following an optical pulse. Thus the wetting layer and the excited state represents a reservoir of carriers available for fast gain recovery. This is the main reason for fast gain and phase recovery and hence higher speed operation using quantum dot based semiconductor optical amplifiers relative to thick active region or quantum well amplifiers.

Simulated results of logic gate NAND, Set-Reset latch and D-Flip-Flop are shown in Figure 2.7, 2.8 and 2.9, respectively. The output eye-diagram is also plotted to show the output quality. Quality of the output can also be quantitatively evaluated by the quality factor, which is defined as $Q=(S_1-S_0)/(\sigma_1+\sigma_0)$ [28]. Here S_1 and S_0 are the average peak powers of output "1"s and "0"s, of the output respectively; σ_1 and σ_0 are their standard deviations. The noise of "1" and "0" in the output determine the standard deviation used in the Q-factor calculation. The lower level of the output is essentially the noise of "0" level. The quality factor is related to the gate's bit-error rate (BER) in terms of $BER \approx \frac{\exp(-Q^2/2)}{Q\sqrt{2\pi}}$ [28]. From the simulated results in Figure 2.7, 2.8 and 2.9, we show that all-optical Set-Reset latch and D-Flip-Flop operation @ ~ 250 Gb/s is feasible.

The primary noise in this calculation is due to pattern effects resulting from long recovery time (longer than bit length) of gain [11] and gain induced phase change i.e. the phase change produced by a given bit depends on the prior sequence of bits. We have also included noise due to amplified spontaneous emission (ASE). The ASE power is related to N_{SP} (spontaneous emission factor) by the relation [28]:

$$P_{ASE} = N_{SP}(G-1)h\upsilon B_0$$

(3.18)

where G is the maximum gain, h is Plank's constant, υ is the frequency ($\upsilon = c/\lambda$) and B_0 is the band width. The ASE noise is added numerically using the above equation to the pattern effect noise to obtain the Q-factor. When adding the ASE noise to the simulation program, we choose G=1000, N_{SP}=2, λ= 1550 nm, B_0=3 nm.

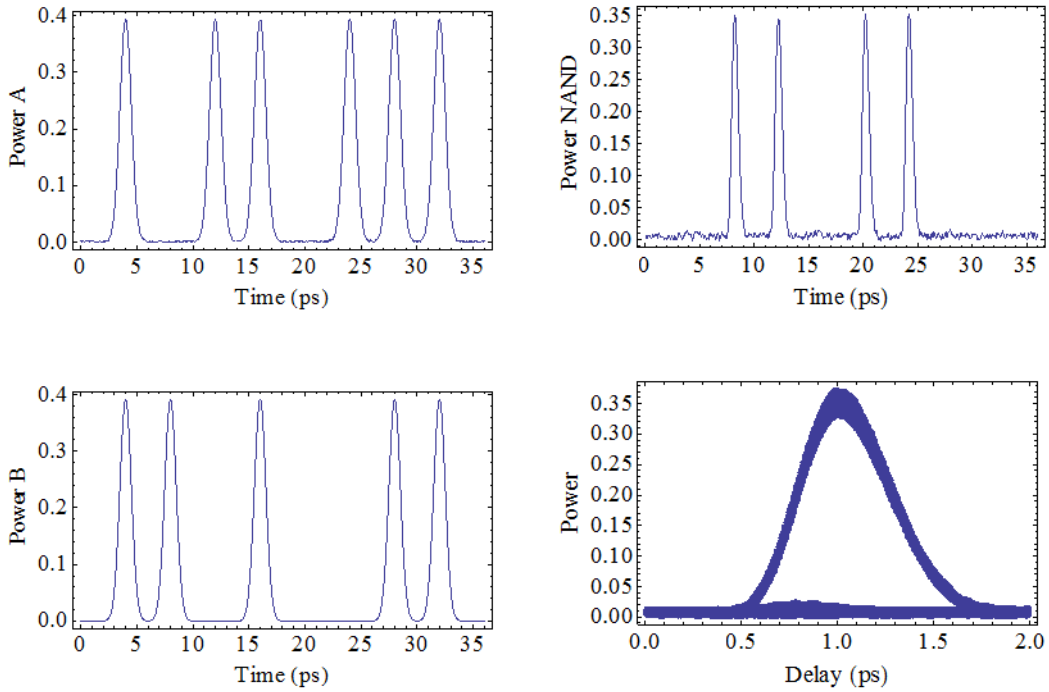

Figure 2.7: Date A and Date B are shown in the left. Simulated results of output (NAND) and eye pattern of the output are shown in the right. The above set of figures is for 250Gb/s data rate.

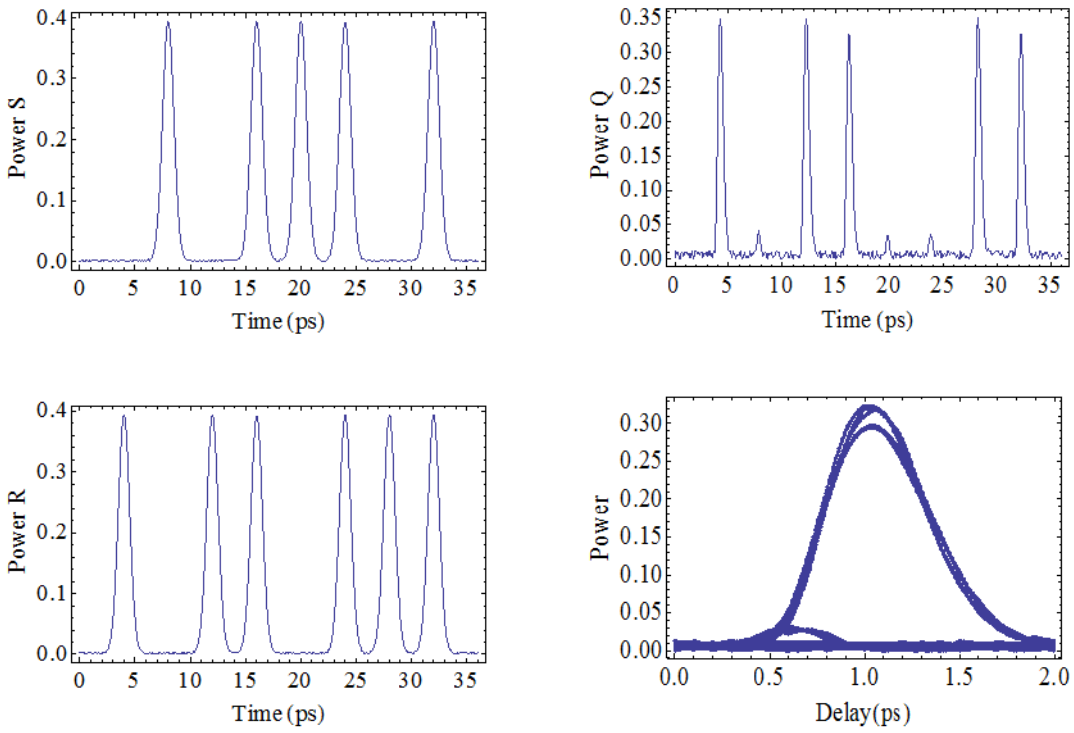

Figure 2.8: Set and Reset are shown in the left. Simulated results of output (Q) and eye pattern of the output are shown in the right. The above set of figures is for 250Gb/s data rate.

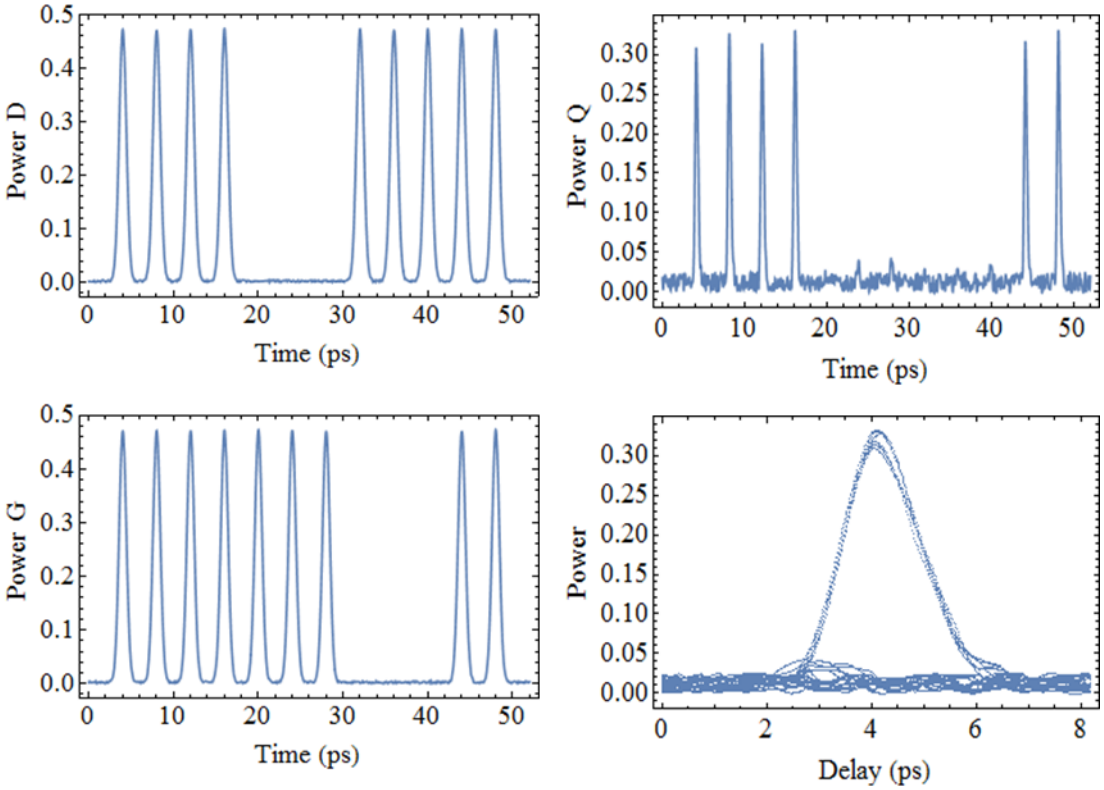

Figure 2.9: Date and Gate are shown in the left. Simulated results of output (Q) and eye pattern of the output are shown in the right. The above set of figures is for 250Gb/s data rate.

The above formulation takes into account the ASE noise in a time averaged form. The ASE noise adds a noise term to the average value of "0" and "1" output bits. Thus a larger ASE noise (for example due to larger spontaneous emission factor) would increase the average intensity of the "0" level and hence reduce the signal to noise ratio (Q factor as defined earlier). The pattern effect noise of "1" and "0" in the output determine the standard deviation used in the Q-factor calculation.

Figure 2.10 shows us the dependence of Q factor on pulse energy and speed of operation. From the result we find that the Q factor increases as pulse energy increases from 0.1pJ to ~ 0.5pJ and then decreases as pulse energy increases when pulse energy is larger than ~ 0.5pJ. The Q factor also decreases as bit-rate increases. This can be explained as: when pulse energy is less than ~ 0.5pJ, the ASE noise plays a significant role and the Q-factor increases with increasing power. For higher single pulse energies, the carrier density in the active region of the device is depleted more and it takes a longer time to recover to the initial level, therefore leading to bigger pattern effect (i.e. pattern effect plays a larger role) and Q factor decreases. The ideal N_{SP} value is N_{SP}=2. Since the spontaneous emission factor (N_{SP}) can vary (in the range of 2 to 8), the Q factor has also been calculated using N_{SP}=6. The result is shown in Figure 2.11. As expected the Q values of Figure 2.11 are less than that for Figure 8 due to higher noise.

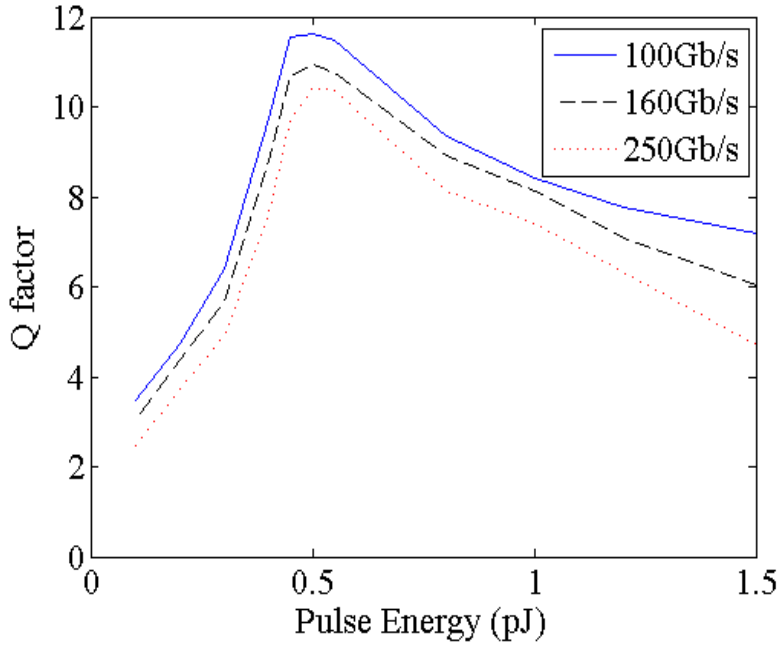

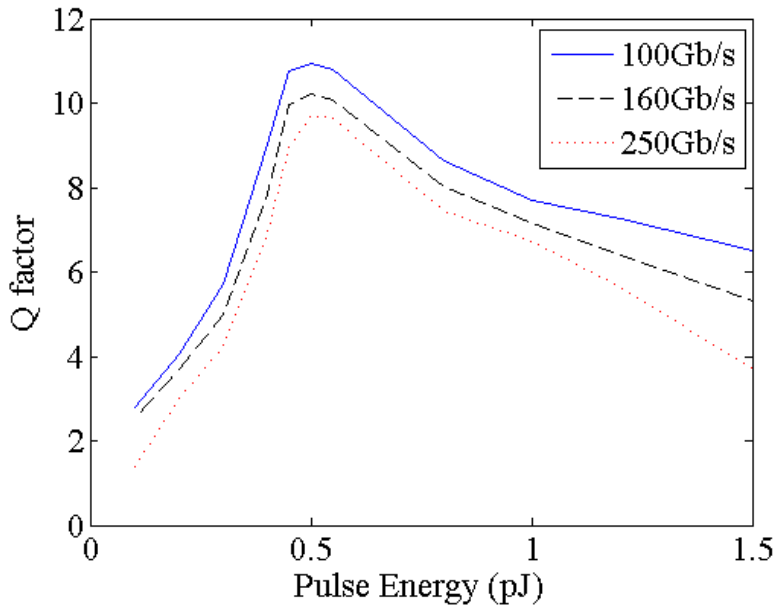

Figure 2.10: The dependence of calculated quality factor Q on pulse energy for different bit-rates. Pulse width is 1/3 of the pulse period for the three bit-rates. (Top: Set-Reset Latch, Bottom: D-Flip-Flop). The three curves are for data rates of 100, 160 and 250 Gb/s respectively. N_{SP}=2.

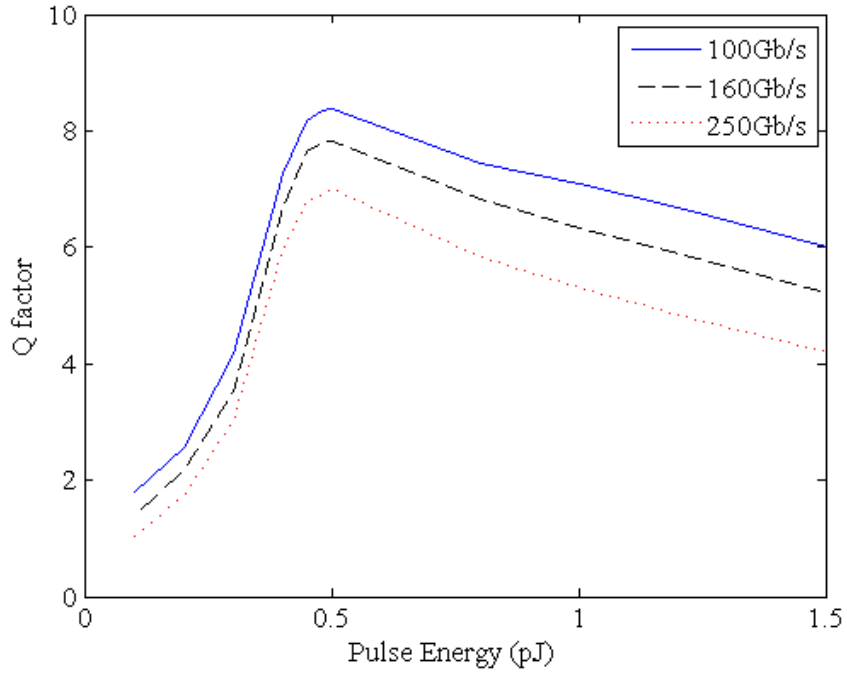

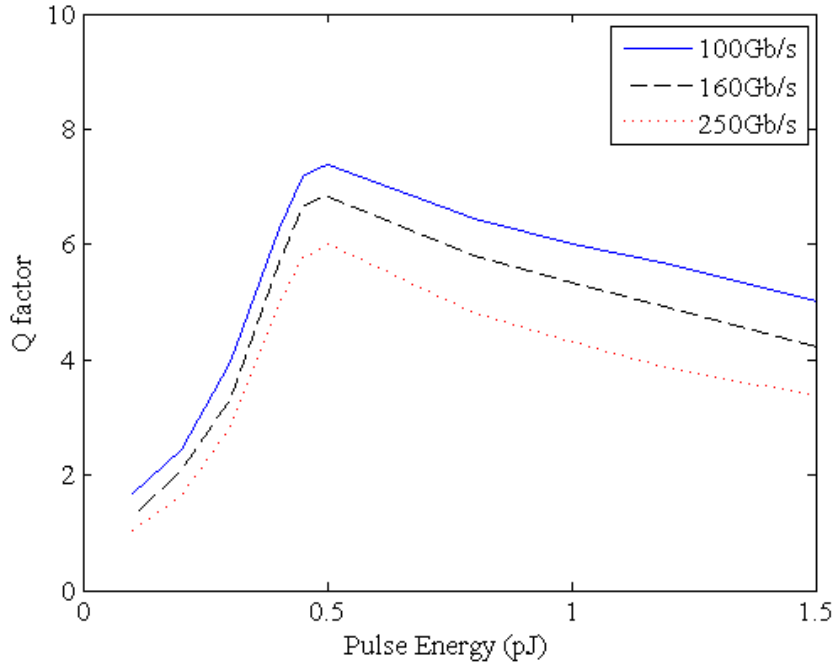

Figure 2.11: The dependence of calculated quality factor Q on pulse energy for different bit-rates. Pulse width is 1/3 of the pulse period for the three bit-rates. (Top: Set-Reset Latch, Bottom: D-Flip-Flop). The three curves are for data rates of 100, 160 and 250 Gb/s

respectively. N_{SP}=6

We also calculated the dependence of Q-factor on carrier transition lifetime and injected current density. Figure 2.12 shows the dependence of Q-factor on transition lifetime and speed of operation. From the result we find that the Q factor decreases as transition lifetime and bit-rate increases. This can be explained as follows: the transition lifetime determines the speed of gain and phase recovery in the active region so Q factor is higher for shorter transition time. Figure 2.13 shows the dependence of Q factor on injected current density and input pulse width. From the results we find that at low injected current level ($J<1.5$ kA/cm^2), the Q factor is lower and increases as current density increases. This can be explained as: with increased current density, more carriers are injected to the wetting layer, thus each QD energy level recovers faster to initial carrier density level after depletion following pulse injection and amplification. This reduces the pattern effect considerably. For higher current density ($J>2$ kA/cm^2), the increase in J will have a smaller impact on the gain recovery process because of carrier saturation. Also, narrower the input pulse (less energy and hence less carrier depletion) results in better performance (higher Q).

The main parameters in the model which determine the performance at high speed are: (i) transition time from the excited state to the ground state, (ii) the injected current density in the QD-SOA and, (iii) the amplified spontaneous emission noise. The dependence of Q-factor on these major parameters has been calculated and analyzed.

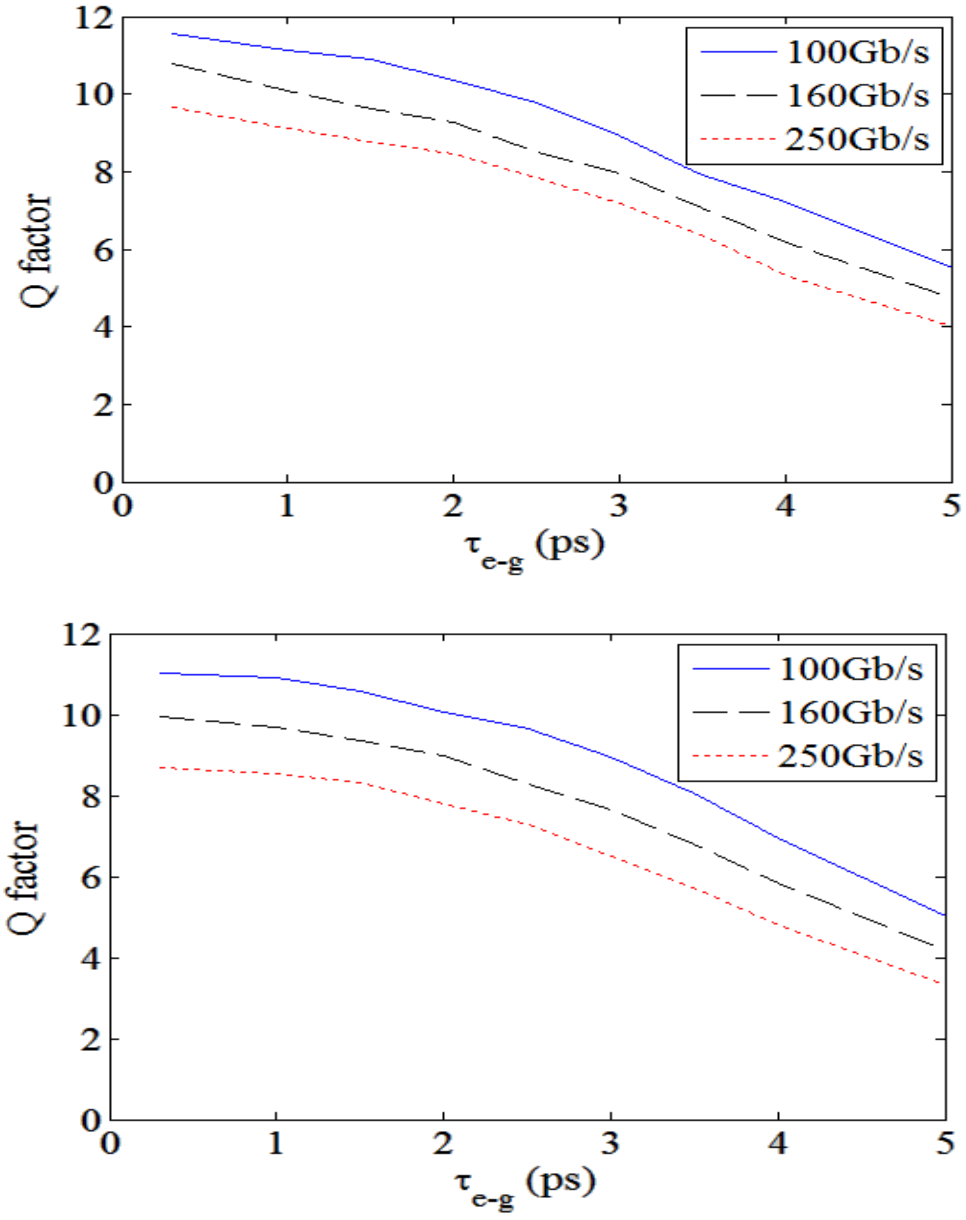

Figure 2.12: The dependence of calculated quality Q on transition lifetime for different bit-rates. Pulse width is 1/3 of the pulse period for the three bit-rates. (Top: Set-Reset Latch, Bottom: D-Flip-Flop). The three curves are for data rates of 100, 160 and 250 Gb/s respectively.

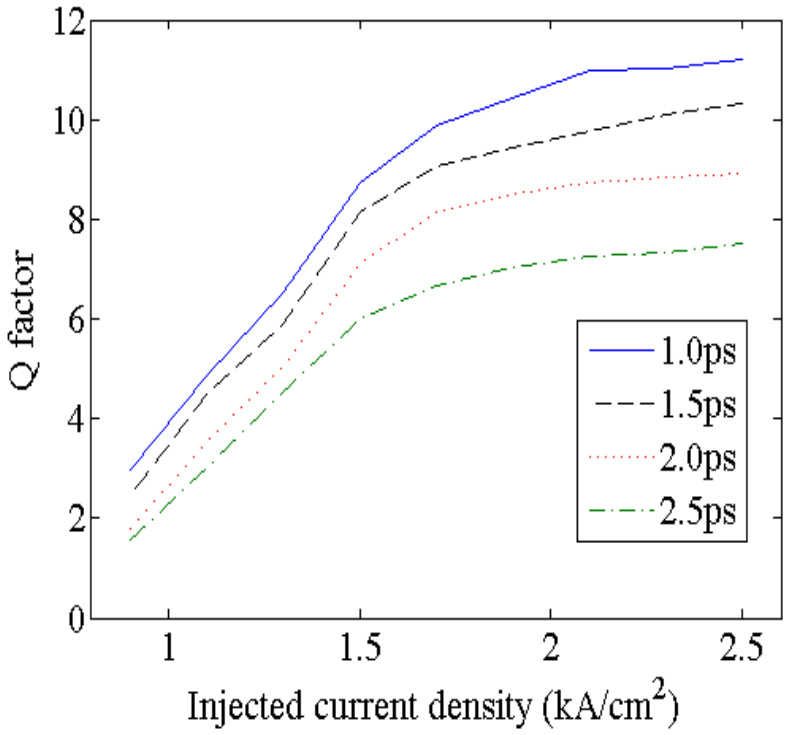

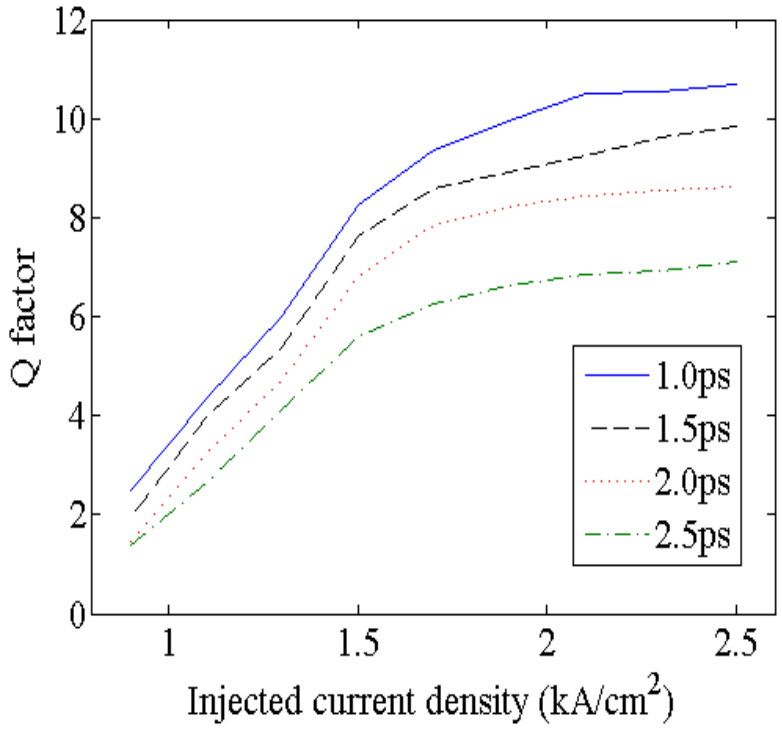

Figure 2.13: The dependence of calculated quality factor Q on injected current density for

different pulse width. (Top: Set-Reset Latch, Bottom: D-Flip-Flop). The four curves are for pulse width of 1.0ps, 1.5ps, 2.0ps and 2.5ps respectively.

2.5 Conclusion

In this chapter I designed and modeled high speed all optical Set-Reset Latch and D-Flip-Flop which are built using two optical logic operations NAND and NOT. Both NAND and NOT operations are realized using QD-SOA (semiconductor optical amplifier with quantum dot active region) based Mach-Zehnder Interferometer in this model. Results show that this model can perform the basic function of Set-Reset Latch and D-Flip-Flop at high bit-rates of ~ 250 Gb/s. The impact of the high speed output quality (Q factor) on a number of parameters, including speed of operation, transition lifetime $\tau_{e\text{-}g}$ and pulse energy has been studied and discussed. Results show that for best output quality for high data rate operation (~ 250Gb/s), this system requires single pulse energy of <1.0pJ, shorter transition lifetime $\tau_{e\text{-}g}$ (<3ps), and narrow input pulse width (FWHM~1.0ps).

Chapter 3 All Optical Latches based on Two-photon Absorption in Semiconductor Optical Amplifiers

3.1 Introduction

Optical latches are important for a wide range of applications including communication systems, optical logic systems, optical random access memory (RAM) and encryption. For communication system it can be used for SONET scrambling and descrambling. The basic optical latches are the Set-Reset latch and the D-Flip-Flop. Both of these types of devices can be built using Boolean logic operations such as NAND and NOT. These operations are also important for all-optical signal processing such as bit pattern matching, pseudo random bit sequence (PRBS) generation and label swapping.

In recent years, researchers have demonstrated Boolean optical logic using different schemes, including using dual semiconductor optical amplifier (SOA) Mach-Zehnder interferometer (MZI) [1, 2], semiconductor laser amplifier (SLA) loop mirror [3], ultrafast nonlinear interferometer (UNI) [4], four-wave mixing (FWM) in SOA [5] and cross gain (XGM)/cross phase (XPM) modulation in nonlinear devices [6]. Among the above schemes, the SOA based MZI has the advantage of being relatively stable, simple and compact. To my knowledge,

however, all these schemes have a limitation of signal bit rate of up to 40 or 80 Gb/s. A scheme for higher date rate logic using quantum dot (QD) based optical amplifiers [7-9] has been analyzed. It is also known that two-photon absorption of a pump beam can result in fast phase change of a probe signal [10-14]. Pump–probe experiment have shown that phase changes take place in a duration ~1ps or less when the pump and probe signals are injected into a semiconductor optical amplifier [10-13]. The magnitude of TPA induced phase shift can be expressed as [11, 12]:

$$\delta\phi = -(1/2)\beta\alpha_2 S(t) L \tag{3.1}$$

where β is TPA coefficient, α_2 is linewidth enhancement factor due to TPA process, S(t) is the light intensity, and L is the effective length of SOA active region. The negative sign represents the observation that the two-photon absorption (TPA) induced phase change is in an opposite direction from that for gain change induced phase change [10, 12]. The typical α_2 value of bulk SOA is around -4 [12], TPA coefficient β is between 20 and 35cm^{-1}/GW [10, 11]. If a 250 Gb/s pulse train with an average input power 20 mW and pulse FWHM (full width at half maximum) of 0.5 ps is injected into SOA with an mode cross section 0.5μm^2, the peak light intensity would be ~32MW cm^{-2}. For SOA with an effective length of 7 mm, TPA coefficient β=30cm/GW, and α_2= -4; the peak phase change experienced by the probe is ~ 0.4π. This phase change is large enough for temporal interference of probe pulses traveling through the two arms of the MZI.

The optical powers needed for XGM (cross gain modulation) and XPM (cross phase modulation) are considerably smaller (~ 1mW). Thus both XGM and XPM are present when

the SOA is used in a Mach-Zhender interferometer (MZI) configuration to form the logic gates. However, these processes are proportional to the power and are slow (time scale ~ 20 ps) compared to the two-photon absorption (TPA) related phase change which is fast (time scale ~ 0.5 ps) and is proportional to the square of the power. Thus high powers are necessary for TPA based MZI. The input average power of the SOA used in this chapter to obtain significant two-photon absorption is 20 mW which corresponds to a peak power of 160 mW at 250 Gb/s when the input pulse width (used in the simulation here) is 0.5 ps. Although this peak power seems high at first glance, Ref. [11] reports measurements on SOAs with high optical peak power. An optical pulse with an energy of 1 pJ in a 200 fs wide pulse has a peak power of 5 W. Measurements at high peak power (a few W) are also reported in Ref. [13]. Thus a few hundred mW of peak power in an ultra-short pulse is acceptable for SOAs. The effect of other nonlinearities such as four wave mixing (FWM) is eliminated (or minimized) in the output with the use of a bandpass filter.

In this chapter, I presented a model to simulate two basic all optical latches: Set-Reset Latch and D-Flip-Flop which are built using two optical logic operations NAND and NOT. Both the NAND and NOT operations are realized by using the ultrafast phase response during two-photon absorption (TPA) process in semiconductor optical amplifiers (SOA) in this model. The NAND gate is constructed using a series combination of AND and NOT gates. NAND gate is important because other Boolean logic elements and circuits can be realized using NAND gates as basic building blocks. Results show that all these optical latches, Set-Reset and D-Flip-Flop, can be realized with a good output quality at high data rates (Q

factor is about 7 @ ~ 250Gb/s).

3.2 Principle of Operation of All-Optical NAND Logic Gate

NAND gates are built using semiconductor optical amplifier based Mach-Zhender interferometer (SOA-MZI). The SOA-MZI consists of two semiconductor optical amplifiers (SOAs) configured in the form of a Mach-Zhender interferometer with additional phase shifters in each arm (the elements in the square block in Figure 3.1). The first SOA-MZI serves in the system as an optical AND gate. Date stream A (centered at λ_1) is coupled into port 1 and a low power CW (wavelength λ_1) light is coupled into port 2, while date stream B (centered at λ_2) is split at port 3 and sent into both SOAs. The bandpass filter (BPF) is set to pass wavelength λ_2. The phase shifters in the interferometer are adjusted so that in the absence of any inputs to ports 1 and 2, there is a phase difference of π between the two arms so that if B=1, A= 0, the output is 0. If B=0, the output is always 0. If A=1 (in port 1), a phase change of ϕ is produced by data A on data B through cross phase modulation (XPM) and two-photon absorption (TPA) process for the upper arm in Figure 3.1, then the output approximately becomes $I_B(1+ \text{Cos}\ (\pi+\phi))$ where I_B is the intensity of the data stream B. As expected, this intensity is maximum when $\phi= \pi$, a departure from $\phi= \pi$ simply reduces the signal to noise ratio. Thus the output light centered at λ_2 coming out of port 4 is 1 only if A=1 and B=1, which is logic operation A AND B. To make results better in quality, a low power CW light goes into port 2 to reduce the noise of data stream A [15]. After screening out all other wavelength components using a band-pass filter (BPF), the A AND B output data stream (λ_2) is amplified to desired power by an amplifier and guided into port 5 as data to one arm of the

second MZI for INVERT operation (described below).

The output of first stage (A AND B) is coupled into port 5 (which goes through one SOA), and a clock pulse train (all 1's) with the same pulse shape and pulse energy (centered at λ_2) is injected to port 6 (which goes through a second SOA). A CW light (wavelength λ_1) is injected into port 7 (center port). This light (wavelength λ_1) is split and goes through both SOAs. The bandpass filter (BPF) is set to pass wavelength λ_1. The phase shifters in the interferometer are adjusted so that in the absence of any inputs to ports 5 and 6, there is a phase difference of π between the two arms so that if input 5 is 1, and since input 6 is always 1, the output is 0. If input 5 is 0, and since input 6 is always 1, the output is 1. Thus the result at port 8 will be INVERT of port 5 input, i.e, INVERT of A AND B, which is the same as logic A NAND B.

Logic gates utilizing cross-phase modulation (XPM) process in SOAs have previously been studied [16, Chapter 9, 2-6]. A major difference between the current scheme and pervious work is that the input data pulses are of sufficiently short duration, and has higher peak power, as a result the pulse are of higher intensity to produce two-photon absorption and the resulting fast phase change. The average power of the data pulses are about a factor of 20 higher than that used in previous work and the pulse duration is shorter (<1ps). The MZI output can be expressed as:

$$P_{out}(t) = \frac{P_{in}(t)}{4}\left[G_1(t) + G_2(t) - 2\sqrt{G_1(t)G_2(t)}\cos\left(\phi_1(t) - \phi_2(t)\right)\right] \tag{3.2}$$

where P_{in} is the input optical power of the weak probe signal, G_1 and G_2 are the gain in two arms of SOA-MZI, ϕ_1-ϕ_2 is the phase difference of the probe signal in two arms.

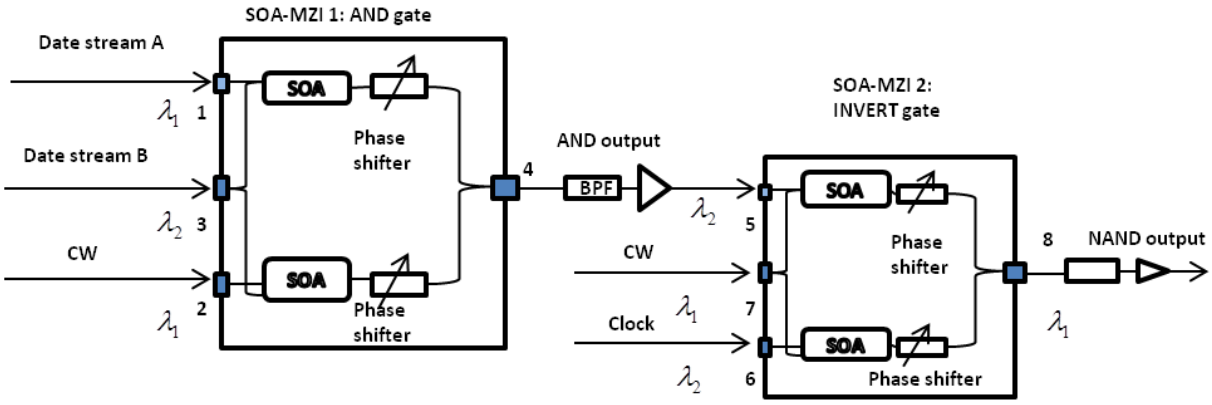

Figure 3.1: Schematic of a NAND logic gate using two Mach-Zehnder interferometers in series configuration.

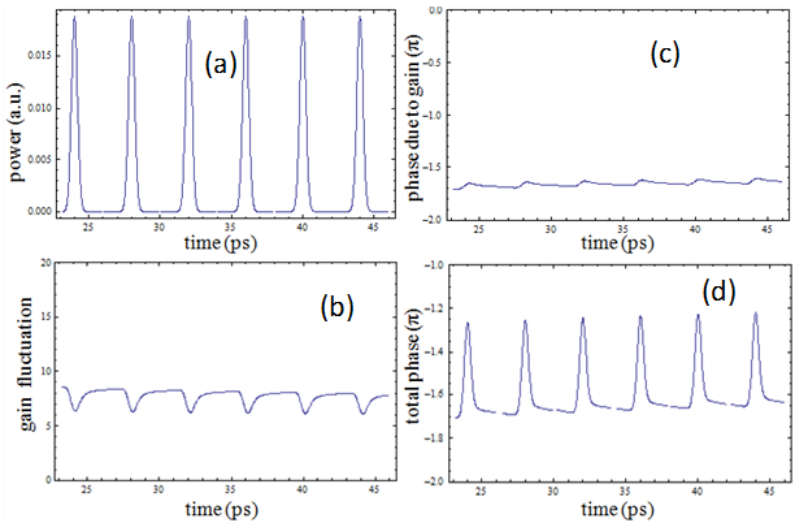

Figure 3.2: Calculated gain and phase change in a SOA due to a series of pulses shown in (a). (b) - gain modulation as a function of time, (c) – cross phase modulation (XPM) due to carrier density modulation as a function of time, (d) - total phase modulation including two-photon absorption as a function of time. Note the periodic total phase change is primarily due to two-photon abs. in (d).

The temporal gain and phase change in the SOA has been analyzed by a numerical solution of the SOA rate equations taking into account two-photon absorption. The time dependent gain of the SOA satisfies the temporal gain rate equations [16, 17]:

$$\frac{dh_l(t)}{dt} = \frac{h_0 - h_l(t)}{\tau_c} - \frac{P(t)}{E_{sat}}\left[e^{h_{total}(t)} - 1\right] \tag{3.3}$$

$$\frac{dh_{CH}(t)}{dt} = -\frac{h_{CH}(t)}{\tau_{CH}} - \frac{\varepsilon_{CH}}{\kappa\tau_{CH}}\left[e^{h_{total}(t)} - 1\right]P(t) \tag{3.4}$$

$$\frac{dh_{SHB}(t)}{dt} = -\frac{h_{SHB}(t)}{\tau_{SHB}} - \frac{\varepsilon_{SHB}}{\kappa\tau_{SHB}}\left[e^{h_{total}(t)} - 1\right]P(t) - \frac{dh_l(t)}{dt} - \frac{dh_{CH}(t)}{dt} \tag{3.5}$$

where h(t) is an integral of contributions of different gain saturation processes over the effective length of SOA and h_{total} equals the sum of h_l, h_{CH}, and h_{SHB}. τ_c is the carrier lifetime, $\exp[h_0]=G_0$ is the unsaturated power gain, $E_{sat}=P_{sat}\tau_c$ is the saturation energy of the SOA, P_{sat} is the SOA's saturation power, $P(t)=\kappa S(t)$ is the input pump power inside the SOA active region, S(t) is the intensity, and $\kappa=\hbar\omega\sigma v_g$ is the conversion factor between the two; σ is SOA active region cross section, v_g is group velocity is SOA; $h_l(t)$, $h_{CH}(t)$, and $h_{SHB}(t)$ are gain factor functions for linear gain and gain contributed by carrier heating and spectral hole burning effects, respectively. Eqs. (3.4) and (3.5) account for the intraband carrier dynamics. The carrier density induced phase change is given by:

$$\phi(t) = -\frac{1}{2}\left[\alpha h_d(t) + \alpha_{CH} h_{CH}(t)\right] - \frac{1}{2}\beta\alpha_2 S(t) L \tag{3.6}$$

where α is the linewidth enhancement factor (i.e. α=5), α_{CH} is the carrier heating alpha factor (i.e. $\alpha_{CH}=1$), other SOA parameters are as follows: P_{sat}=30mW, G_0=10dB, τ_c=30ps, τ_{FWHM}=0.5ps, τ_{SHB}=100fs, τ_{CH}=300fs, $\varepsilon_{SHB}=\varepsilon_{CH}=0.2m^2/W$ [15, 16]. Note that a low gain of 10dB reduces the amount of gain induced phase change which is slower than the two-photon absorption related phase change. And the second term in Eq. (3.6) is due to two-photon

absorption. Here, we use α_2=-4 [10, 11].

The total phase dynamics used in the model here includes both the fast (TPA induced) phase change and the relatively slow cross phase modulation and cross gain modulation induced phase change. The calculated change in gain and phase as a function of time when a pulse train @ 250 GHz is injected into the SOA is shown in Figure 3.2. The pulse width (full width at half maximum) is 0.5 ps, the average power is 21 mW and the SOA cross section is 0.5 μm^2.

3.3 Function and Schematic of all optical latches

The Set-Reset Latch can be considered as one of the most basic logic circuit possible. This simple latch is basically a one-bit memory bistable device that has two inputs, one of which will "SET" the device (meaning the output = "1"), and another which will "RESET" the device (meaning the output = "0"). Then the SR description stands for "Set-Reset". The reset input resets the flip-flop back to its original state with an output Q that will be either at a logic level "1" or logic "0" depending upon this set/reset condition. The simplest way to make Set-Reset Latch is to connect together a pair of cross-coupled 2-input NAND gates. The schematic of Set-Reset Latch and the truth table for the Set-Reset function are shown in Figure 3.3. In addition, Figure 3.4 shows the schematic of the S-R latch with the all-optical NAND gates (from Figure 3.1) explicitly drawn in the schematic of Figure 3.3.

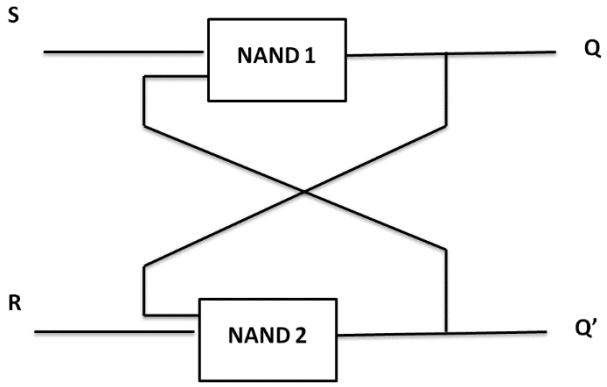

S	R	Action
0	0	Restricted Combination
0	1	Q=1, Q'=0
1	0	Q=0, Q'=1
1	1	No Change

Figure 3.3: The left figure is the schematic of the Set-Reset Latch. The right figure is the truth table for the Set-Reset function.

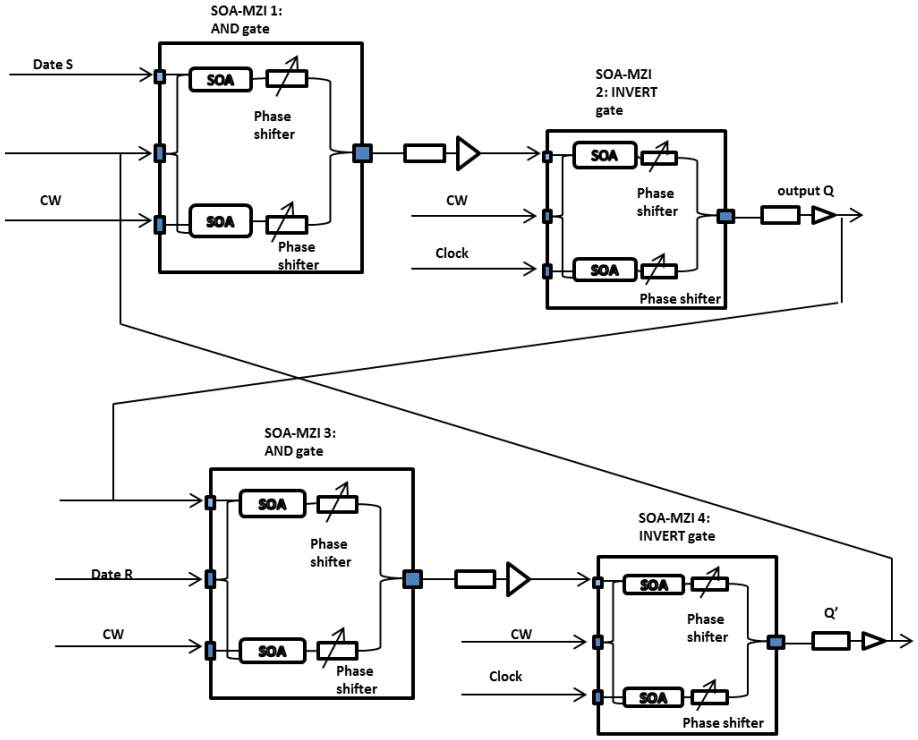

Figure 3.4: Schematic of a Set-Reset latch. The figure shows all the SOA-MZIs.

The D-Flip-Flop is widely used as the building block of a logic function. It is also known as a data or delay flip-flop. The D-Flip-Flop captures the value of the D-input at a definite portion of the gate cycle (such as the rising edge of the gate). That captured value becomes the Q output. At other times, the output Q does not change. The D- Flip-flop can be viewed as a memory cell, a zero-order hold, or a delay line. We can use the NAND and NOT gates to make a D-Flip-Flop. The schematic of D-Flip-Flop and the truth table for D-Flip-Flop function are showed in Figure 3.5. Similarly, Figure 3.6 shows the schematic of the D-Flip-Flop with the all-optical NAND gates (from Figure 3.1) explicitly drawn in the schematic of Figure 3.5.

3.4 Simulation result and output quality evaluation

For NAND operation, we assume the data stream pulses (A and B) to be Gaussian pulses, i.e.

$$P_{A,B}(t) = \sum_{n=-\infty}^{+\infty} a_{nA,B} \frac{2\sqrt{\ln 2}P_0}{\sqrt{\pi}\tau_{FWHM}} \exp\left(-\frac{4\ln 2(t-nT)^2}{\tau_{FWHM}^2}\right) \quad (3.7)$$

where P_0 is the energy of a single pulse, $a_{nA,B}$ represents n_{th} data in data stream A and B, $a_{nA,B}$= 1 or 0. To simulate the NAND gate performance, we assume both input signals are of RZ type. The pseudo random sequence is generated using a random number generator in the software used for modeling. Simulated results of logic gate NAND is shown in Figure 3.7. Similar process is used for generation of Set/Reset pulses for S-R latch and Data/Gate pulses for D-Flip-Flop respectively. The output eye-diagram is also plotted to show the output quality.

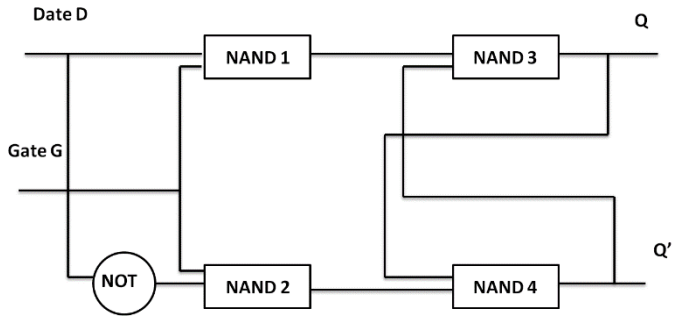

Gate	D	Q next
Rising edge (1)	0	0
Rising edge (1)	1	1
Non-Rising (0)	*	Q

Figure 3.5: The left figure is the schematic of the D-Flip-Flop. The right figure is the truth table for D-Flip-Flop function.

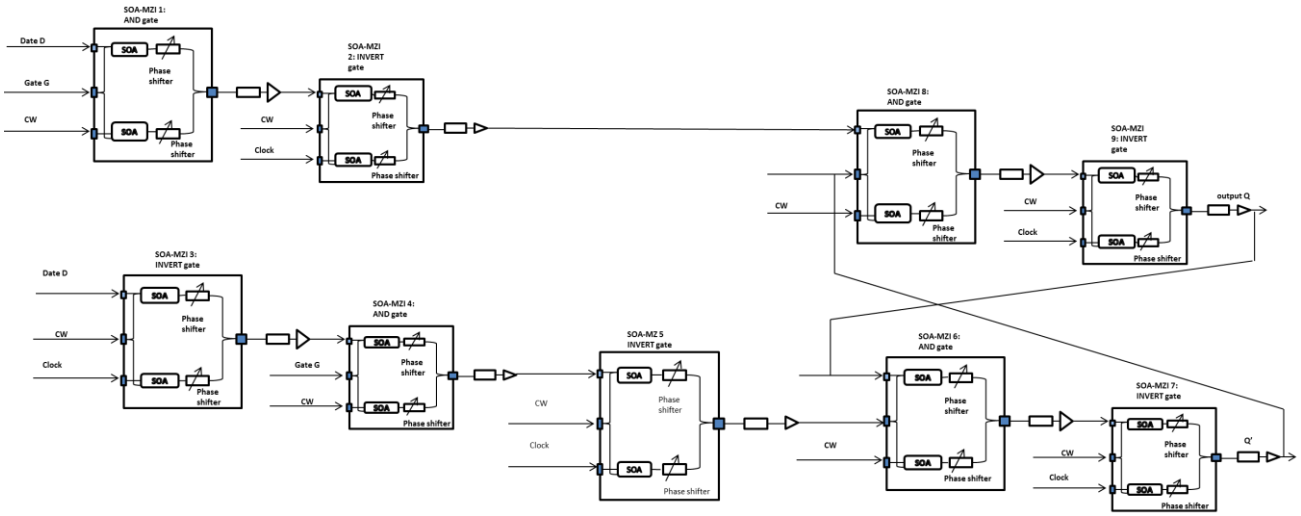

Figure 3.6: Schematic of a D-Flip-Flop. The figure shows all the SOA-MZIs.

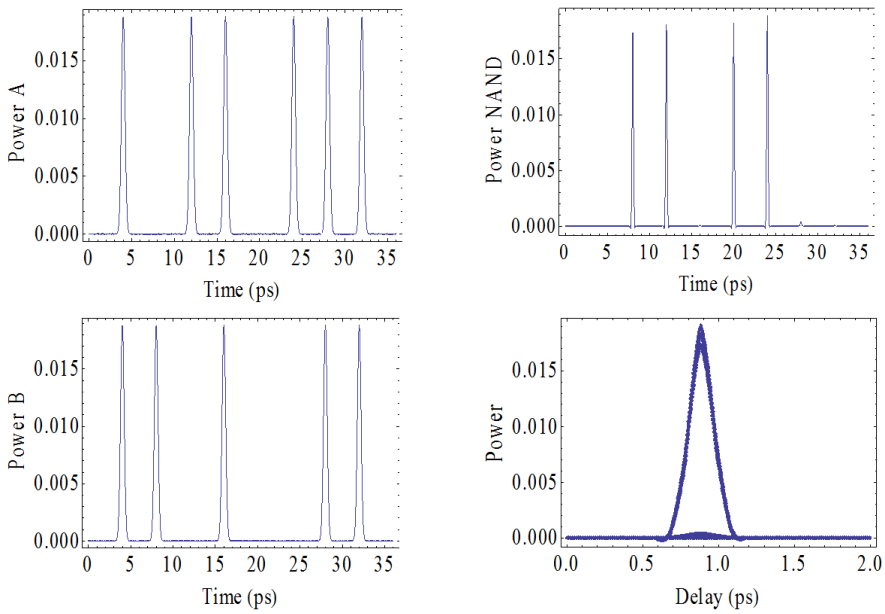

Figure 3.7: Date A and Date B are shown in the left. Simulated results of output (NAND) and eye pattern of the output (Q) are shown in the right. The above set of figures is for 250Gb/s data rate.

Figure 3.7 shows the calculated NAND results for 250 Gb/s input data using the above equations, signal A has (10110111) pattern, and signal B has (11010011) pattern. Signals A and B are on the left and the NAND (01101100) output is on the upper right. The bottom right shows the eye diagram. The eye diagram is obtained by superimposing the output of 50 separate pseudo random sequence of A and B input pulses. The Q value is given by $Q = (S_1-S_0)/(\sigma_1+\sigma_0)$, where S_1, S_0 are the average intensities of the expected "1"s and "0"s and σ_1 and σ_0 are standard deviations of those intensities. The calculated Q is 12 which represent a very low error rate. The simulated results for a 250 Gb/s input set and reset pulses are shown in Figure 3.8.

The performance of the S-R latch is better illustrated using longer set and reset pulses. The S-R latch for this case has been simulated using the rate equations. The result is shown in Figure 3.9. Please note that if R= 1, S=0 then Q becomes 1 (@ ~ 20 ps in Figure 8) ; also Q remains set at 1 even if R becomes 0 (after ~ 40 ps in Figure 8) , if S=0. If R=0, S=1 then Q becomes 0 when S turns on (S=1) (e.g. @ 70 ps in Figure 8) i.e. Q resets to 0 when S turns on. Please also note that if R=1, S=1 there is no change in Q from previous state (i.e. Q remains 0, e.g. @ ~ 100 ps in Figure 8). When, R=1 and S=0 (@~110 ps in Figure 8), Q becomes to 1 as expected for a Set/Reset function.

The simulated results for D-Flip-Flop latch are shown in Figure 3.10 and from this simulated results, we show that all-optical Set-Reset latch and D-Flip-Flop operation @ ~ 250 Gb/s is feasible.

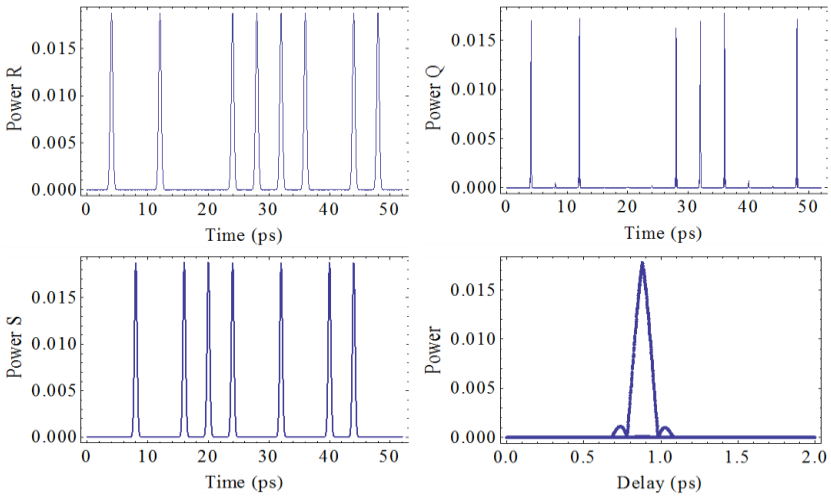

Figure 3.8: Set and Reset signals are shown in the left. Simulated results of output (Q in Figure 3.3) and eye pattern of the output (Q) are shown in the right. The above set of figures is for 250Gb/s data rate.

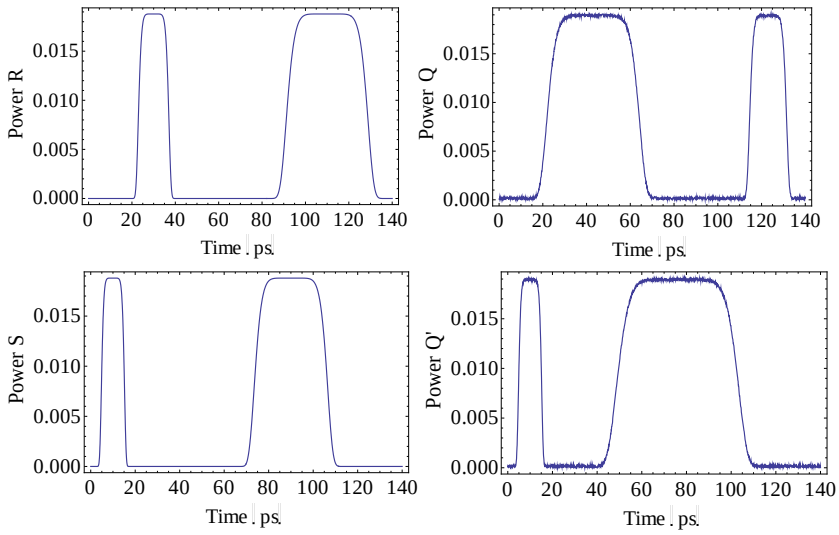

Figure 3.9: Set and Reset signals are shown in the left. Simulated results of output (Q in Figure 3.3) and inverse of Q (Q') are shown in the right. Note that if R= 1, S=0 then Q becomes 1 (@ ~ 20 ps) ; also Q remains set at 1 even if R becomes 0 (after ~ 40 ps) , if S=0. If R=0, S=1 then Q becomes 0 when S turns on (S=1) (e.g. @ 70 ps) i.e. Q resets to 0 when S turns on. Please also note that if R=1, S=1 there is no change in Q from previous state (i.e. Q remains

0, e.g. @ ~ 100 ps). Q' (Q-bar) is inverse of Q.

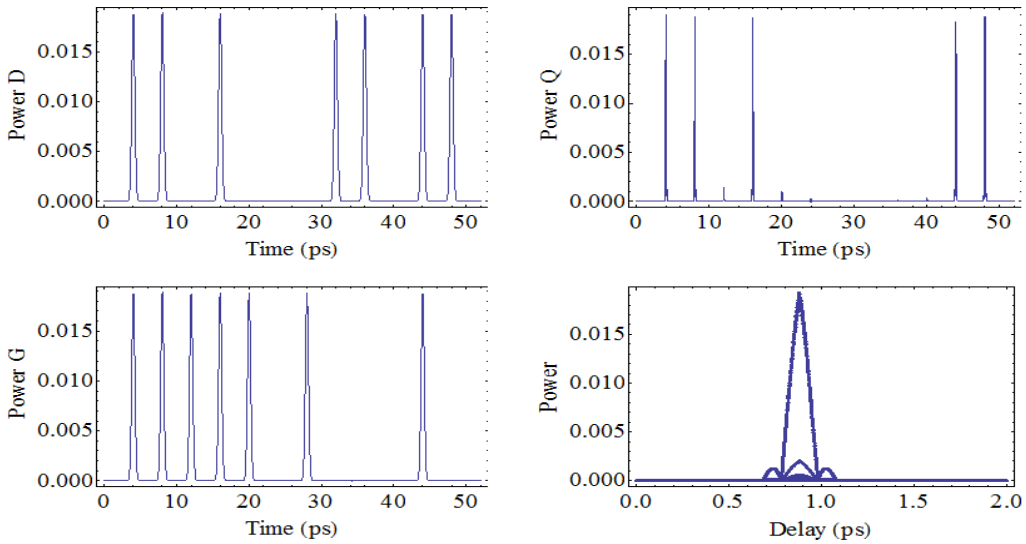

Figure 3.10: Date (D) and Gate (G) are shown in the left. Simulated results of output (Q in Figure 3.5) and eye pattern of the output (Q) are shown in the right. The above set of figures is for 250Gb/s data rate.

The total phase dynamics used in the model here includes both the fast (TPA induced) phase change and the relatively slow cross phase modulation and cross gain modulation. The latter processes are slow and hence they cause “pattern effect” at high speeds (~ 250 Gb/s) i.e. the phase change caused by an individual bit (e.g. bit 1) depends on the prior sequence of bits. This phenomenon results in a change in the shape of the output NAND pulses, noise, and, timing jitter. The eye diagrams for NAND, S-R latch, and, D-Flip-Flop are different because the input pulses undergo different number of all-optical logic (NAND) gates. For example: in the S-R latch the input pulses pass through two “NAND” gates and in the D-Flip-Flop system the input pulses pass through four “NAND” gates. Hence for the three all-optical logics discussed here, the input pulses undergo different amounts of nonlinear logic processing which results in the differences in the amount of noise accumulation and timing jitter in the output pulses and the eye diagrams.

The Q-factor dependence on date rate and input peak power has been calculated. It is shown in Figure 3.11, which shows that for sufficient large input power (average power > 18dBm), the optical latches has good quality factor (Q > 6) at high data rates up to 250Gb/s. This can be explained as at low power levels, the phase due to TPA is small, and the pattern effect due to slower gain change induced phase change is more significant. As the injected power increases, the TPA induced fast phase modulation becomes a major contribution of the total phase shift, and the pattern effect becomes relatively small, resulting in higher Q-factor.

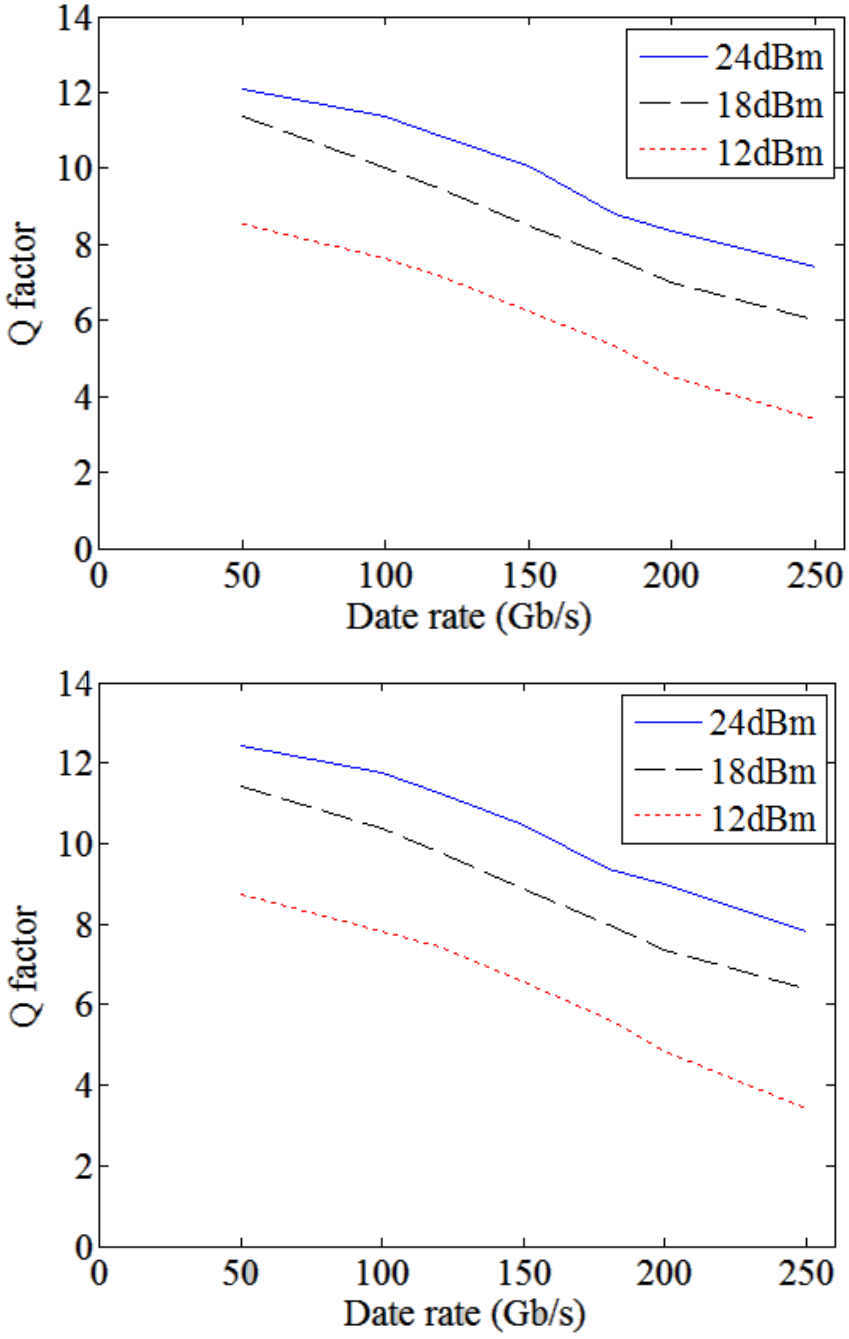

Figure 3.11: The calculated quality factor Q at different operating bit-rates and different input data stream average powers. (top: D-Flip-Flop, bottom: Set-Reset Latch).

3.5 Conclusion

In this chapter I designed and modeled high speed all optical Set-Reset Latch and D-Flip-Flop which are built using two optical logic operations NAND and NOT. Both NAND and NOT operations are realized using the ultrafast phase response during two-photon absorption (TPA) process in semiconductor optical amplifiers (SOA) in this model. Results show that this scheme can perform the basic function of Set-Reset Latch and D-Flip-Flop at high bit-rates of ~ 250 Gb/s. The impact of the output quality (Q factor) on operation speed and input data stream average power has been studied and discussed. Results show that for best output quality and high data rate operation (~ 250Gb/s), this system requires sufficient large input average power (average power > 18dBm) and narrow input pulse width (FWHM~0.5ps).

Chapter 4 High Speed All-Optical Encryption and Decryption using QD-SOA

4.1 Introduction

Encryption and decryption has long been used by governments to facilitate secret communication. It is now commonly used in protecting information within many kinds of civilian systems. For example, encryption can be used to protect data being transferred via internet, mobile telephones, wireless intercom systems and prevent unauthorized use or reproduction of copyrighted material. In an encryption scheme, the message is encrypted using an encryption algorithm. This is usually done with the use of an encryption key, which specifies how the information is to be encoded. An encryption scheme usually needs a key-stream generator to randomly produce keys. The pseudorandom bit sequence (PRBS) can be used as the key for encryption and decryption.

In future high speed all-optical communications, all-optical data processing will be important [1]. The pseudorandom bit sequence (PRBS) using linear feedback shift registers (LFSR), which were first introduced in electronics, are characterized by its simplicity of generation, good repeatability and statistical properties [2]. It thus received wide application, including in simulation of noise in signal transmission, data encryption/decryption, and in bit error rate testers (BERT) [3]. The recent achievements in photonics signal processing spurred more interest towards realizing high speed all-optical PRBS generation. A pseudorandom bit sequence (PRBS) can be generated using a linear feedback shift register (LFSR) [3-4]. The

PRBS sequence generated with a shift register of length m has a period of 2^m-1. To generate a stable optical PRBS sequence using LFSR, an optical XOR logic gate is needed. In recent years, demonstrations of high speed all-optical XOR logic gates using different schemes were reported, including using semiconductor optical amplifier loop mirror (SLALOM) with data rates of ~10Gb/s [5], ultrafast nonlinear interferometer (UNI) with data rates of ~20Gb/s [6], and the SOA based Mach-Zehnder interferometer (SOA-MZI) with data rates of ~20Gb/s [7-8]. Among these schemes, the quantum dot (QD) SOA-MZI based XOR gate is presently a suitable design for high data rates of ~ 250Gb/s [9].

In this chapter, I presented a model to simulate the process of encryption and decryption. The encryption algorithm and the key we used in this model are XOR operation and pseudorandom bit sequence (PRBS). Both of the high speed all-optical XOR operation and PRBS are realized by using the QD-SOA Mach-Zehnder interferometer. Furthermore, I also designed and investigated two other kinds of more secure key-stream generators: cascaded design and parallel design, which are based on linear feedback shift registers (LFSR). Results show that encryption and decryption using key-stream generators can be realized at high date rates (~250Gb/s).

4.2 Schematic of Encryption and Decryption

We can use the logic XOR operation to realize the encryption and decryption of the message. The message can be encrypted by applying the bitwise XOR operation to every character

using a given key. To decrypt the coded message, we merely reapply the XOR operation with the same key which is used for encryption. The schematic of encryption and decryption using the same key are shown in Figure 4.1.

In this chapter, we use a QD-SOA MZI system to realize high speed all-optical XOR logic operation which is used for encryption and decryption. The principle of the logic XOR operation based on SOA-MZI has been discussed and analyzed [9, 10-11]. As shown in Figure 4.2, the data stream A and B (at λ_1) are injected to two identical QD-SOA arms, a clock signal (at λ_2) which is used as control beam is equally split and fed into the two arms. The two data streams modulate the gain and phase that the clock signal experiences in each of the QD-SOAs via cross gain modulation (XGM) and cross phase modulation (XPM) [12]. Two phase shifters are used in the MZI arms so that the clock streams through the two arms acquire π phase difference at port 4. In this way, when the two clock streams recombine at port 4 with their amplitude and phase modulated, they will interfere to produce different results under different conditions. If input to port 1 and 2 are the same (either both“0” or both“1”), the clock streams arriving at port 4 will experience the same gain and phase shift in the QD-SOAs and will undergo destructive interference due to the π phase difference between the arms and produce output result “0;” if input bits are different (one is “0” and the other is “1”), the clock streams will experience different gain and phase shift, and the interference result at port 4 will be “1.” This results in XOR operation

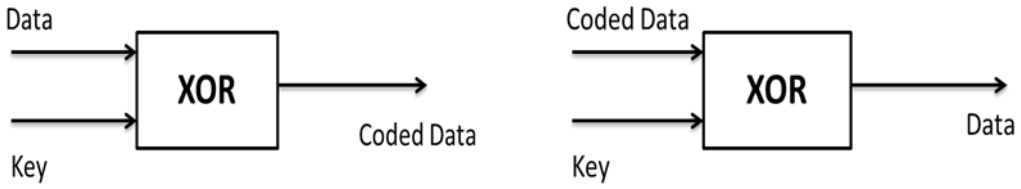

Figure 4.1: The left figure is the schematic of encryption. The right figure is the schematic of decryption. The same key stream is used for both encryption and decryption.

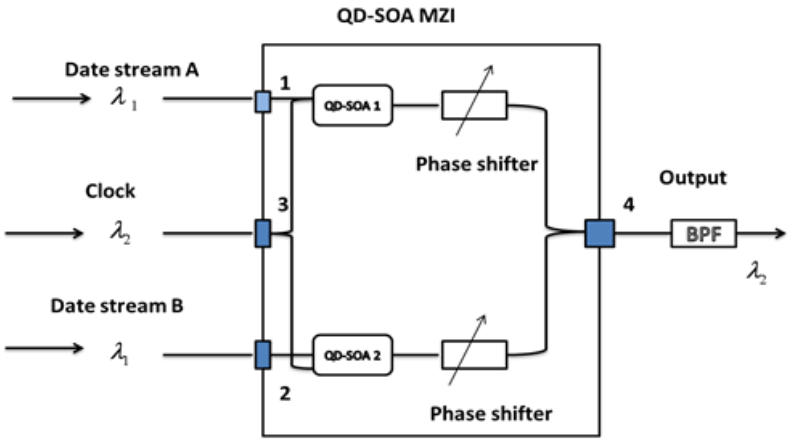

Figure 4.2: Schematic of QD-SOA Mach-Zehnder Interferometer. BPF: bandpass filter centered at λ_2

We can also use a MZI scheme [13] to realize logic AND operation. By putting data A to port 1 and data B to port 3, we can get gain modulated pattern of data B out of port 4 resembling logic A AND B. To make results better in quality, a low power CW light is used into port 2 to cancel out the background noise of date stream A. Similarly, if we use a clock as date B which is put into port 2, put data A into port 1, and use optical CW as control beam into port 3, we can get out of port 4 data pattern of A XOR "1", which is the same in terms of truth value as "INVERT A".

4.3. Generation of the key

The key we used for encryption and decryption is high speed all-optical pseudo random bit sequence (PRBS) which is generated by a linear feedback shift register (LFSR) composed of QD SOA-based logic XOR and AND gates, shown in Figure 4.3(a). An LFSR has m data storing units (optical delay line in all-optical system), each unit is capable of storing one binary data bit for one clock period [14]. The whole system is synchronized with a clock. At each period, the n_{th} and m_{th} bit go through an XOR process [8]. Their XOR result gets reshaped and its wavelength is converted back to system's operation wavelength through an AND gate, and then goes back to the front of LFSR. The output PRBS signals can be tapped from the end of the LFSR. Figure 4.3(b) shows the design of the logic functional unit. The main parts of this unit are two Mach-Zehnder interferometers (MZI) each arm of which has a semiconductor optical amplifier (SOA) with a quantum dot (QD) active region. The first MZI serves as an all-optical logic XOR gate for the two bits (m, n), while the other MZI serves as

logic AND gate.

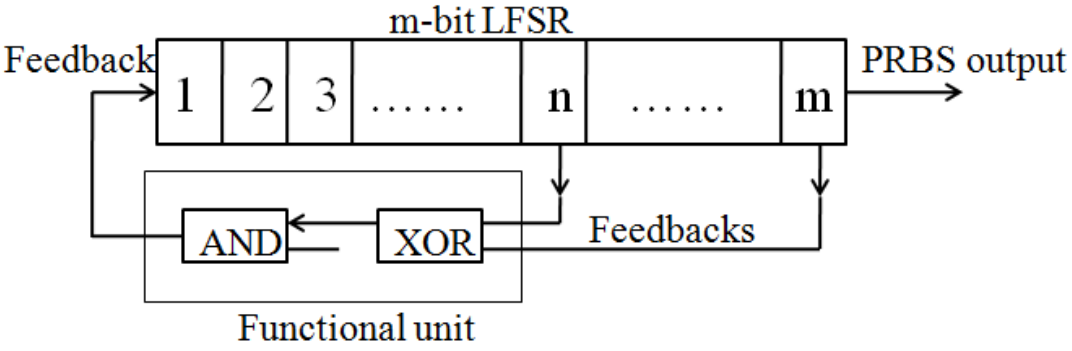

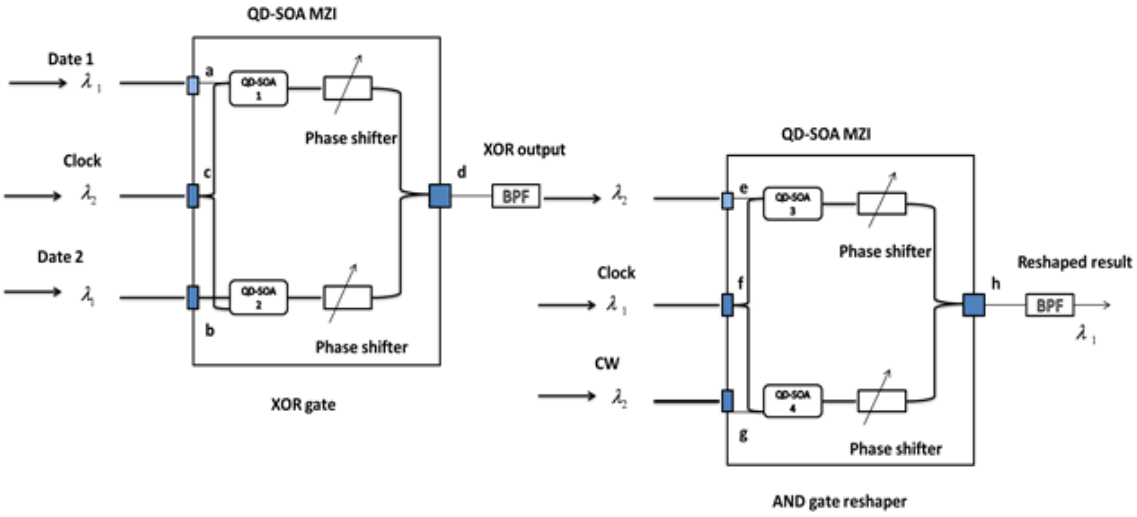

Figure 4.3: Design of PRBS generator. (a): Block diagram of a LFSR (b): functional unit, including two QD-SOA MZIs operating as XOR and AND gates.

After a band-pass filter centered at λ_2, the XOR result of data 1 and 2 enters the input port "e" of a logic AND gate. The LSFR operation begins by using a low power CW light as input to the arm of the second MZI (AND function). The clock signal (at wavelength λ_1) is injected into the center port. In our case, we want to reshape the XOR result, so we choose to make AND operation between XOR result and "1." This bit "1" is from a clock pulse train centered at λ_1, injected to port "f." After another band-pass filter centered at λ_1, the AND result represents a reshaped replica of the XOR result, and its wavelength is converted back to λ_1 that circulates in the LFSR.

The PRBS sequence generated using this scheme has a repetition bit period of $T=2^m-1$. Basically, the PRBS sequences are different from truly random bit sequences in that the latter has a continuous spectrum while the former has a discrete spectrum with harmonics [15]. As m increases the generated PRBS spectrum becomes more and more continuous and the output can better represent a truly random signal. The frequency space between two neighboring lines in the frequency spectrum of PRBS sequences is given by [15]

$$\Delta f = \frac{f_b}{2^m - 1} \tag{4.1}$$

where f_b is the bit rate. From the above equation, we can see as m increases the frequency space becomes smaller which means the PRBS frequency spectrum becomes more and more continuous. Thus, as m increases the randomness of PRBS sequence becomes better

I also design two other kinds of more secure key-stream generators, cascaded design and parallel design, shown in Figure 4.4 and Figure 4.5.

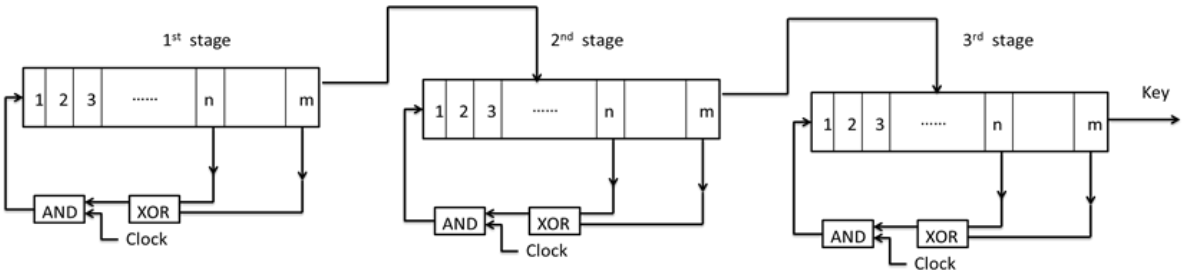

Figure 4.4: Block diagram of cascaded designed key-stream generator

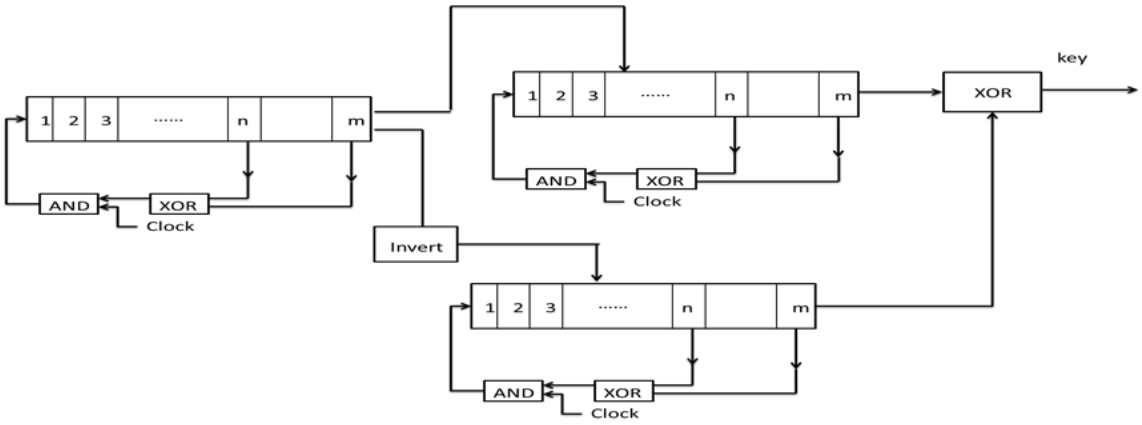

Figure 4.5: Block diagram of parallel designed key-stream generator

This cascaded design consists of three cascaded linear feedback shift registers (LFSR) which can generate all-optical PRBS. The output of the first LFSR can be used as the input of the second LFSR and the output of the second LFSR can be used as the input of the third LFSR. All these three LFSR are realized using the QD-SOA MZIs.

This parallel design is composed of three linear feedback shift registers (LFSR), an INVERT gate and a XOR gate. The output of the first LFSR and its invert are used as the input of the second LFSR and the third LFSR respectively. The final output is the XOR of the output of second LFSR and third LFSR. The three LFSR and all the logic gates are realized by using QD-SOA MZIs.

It is known that the randomness and the length of the key are the most important two factors which decide the security of the key. If the key is more random and is at least as long as the message, the XOR cipher is much more secure than when there is key repetition within a message[16]. For example, if the key is truly random, as long as the message and only used once, we can use this kind of key to construct a perfect encryption scheme which is called one-time pad. Assuming an eavesdropper cannot get access to the key used to encrypt the message; this one-time pad scheme is perfectly secure. Since every plaintext message is equally possible, there is no way for the crypt analyst to determine which plaintext message is the correct one. A random key sequence added to a nonrandom plaintext message produces a completely random cipher text message and no amount of computing power can change that [17].

For a PRBS sequence whose repetition bit period is $T=2^m-1$, as m increases the randomness of the generated PRBS becomes better. However, when m increases, the number of different input for LFSR becomes larger. For example, if m=7, there are 2^7 different kinds of input for LFSR. Thus, it becomes difficult to choose the input for a single LFSR in order to generate different PRBS when m becomes larger. However, the above cascaded design and parallel design can serve as better key-stream generators for generating longer (big m) and different keys because we can use the output of previous stage as the input of next stage which solves the difficulty of choosing and changing the input for one single LFSR. In addition, the algorithms of the cascaded design and parallel design are much more complicated compared to that for a single LFSR, which makes the generated keys much harder to break. Overall, the cascaded design and parallel design can generate more secure keys than a single LFSR.

4.4. QD-SOA rate equations and nonlinear effects

The device we chose here is the InAs/GaAs QD-SOA, with InAs quantum dots embedded in GaAs layers [12, 18-21]. This type of device has a typical gain of ~15 dB gain around 1550nm band, with noise figure as low as 7 dB [20]. The device gain is nearly polarization-independent [21].

The carrier transitions between various states in the QD-SOA are described by the following rate equations [22-23]:

$$\frac{dw}{dt} = \frac{I}{eVN_{wm}} - \frac{w}{\tau_{wr}} - \frac{w}{\tau_{w-e}}(1-h) + \frac{N_{esm}}{N_{wm}}\frac{h}{\tau_{e-w}}(1-w) \tag{4.2}$$

$$\frac{dh}{dt} = -\frac{h}{\tau_{esr}} + \frac{N_{wm}}{N_{esm}}\frac{w}{\tau_{w-e}}(1-h) - \frac{h}{\tau_{e-w}}(1-w) + \frac{N_{gsm}}{N_{esm}}\frac{f}{\tau_{g-e}}(1-h) - \frac{h}{\tau_{e-g}}(1-f) \tag{4.3}$$

$$\frac{df}{dt} = -\frac{f}{\tau_{gsr}} - \frac{f}{\tau_{g-e}}(1-h) + \frac{N_{esm}}{N_{gsm}}\frac{h}{\tau_{e-g}}(1-f) - \frac{\Gamma_d}{A_d}a(2f-1)\frac{1}{N_{gsm}}\frac{S(t)}{\hbar\omega} \tag{4.4}$$

where w, h and f are the occupation probability of the wetting layer, the QD excited state and ground state, respectively; N_{wm}, N_{esm} and N_{gsm} are the maximum density of carriers in each state; τ_{ar} ("a" being "w," "es" or "gs") is the spontaneous radiation lifetime of each state; $\tau_{a\text{-}b}$ is the relaxation lifetime between any two states "a" and "b"; I is the injected bias current; Γ_d is the active layer confinement factor; V is the effective volume of the active layer; a is the differential gain; A_d is the effective cross-sectional area of the active layer and S(t) is the total input light power.

The gain of QD-SOA which results from carrier density dynamics, including nonlinear processes like carrier heating (CH) and spectral hole burning (SHB) effects [24-25], is expressed as:

$$g(t) = \frac{a(N - N_t)}{1 + (\varepsilon_{CH} + \varepsilon_{SHB})S(t)} \tag{4.5}$$

where N is the GS carrier density, N_t is the transparent GS carrier density; ε_{CH} and ε_{SHB} are the gain suppression factors for carrier heating and spectral hole burning effect, respectively.

The injected light and temperature change due to carrier heating also changes the refractive index of the active region, and thus a phase change to any probe wave injected.

$$\phi(t) = -\frac{1}{2}(\alpha G_l(t) + \alpha_{CH}\Delta G_{CH}(t)) \tag{4.6}$$

where $G_l(t)=e^{g(t)l}$ is the linear gain factor of the device with l being the effective length of the

active layer, α and α_{CH} are the linewidth enhancement factors of the device corresponding to band-to-band transition and carrier heating process, respectively [26, 27]. The linewidth enhancement factor due to spectral hole burning (SHB) is ~0.

When the two clock streams recombine at the output port, their interference power can be expressed as:

$$P_{out}(t) = \frac{P_{cb}(t)}{4}[G_1(t) + G_2(t) - 2\sqrt{G_1(t)G_2(t)}\cos(\phi_1(t) - \phi_2(t) + \phi_0)] \quad (4.7)$$

where P_{cb} is the input clock signal light power, $G_1(t)$ and $G_2(t)$ are the total gain factors of the two MZI arms respectively, $\phi_0=\pi$ is the initial phase difference added by the phase shifters located in the MZI arms.

4.5 Simulation Results

Parameters chosen for simulation in this work are experimental results on QD-SOAs for central wavelength: 1.55μm: $\tau_{wr}=\tau_{esr}$=200ps, τ_{gsr}=50ps, $\tau_{w\text{-}e}$=3ps, $\tau_{e\text{-}w}$=300ps [28], $\tau_{g\text{-}e}$=10ps, Γ_d=10%, linewidth enhancement factors α=4, α_{CH}=0.2 [26,27], QD energy levels' densities of states, $n_w=5.4\times10^{17}cm^{-3}$, $n_w:n_e:n_g\approx15:2:1$ [23], QD areal density is $7.5\times10^{10}cm^{-2}$, saturated output power is 18dBm at 1.55μm wavelength [20], device differential gain $a=8.6\times10^{-15}cm^2$ [19], effective length l=1.0mm, noise figure F=7dB [20], transparency pump current density is ~0.2kA/cm^2 [24], gain suppression factors are $\varepsilon_{CH}=0.5\times10^{-23}m^3$, $\varepsilon_{SHB}=7.5\times10^{-23}m^3$ [29], which correspond to threshold input pulse energy for both nonlinear effects ~0.47pJ, Value of time constant $\tau_{e\text{-}g}$ has been measured in many experiments, the smallest report value is ~0.1ps [24]

and the largest measured value goes up to several picoseconds [21]. We have not taken into account the inhomogeneous broadening associated with different dot sizes. But it is indirectly taken into account in the form of spectral hole burning. In a QD the inhomogeneously broadened spectrum range could be small because it requires carrier transport among QDs: a QD has discrete transition wavelengths and carrier relaxation to another wavelength involves transition to another QD [25]. The simulated results of encryption and decryption for the QD-SOA based XOR operation are shown in Figure 4.6. Input data is on the top right and a key (chosen any of bots in this case) is shown on top left. The encrypted in XOR of the input data and key is shown on bottom left. The decrypted data which should be the original data is shown on bottom right. Note that top right and bottom right traces are identical as it should be.

From the above simulated results, we can see the decrypted data is the same as the input data. Thus, we prove that all-optical encryption and decryption operation at ~250Gb/s is feasible. We also calculate the Q factor for the decrypted data in Figure 4.6. The Q factor is 8.7, which means a good quality of the decrypted data.

The key used for encryption and decryption is high speed all-optical pseudo random bit sequence (PRBS). The all-optical PRBS generated by a 7-bit optical LFSR is simulated by modeling the logic XOR and AND operations in the QD-SOAs as shown in Figure 4.7.

The simulation results of cascaded design and parallel design key stream generators are shown in Figures 4.8 and Figure 4.9 respectively.

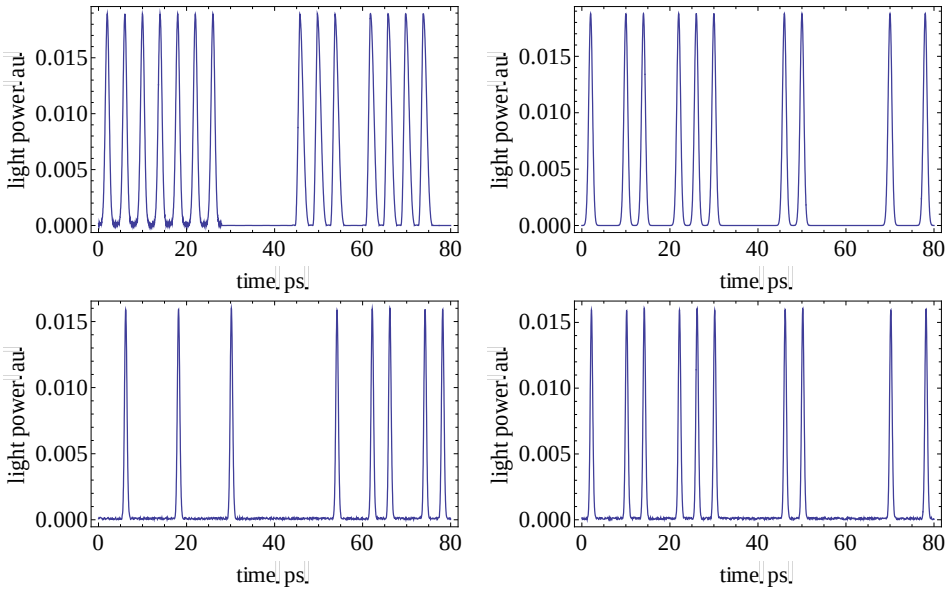

Figure 4.6: Input date is shown at the top-right corner and key is shown at the top-left corner. Simulated results of encrypted data and decrypted data are shown at the bottom-left corner and bottom-right corner respectively. The above set of figures is for 250Gb/s data rate.

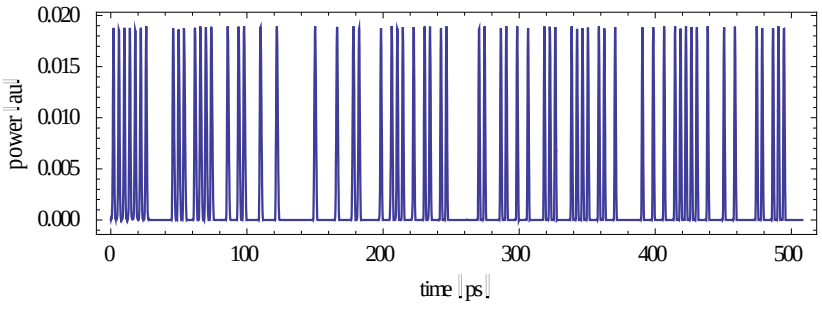

Figure 4.7: Simulation result of PRBS sequences generated by 7-bit LFSR, operating at 250Gb/s. The input of all-optical LFSR is seven “1”s.

As shown in figure 4.8 and 4.9, the cascaded design and parallel design key-stream generators operating at ~250Gb/s is feasible. Thus, we can use these two kinds of key-stream generators to produce various more secure keys.

4.6. Conclusion

In this chapter we designed and modeled high speed all-optical encryption and decryption systems using key-stream generators and XOR gate based on quantum-dot semiconductor optical amplifiers (QD-SOA). Results show that this all-optical model can realize the basic function of encryption and decryption at high bit-rates of ~ 250 Gb/s. Three kinds of key-stream generators based on QD-SOA, single LFSR, cascaded design and parallel design, have been designed and simulated. Results show that all of these three key-stream generators operating at ~250Gb/s are feasible and the cascaded design and parallel design are suitable for producing more secure keys.

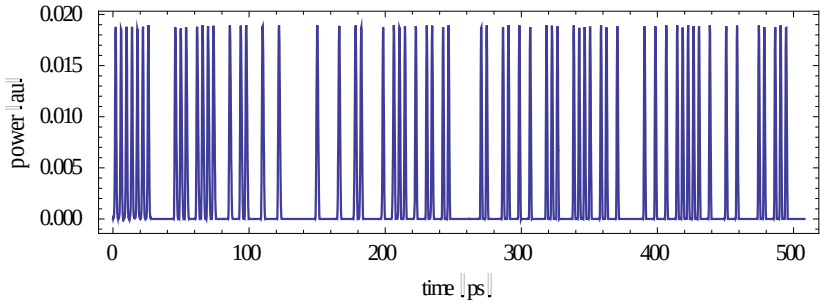

(a)

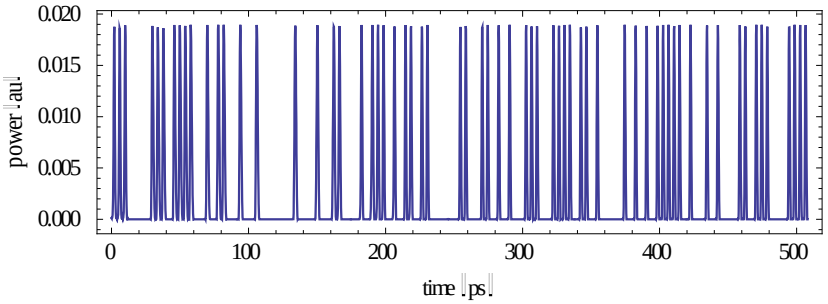

(b)

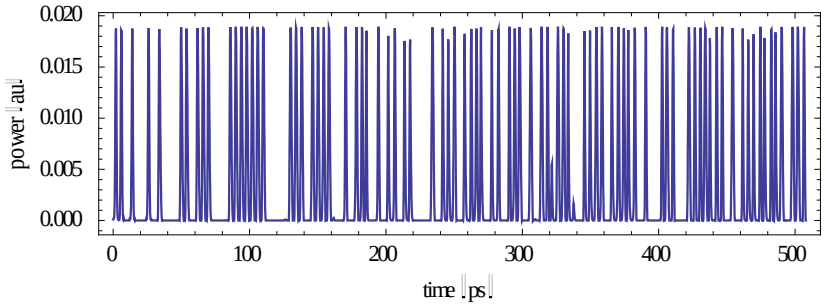

(c)

Figure 4.8: (a) Simulation result of the first stage in cascaded design, input is seven "1"; (b) Simulation result of the second stage in cascaded design, input is "8th-14th" of the output of the first stage; (c) Simulation result of the third stage in cascaded design, input is "15th-21st" of the output of the second stage

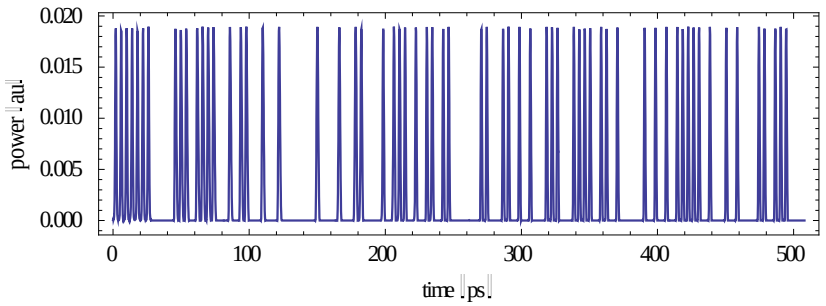

(a)

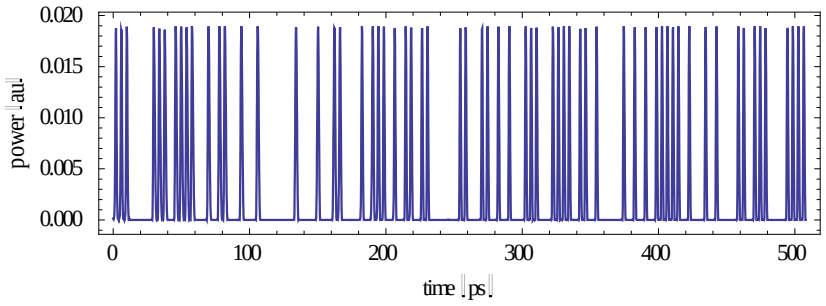

(b)

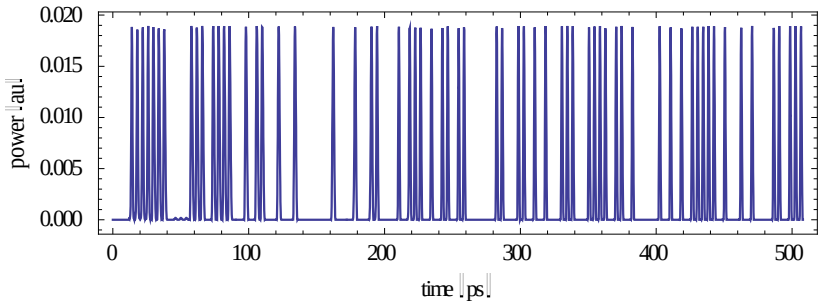

(c)

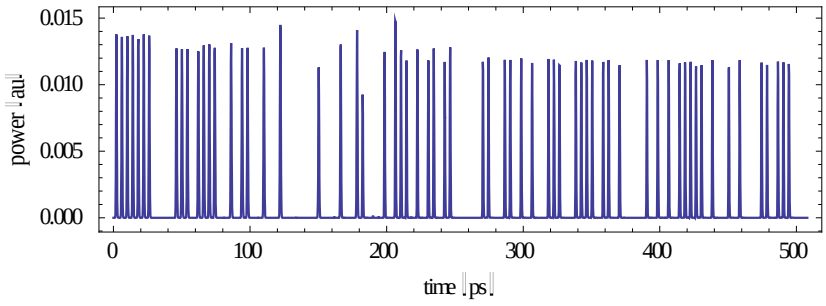

(d)

Figure 4.9: (a) Simulation result of the first LFSR in parallel design, input is seven "1"; (b) Simulation result of the second LFSR in parallel design, input is "8th-14th" of the output of the first LFSR; (c) Simulation result of the third LFSR in parallel design, input is the invert of "8th-14th" of the output of the first LFSR; (d) the final output of parallel design: XOR of the output of second and third LFSR.

Chapter 5 High Speed All Optical Logic Gates using Binary Phase Shift Keyed Signal based on QD-SOA

5.1 Introduction

In future high speed all-optical communications, logic gates will play important roles, such as signal regeneration, addressing, header recognition, data encoding and encryption [1]. In recent years, demonstrations of high speed all-optical logic gates using different schemes were reported, including dual semiconductor optical amplifier (SOA) Mach-Zehnder interferometer (MZI) [2, 3], semiconductor optical amplifier loop mirror (SLALOM) [4], ultrafast nonlinear interferometer (UNI) [5], four-wave mixing in SOA [6] and cross gain (XGM)/cross phase (XPM) modulation in nonlinear devices [7]. Among the above schemes, the SOA based MZI has the advantage of being relatively stable, simple and compact. The emergence of quantum-dot (QD) SOAs in recent years provided a better device for signal processing at communication band. Up till now, such devices has experimentally demonstrated high saturated output power and low noise figure [8, 9], ultrafast carrier relaxation between QD energy states [10, 11] and a much smaller carrier heating (CH) impact on gain and phase recovery [12]. In recent years, optical logic gates using OOK signals based on QD-SOA-MZI have been proved at data rates of ~ 250Gb/s [13]. However, the patterning effects and amplified spontaneous emission are very strong for the above schemes using OOK signal which will degrade the output quality.

Thus, in this chapter I proposed an alternative method of improving the output quality and

achieving high-speed all-optical logic operations. This method utilizes a QD-SOA-MZI pair each differentially driven by a data input and its complement. In addition, I presented a model of pseudo-random binary sequence (PRBS) generators based on optical logic XOR and AND gates. The simulation results on optical logic gates and PRBS generation show that this new system is capable of realizing generation at speed of ~250Gb/s with better output quality.

5.2. Operation Principles of all-optical logic gates and schematic of PRBS generation

The proposed scheme accomplishing all-optical XOR operations is shown in Figure 5.1. It consists of a pair of QD-SOA-MZIs. Each QD-SOA-MZI is differentially driven by data and complement. The arrangement in Figure 5.1, in contrast to the conventional single SOA-MZI XOR set up, ensures that each QD-SOA receives a nearly constant-power stream of input pulse train. This is also illustrated in Figure 5.1 using an example of an on-off-keyed (OOK) signal A=[101]. Hence the patterning effects can be mitigated that arise from the fluctuation in the signal optical powers when QD-SOAs are directly modulated by OOK signals without a differential set up. For instance, the most deleterious situation is avoided, where the QD-SOAs receive a long sequence of 1's followed by a long sequence of 0's, or vice versa. Furthermore, because binary phase shift keyed (BPSK) signals carry information on the phase part while keeping the amplitude as a constant, the impairments from optical nonlinear effects and amplified spontaneous emission are greatly reduced. The working principle as follows: the top QD-SOA-MZI converts the input OOK data streams A and its complement into BPSK signal, $\exp(j\pi A)$.The bottom QD-SOA-MZI similarly outputs a BPSK signal $\exp(j\pi B)$. The

conversion of OOK into BPSK was first used for all-optical wavelength conversion of DPSK signals [14] and its process is detailed in [14, 15]. The next step in XOR operation is the linear optical interference between these two BPSK signals. The interference yields two OOK signals, one is XOR logic and the other is NXOR logic. The intensity envelops of the output signals emerging from the constructive and destructive ports of the 2x2 coupler are calculated using:

$$\left|\exp(j\pi A)+\exp(j\pi B)\right|^2 \square \overline{A\oplus B} \tag{5.1}$$

$$\left|\exp(j\pi A)-\exp(j\pi B)\right|^2 \square A\oplus B \tag{5.2}$$

We can use a similar scheme to realize logic AND and NAND operations as shown in Figure 5.2. From Boolean algebra, we know $\overline{\mathrm{A}}$ XOR$\left(\overline{\mathrm{A}}+\mathrm{B}\right)$=A AND B. In this scheme, the top QD-SOA-MZI converts the input OOK data $\overline{\mathrm{A}}$ and its complement A into BPSK signal exp(j$\pi\overline{\mathrm{A}}$).The bottom QD-SOA-MZI similarly outputs a BPSK signal exp(jπ($\overline{\mathrm{A}}$+B)). Thus, one output after interference is $\overline{\mathrm{A}}$ XOR$\left(\overline{\mathrm{A}}+\mathrm{B}\right)$ which is the same as A AND B and the other output after interference is A NAND B. $\overline{\mathrm{A}}+\mathrm{B}$ is simply realized by an optical coupler.

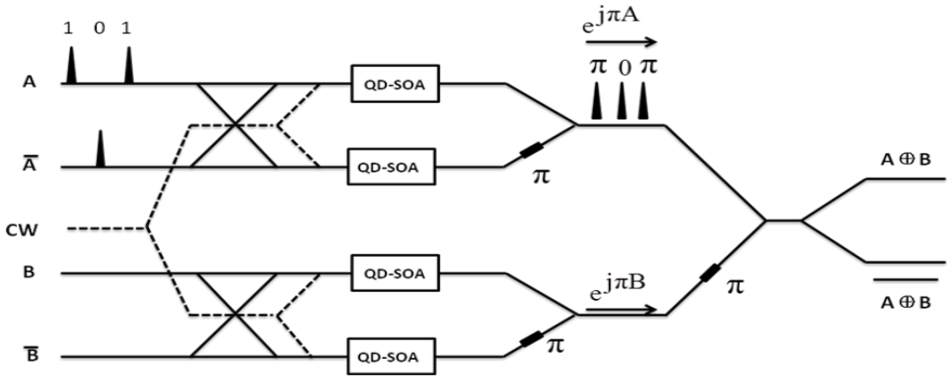

Figure 5.1: Schematic of the all-optical XOR logic gate, CW: continuous wave

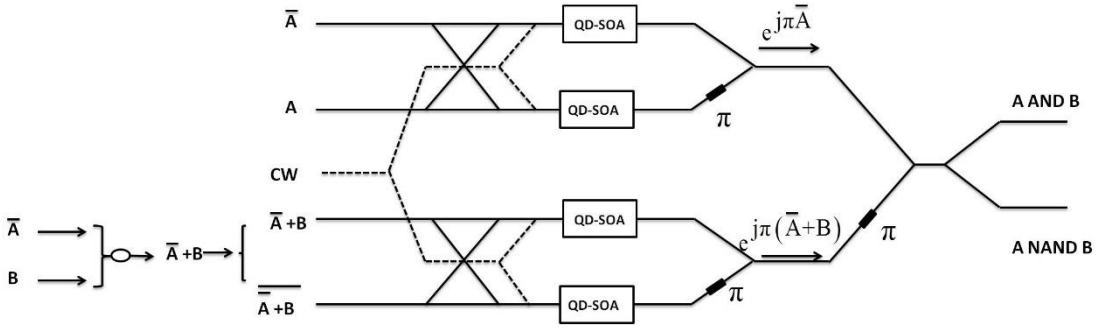

Figure 5.2: Schematic of the all-optical AND and NAND logic gates, CW: continuous wave

Similar to chapter 4, PRBS signals are generated by a linear feedback shift register (LFSR) composed of QD-SOA-based logic XOR and AND gates, shown in Figure 5.3. An LFSR has m data storing units (optical delay line in all-optical system), each unit is capable of storing one binary data bit for one clock period [16]. The whole system is synchronized with a clock. At each period, the n_{th} and m_{th} bit go through an XOR process. Their XOR result gets reshaped and its wavelength is converted back to system's operation wavelength through an AND gate, and then goes back to the front of LFSR. The output PRBS signals can be tapped from the end of the LFSR.

The XOR gate in LFSR is realized through our scheme in Figure 5.1. Because after the XOR gate the BPSK data change back to OOK data we can use a single QD-SOA-MZI scheme [13] to realize all-optical logic AND operation which is also the building block of our PRBS scheme. As shown in Figure 5.4, two identical QD-SOAs form the two arms of the interferometer. By putting data A to port 1 and data B to port 3, we can get gain modulated pattern of data B out of port 4 resembling logic A AND B. To make results better in quality, a low power CW light is used into port 2 to cancel out the background noise of data stream A.

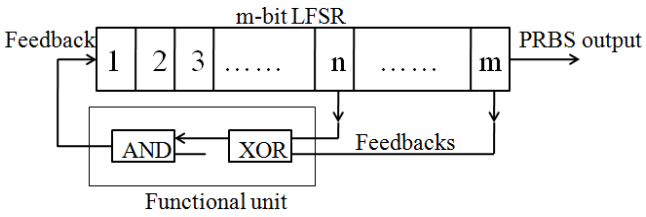

Figure 5.3: Design of PRBS generator: Block diagram of a LFSR

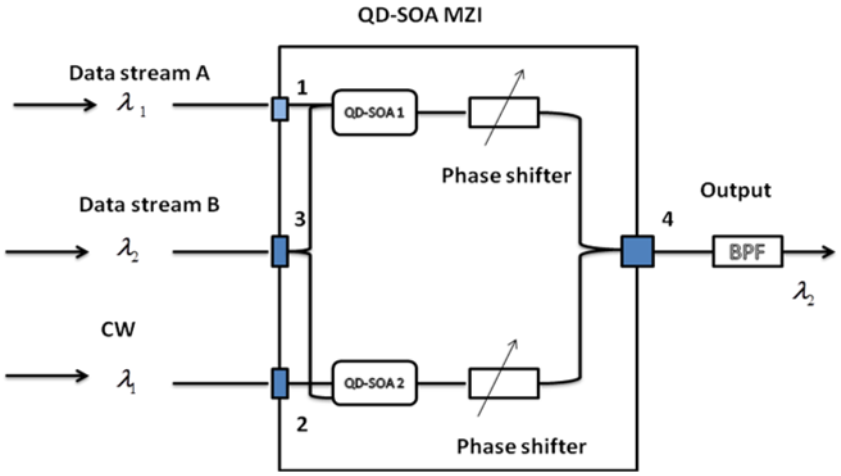

Figure 5.4: Schematic of one single QD-SOA Mach-Zehnder Interferometer to realize AND logic. BPF: bandpass filter centered at λ_2

5.4. QD-SOA rate equations and nonlinear effects

The device we chose here is InAs/GaAs QD-SOA, with InAs quantum dots embedded in GaAs layers [8, 17-20] which is the same as chapter 2 and 4. This type of device has a typical gain of ~15 dB gain around 1550nm band, with noise figure as low as 7 dB [8]. The device gain is nearly polarization-independent [20].

The carrier transitions between various states in the QD-SOA are described by the following rate equations [21-22]:

$$\frac{dw}{dt} = \frac{I}{eVN_{wm}} - \frac{w}{\tau_{wr}} - \frac{w}{\tau_{w-e}}(1-h) + \frac{N_{esm}}{N_{wm}}\frac{h}{\tau_{e-w}}(1-w) \tag{5.3}$$

$$\frac{dh}{dt} = -\frac{h}{\tau_{esr}} + \frac{N_{wm}}{N_{esm}}\frac{w}{\tau_{w-e}}(1-h) - \frac{h}{\tau_{e-w}}(1-w) + \frac{N_{gsm}}{N_{esm}}\frac{f}{\tau_{g-e}}(1-h) - \frac{h}{\tau_{e-g}}(1-f) \tag{5.4}$$

$$\frac{df}{dt} = -\frac{f}{\tau_{gsr}} - \frac{f}{\tau_{g-e}}(1-h) + \frac{N_{esm}}{N_{gsm}}\frac{h}{\tau_{e-g}}(1-f) - \frac{\Gamma_d}{A_d}a(2f-1)\frac{1}{N_{gsm}}\frac{S(t)}{\hbar\omega} \tag{5.5}$$

where w, h and f are the occupation probability of the wetting layer, the QD excited state and ground state, respectively; N_{wm}, N_{esm} and N_{gsm} are the maximum density of carriers in each state; τ_{ar} ("a" being "w," "es" or "gs") is the spontaneous radiation lifetime of each state; $\tau_{a\text{-}b}$ is the relaxation lifetime between any two states "a" and "b"; I is the injected bias current; Γ_d is the active layer confinement factor; V is the effective volume of the active layer; a is the differential gain; A_d is the effective cross-sectional area of the active layer and S(t) is the total input light power.

The gain of QD-SOA which results from carrier density dynamics, including nonlinear processes like carrier heating (CH) and spectral hole burning (SHB) effects [12，23], is expressed as:

$$g(t) = \frac{a(N - N_t)}{1 + (\varepsilon_{CH} + \varepsilon_{SHB})S(t)}$$

(5.6)

where N is the GS carrier density, N_t is the transparent GS carrier density; ε_{CH} and ε_{SHB} are the gain suppression factors for carrier heating and spectral hole burning effect, respectively.

The injected light and temperature change due to carrier heating also changes the refractive index of the active region, and thus a phase change to any probe wave injected.

$$\phi(t) = -\frac{1}{2}(\alpha G_l(t) + \alpha_{CH}\Delta G_{CH}(t)) \quad (5.7)$$

where $G_l(t)=e^{g(t)l}$ is the linear gain factor of the device with l being the effective length of the active layer, α and α_{CH} are the linewidth enhancement factors of the device corresponding to band-to-band transition and carrier heating process, respectively [24, 25]. The linewidth enhancement factor due to spectral hole burning (SHB) is ~0.

5.5. Simulation results

Parameters chosen for simulation in this chapter are experimental results on QD-SOAs for central wavelength: 1.55μm: $\tau_{wr}=\tau_{esr}=200$ps, $\tau_{gsr}=50$ps, $\tau_{w\text{-}e}=3$ps, $\tau_{e\text{-}w}=300$ps, $\tau_{g\text{-}e}=10$ps, $\Gamma_d=10\%$, linewidth enhancement factors $\alpha=4$, $\alpha_{CH}=0.2$ [24,25], QD energy levels' densities of states, $n_w=5.4\times10^{17}$cm^{-3}, $n_w:n_e:n_g\approx15:2:1$ [22], QD areal density is 7.5×10^{10}cm^{-2}, saturated output power is 18dBm at 1.55μm wavelength [8], device differential gain $a=8.6\times10^{-15}$cm^2 [19], effective length l=1.0mm, noise figure F=7dB [8], transparency pump current density is ~0.2kA/cm^2 [12], gain suppression factors are $\varepsilon_{CH}=0.5\times10^{-23}$m^3, $\varepsilon_{SHB}=7.5\times10^{-23}$m^3 [26], which

correspond to threshold input pulse energy for both nonlinear effects ~0.47pJ. Value of time constant $\tau_{e\text{-}g}$ has been measured in many experiments, the smallest report value is ~0.1ps [12] and the largest measured value goes up to several picoseconds [18]. We have not taken into account the inhomogeneous broadening associated with different dot sizes. But it is indirectly taken into account in the form of spectral hole burning. In a QD the inhomogeneously broadened spectrum range could be small because it requires carrier transport among QDs: a QD has discrete transition wavelengths and carrier relaxation to another wavelength involves transition to another QD [23]. Simulated results of all-optical XOR, AND and NAND logic gates using our schemes in Figure 5.1 and Figure 5.2 are shown in Figure 5.6, Figure 5.7 and Figure 5.8. The output eye-diagrams are also plotted to show the output quality. From the simulated results, we show that all-optical XOR, AND and NAND logic gates using BPSK signal, scheme of a pair of QD-SOA-MZIs, @ ~ 250 Gb/s are feasible.

A simulated high speed all-optical 7-bit PRBS output at operation speed 250Gb/s is shown in Figure 5.9(a), its eye diagram is also plotted in Figure 5.9(b). Meantime, the high speed all-optical 7-bit PRBS output using OOK signal based on QD-SOA (the XOR gate is realized by using one QD-SOA-MZI) and its eye diagram are also shown in Figure 5.10 [27]. From the two eye diagrams in Figure 5.9 and Figure 5.10, we can see the eye diagram in Figure 5.9 shows a much clearer open eye than that in Figure 5.10 illustrating better output quality and the stability of the scheme using BPSK signal based on QD-SOA.

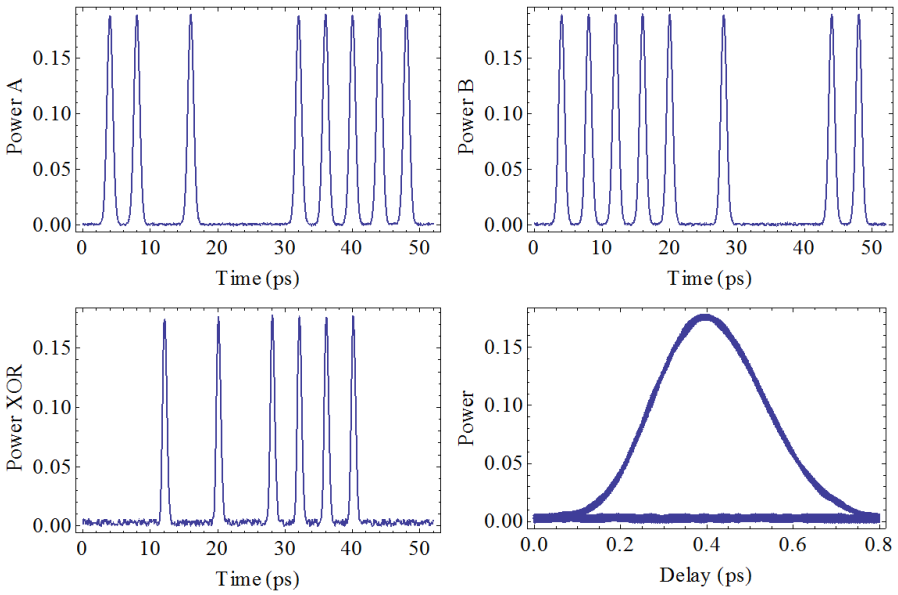

Figure 5.6: Date A and Date B are shown on the top. Simulated results of output (XOR) and eye diagram of the output are shown below. The above set of figures is for 250Gb/s data rate.

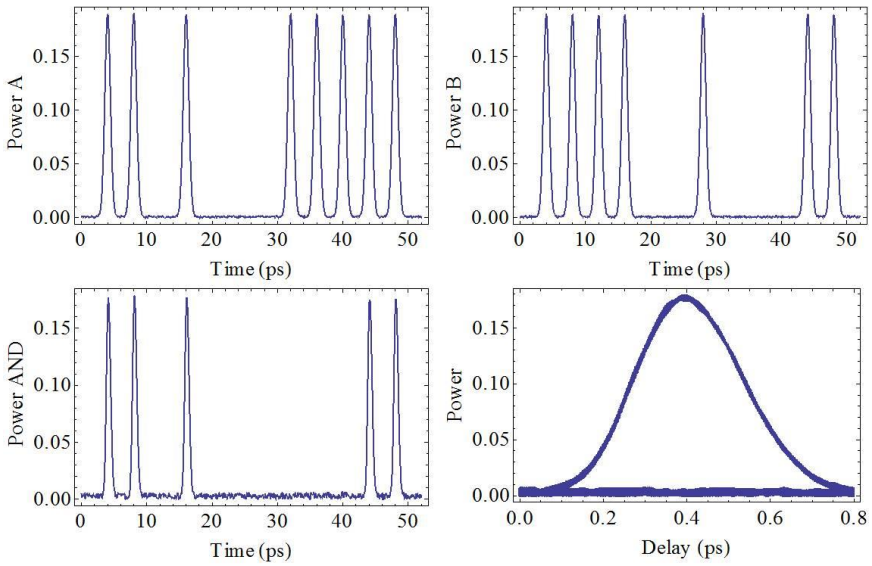

Figure 5.7: Date A and Date B are shown on the top. Simulated results of output (AND) and eye diagram of the output are shown below. The above set of figures is for 250Gb/s data rate.

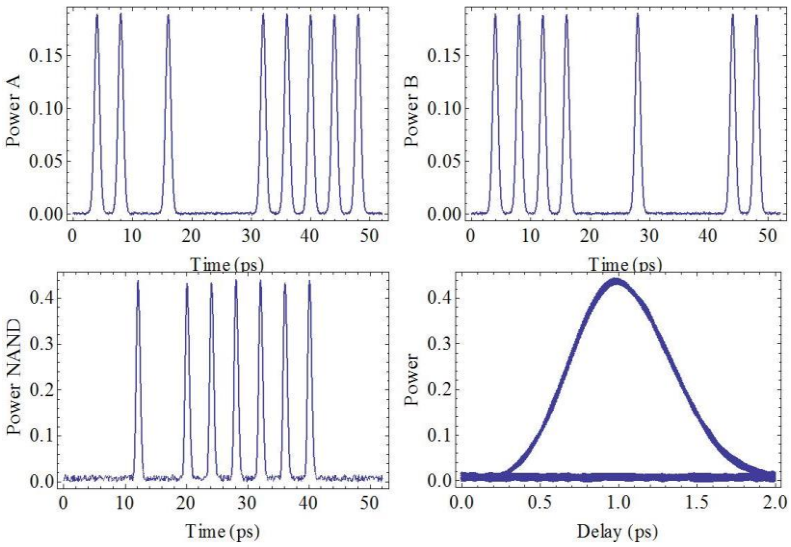

Figure 5.8: Date A and Date B are shown on the top. Simulated results of output (NAND) and eye diagram of the output are shown below. The above set of figures is for 250Gb/s data rate.

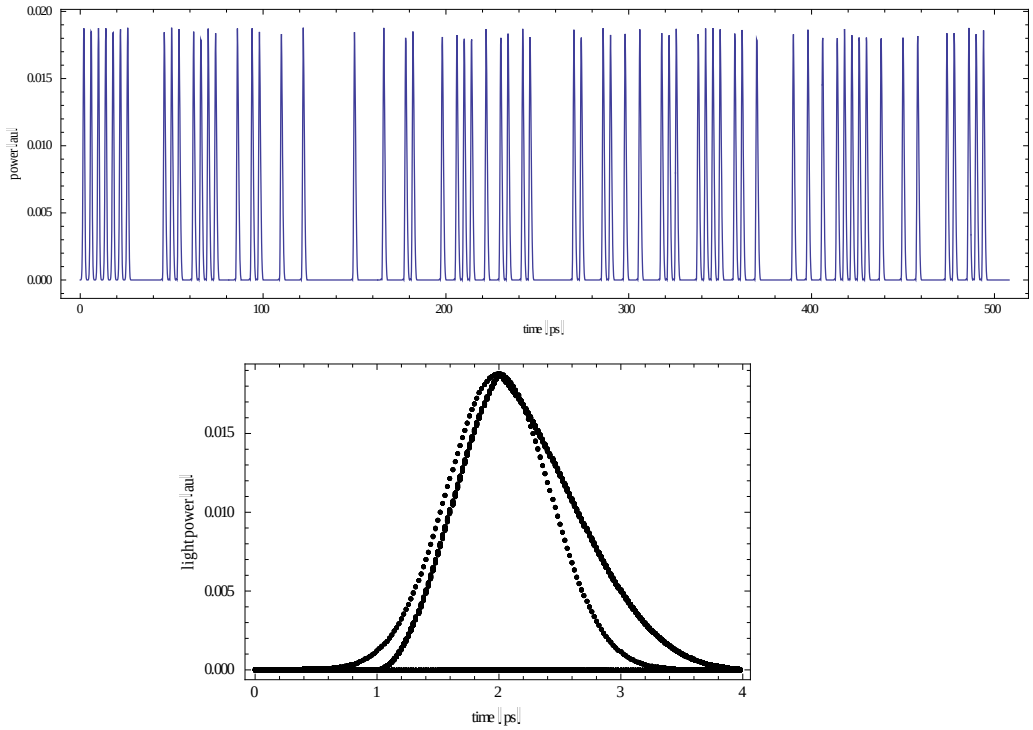

Figure 5.9 (a) Simulation result of PRBS sequence using BPSK scheme, operating at 250 Gb/s; (b) The eye diagram of this result.

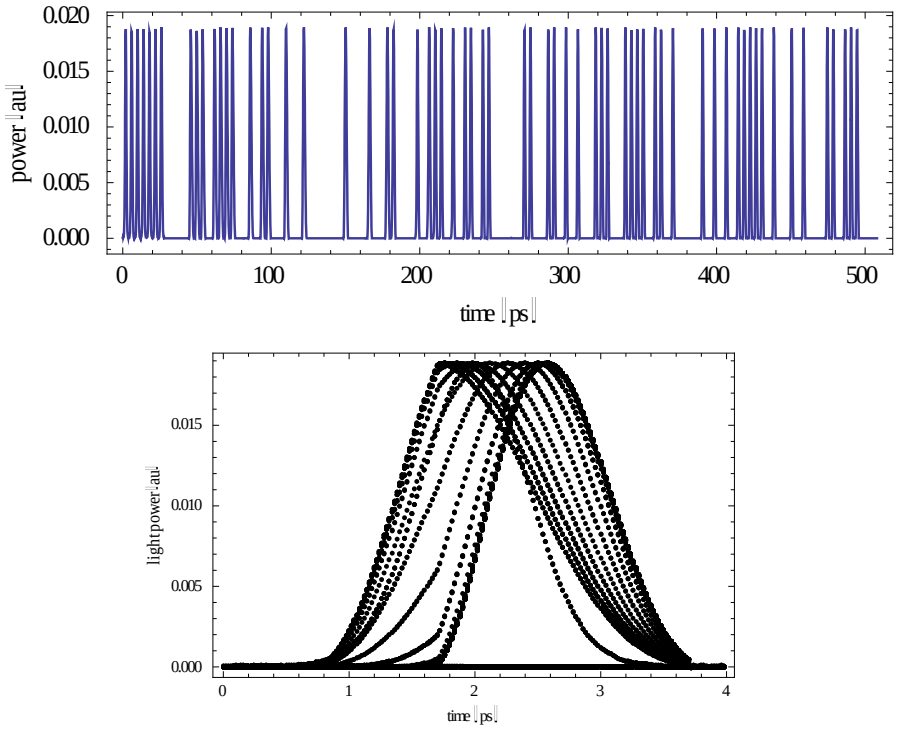

Figure 5.10 (a) Simulation result of PRBS using OOK scheme based on QD-SOA, operating at 250 Gb/s; (b) The eye diagram of this result.

5.6 Conclusion

In this chapter I proposed and simulated a scheme to realize high speed all-optical logic gates and pseudo random bit sequence (PRBS) using binary phase shift keyed (BPSK) signal based on quantum-dot semiconductor optical amplifiers (QD-SOA). The PRBS is generated using a linear feedback shift register (LFSR) composed of all-optical logic XOR and AND gates. The optical logic gate is composed of a pair of QD-SOA Mach-Zehnder interferometers, which can generate BSPK signal to realize optical logic XOR, AND and NAND gates. Results show that this kind of scheme can perform logic operations such as XOR, AND, NAND and PRBS at high bit rate up to 250Gb/s with better output quality comparing with the system using OOK signal.

Chapter 6 High Speed Ultrashort Pulse Fiber Ring Laser Using Charcoal Nano-particles

6.1 Introduction

The generation of stable high speed ultrashort pulses is very important for fiber-optic telecommunication system. Future transmission systems may operate at data rate 250Gb/s or more [1]. Thus, the stability of the optical pulse train from a fiber laser needs to be improved for practical system use. The instability of fiber laser generally originates from three main factors: 1) polarization fluctuations in the long fiber cavity due to mechanical vibrations; 2) cavity length drift due to fluctuations of the temperature; 3) independent supermodes, whose frequencies could be any integral multiples of the cavity fundamental frequency f_c. Several researchers have carried out experiments to overcome the instability problems. Takara *et al* constructed fiber lasers with an all-polarization-maintaining ring cavity [2]. Shan *et al* developed a pulsed phase-lock method to compensate for the drift of the long fiber cavity length [3]. Wu *et al* proposed a scheme using a semiconductor optical amplifier (SOA) in the ring cavity to improve the stability of the fiber laser by removing the supermode noise [4]. Meanwhile, during the past two decades, a variety of schemes of pulse compression have been proposed and demonstrated. These schemes include (1) adiabatic soliton compression techniques [5-6], (2) multiple-step compression based on self phase modulation in highly nonlinear fibers or semiconductor optical amplifiers (SOA) [7-8], (3) a comb-like profiled fiber (CPF) to emulate dispersion decreasing fiber [9-10], (4) saturable optical absorbers such as nonlinear optical loop mirror (NOLM) or nonlinear amplifying loop mirror (NALM)

[11-13]. The saturable optical absorber is a promising method to compress the optical pulse width and can be adapted to various possible configurations.

Since the first demonstration of graphene saturable absorber for passively mode-locked erbium-doped fiber lasers (EDFLs), versatile graphene samples in different forms have been developed, including single-layer graphene [14], few-layer graphene [15], multi-layer graphene [16], graphene polymer [17], graphene composite [18], graphene solution [19] and graphite nan-particle [20] etc., which progressively show the capabilities on initiating the ultrafast saturable absorption in the EDFL cavity. Up to now, almost all graphene, graphene oxide and graphite materials can be used as optical saturable absorbers which have ultrafast recovery time, ultrahigh nonlinearity and large optical damage threshold. Recently, Singh *et al* demonstrated a green and simple method to synthesis the graphene nano-sheets from a pencil using the electrochemical exfoliation [21]. The bulk charcoal structure in a pencil is confirmed to be similar with graphite that contains multi-layer graphene. In the meantime, Lin's group also obtained the charcoal nano-particles by simply polishing the pencil [22], and presented that even the unprocessed charcoal nano-particles possess the ability of saturable absorption.

In this chapter, a fiber ring laser system with charcoal nano-particles in the cavity is proposed and experimentally studied. The charcoal nano-particles are made through mechanical polishing from pencil and then directly brushed onto the end-face of single-mode fiber (SMF) patchcord connector. This fiber ring laser system is composed of a Mach-Zehnder type

modulate, an EDFA as the gain medium, an isolator and a polarization controller (PC). Results show that with the charcoal nano-particles inside the ring cavity, this fiber ring laser system can generate optical pulse train @ 20Gb/s with improved stability and smaller pulse width comparing with the system without the particles in the cavity.

6.2 Experiment Setup

We directly brushed the triturated charcoal nano-particles which are mechanically polished from the pencil onto the end-face of single-mode fiber (SMF) patchcord connector to be the saturable absorber for the fiber ring laser system. However, the self-aggregation of charcoal nano-particles would enlarge its size to increase the absorption loss [22]. Thus, we utilized the imprinting-exfoliation-wiping method [20] to reduce the size of charcoal nano-particle and its coverage ratio on the SMF end-face. Figure 6.1 shows the fabricating process for thinning and separating the charcoal nano-particles by utilizing the imprinting-exfoliation-wiping method. The photograph of the pencil, the triturated charcoal powder and the SMF patchcord are shown in Figure 6.1(a). The optical microscope (OM) image of the adhesion of charcoal nano-particles on the SMF connector end-face after direct brushing is shown in Figure 6.1(b). Then, the SMF patchcord with charcoal nano-particles is tightly connected with another SMF patchcord which is shown in Figure 6.1(c). After separating the connected SMF patchcords, the charcoal nano-particles can be exfoliated again to shrink their size. This method can reduce the layer number of the graphene inside the charcoal nano-particle, as illustrated in Figure 6.1(d). By repeating the imprinting-exfoliation-wiping process several times, the OM

image in Figure 6.1(e) shows the reduced coverage ratio of charcoal nano-particles on SMF connector end-face.

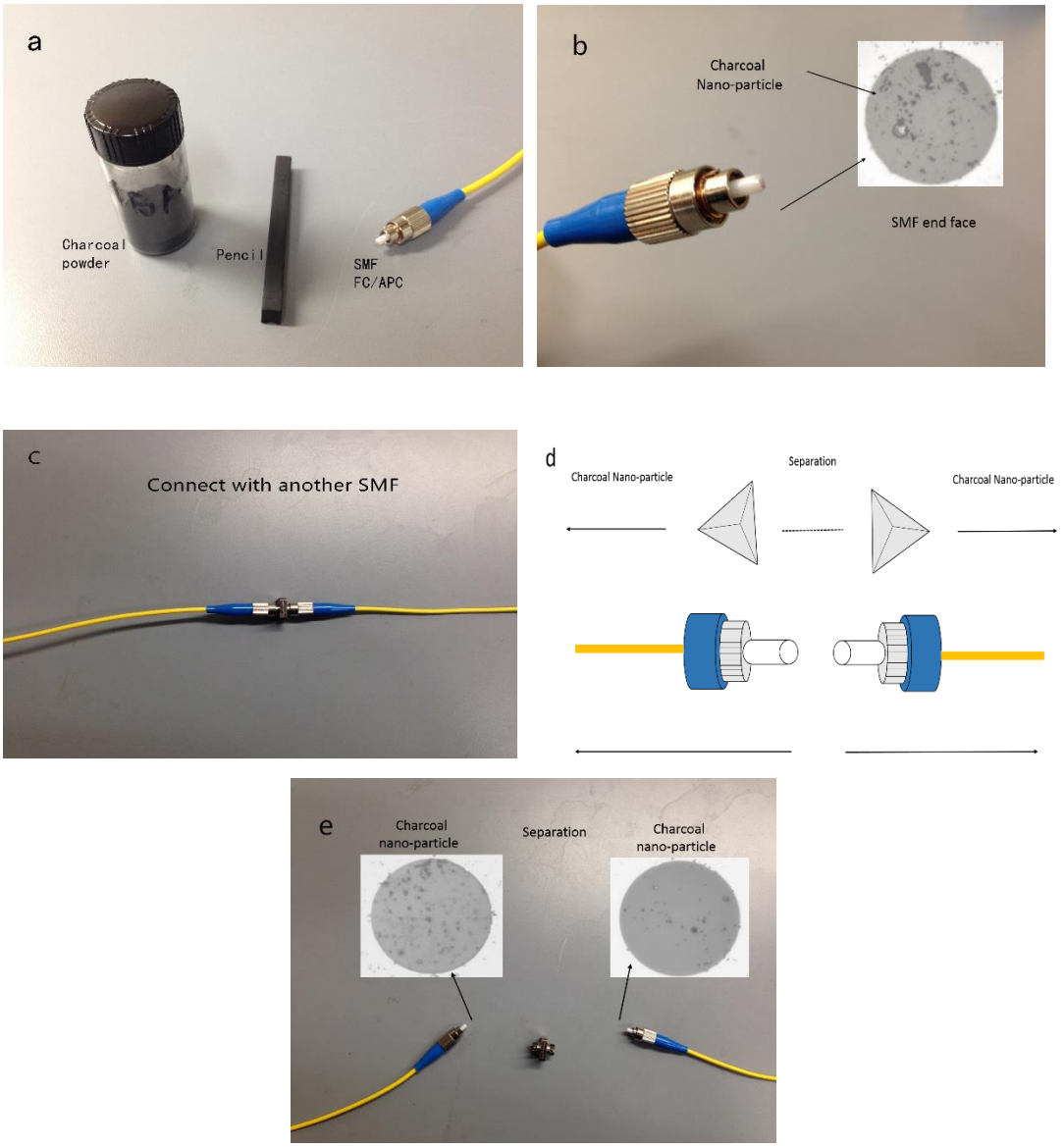

Figure 6.1: The imprinting-exfoliation-wiping process for adhesion of charcoal nano-particles onto the end-face of SMF patchcord. (a) The photograph of pencil, charcoal powder and SMF. (b) OM image of charcoal nano-particles directly brushed on SMF end-face. (c) Connect with another SMF. (d) Separation of SMF connectors. (e) The OM images of charcoal nano-particles on both SMF end faces after repeating the imprint-exfoliation-wiping process

several times.

The experiment setup of fiber ring laser system is shown in Figure 6.2. The system consists of a 23m long Er-doped fiber, a WDM coupler, a 980nm laser diode, a 10% output coupler, an islotar, a polarization controller, a Mach-Zehnder type modulator and a systhesizer. All components were connected by regular single-mode fiber. We use a 980nm laser diode to pump the EDF and a 980/1550 wavelength division multiplexer (WDM) is involved to deliver the pumping power. The isolator is placed in the ring system to decide circulation direction and avoid feedback. The PC is insertd in the system to control the intra-cavity polariztion. The synthesizer is used to generate the RF signal to drive the Mach-Zehnder type modulator which has a bandwidth of 11GHz. The charcoal nano-particles are confined betweeen two SMF patchcord connectors side the ring cavity. The output optical coupler provides 90% feedback ratio and 10% output coupling ratio.

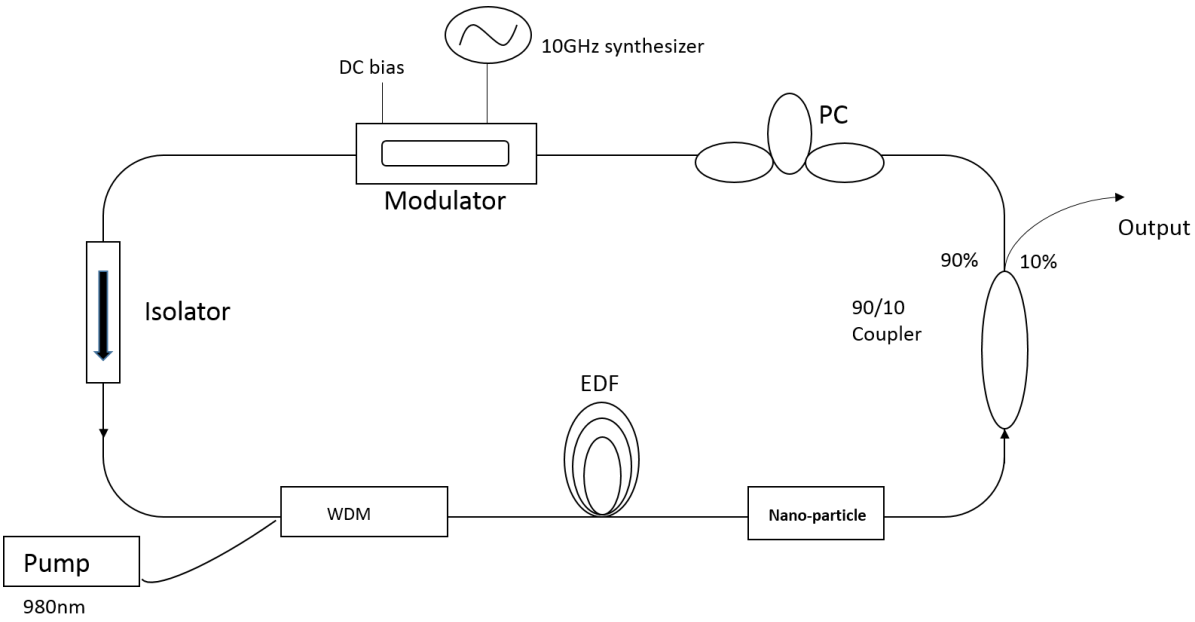

Figure 6.2: The schematic diagram of the fiber ring laser system with charcoal nano-particles inside the cavity. WDM: wavelength-division multiplexer, PC: polariztion controller.

6.3 Harmonic and rational harmonic mode locking

We can use the experiment set-up in Figure 6.2 to realize harmonic mode locking and rational harmonic mode locking. To analyze the fiber ring laser, we assume the ring cavity has a length L, then the fundamental cavity frequency is $f_c=c/(Ln_{eff})$, where c is the velocity of light in vacuum and n_{eff} is the effective refractive index of the cavity. A modulation signal with frequency f_m is applied to the modulator to modulate the loss in the cavity. For harmonic mode-locking, $f_m=nf_c$, where n is an integer. For a typical fiber ring laser, $f_c \sim$ 1 to 3 MHz and $f_m \sim$ 1 to 10GHz so about 10^6 cavity modes are present within the gain spectrum, which allows harmonic mode locking. Although the modulator couples every ~1000th mode, the gain spectrum is broad enough that coupling of ~10^5 to 10^6 cavity modes can occur. Considering the loss and gain in the fiber ring laser and using the Fourier analysis method, we can get the expression for the envelope of mode-locked pulse [23]:

$$a(\omega) = A\exp\left(\frac{-\omega^2\tau^2}{2}\right) \tag{6.1}$$

$$a(\mathrm{t}) = \frac{\sqrt{2\pi}}{\tau}A\exp\left(\frac{-t^2}{2\tau^2}\right) \qquad \tau = \left(\frac{2g}{M}\right)^{1/4}\left(\frac{1}{\omega_m\Omega_g}\right)^{1/2} \tag{6.2}$$

where g is the gain at the center frequency, M is the modulation depth, Ω_g is the gain bandwidth and $\omega_m=2\pi f_m$. Thus, for harmonic mode-locking case $f_m=nf_c$, the solution is a Gaussian pulse, where the pulse width is proportional to $f_m^{-1/2}$. Furthermore, we can obtain smaller pulse width by increasing the modulation frequency and modulation power while reducing the pump power for the cavity of the fiber ring laser.

The phenomena of rational harmonic mode locking with a repetition rate of $(np+1)f_c$ can be

realized when the modulation frequency $f_m=(n+1/p)f_c$, where n and p are integers. Following a similar analysis of harmonic mode-locking, we can conclude that the solution for harmonic mode-locking is also a Gaussian pulse given by equation (6.2) and the pulse width τ is expressed as [23]:

$$\tau = \left(\frac{2g}{M}\right)^{1/4} \left(\frac{1}{(n+\frac{1}{p})\omega_m \Omega_g}\right)^{1/2} \tag{6.3}$$

where $\omega_m=2\pi f_m$. From the above equation, we can see the pulse width parameter τ is proportional to $(n+1/p)^{-1/2}$. Since n is much larger than 1 for the modulation frequencies we often use, it is possible to conclude that the pulse width for rational harmonic mode-locking is almost same as that for harmonic mode locking.

6.4 Characterization of charcoal nano-particles

The size of the charcoal nano-particles after trituration is reduced down to 500nm [24], which further shrinks to 300nm after the exfoliation-imprinting-wiping process, as shown in Figure 6.3 (a). The XRD analysis of charcoal nano-particle shown in Figure 6.3(b) reveals a peak at 26.77^0 from the {002}-oriented lattice in comparison with the {002} peak of nature graphite (26.54^0), indicating the main composition and structure of charcoal nano-particles are similar with graphite. However, the small angel shift of $0.23^0$and the satellite peaks on the XRD graph elucidate the existence of impurities and structural defects including curvatures and distortions of graphene layers [25].

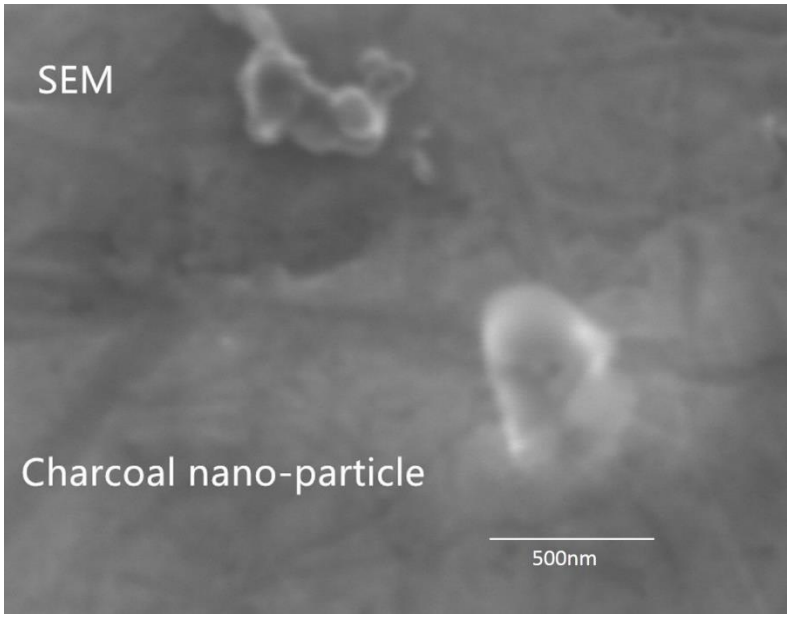

Figure 6.3 (a): The SEM image of charcoal nano-particles.

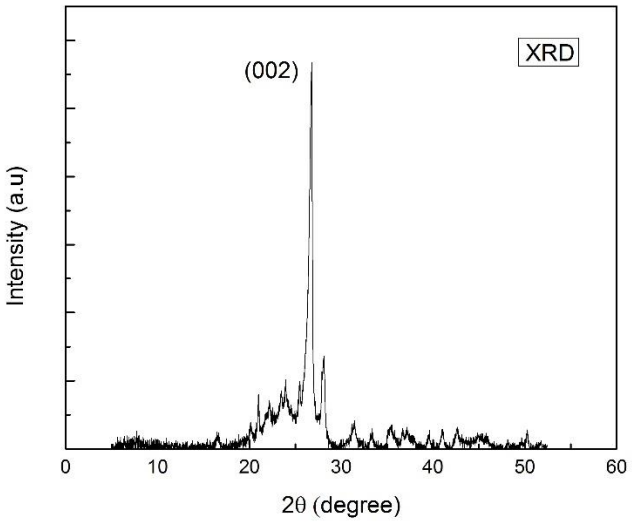

Figure 6.3 (b): XRD spectrum of charcoal nano-particles.

The saturable absorbance of charcoal nano-particle is characterized by fiber ring laser illumination. The optical absorption of charcoal nano-particle is reduced under high optical power illumination because the carrier transition from valence band to conduction band is forbidden by the Pauli blocking effect [24]. The optical absorbance α of charcoal

nano-particle is correlated with the linear absorbance (q_{lin}), the nonlinear absorbance (q_{non}), as described by [14]:

$$\alpha = q_{lin} + \frac{q_{non}}{1 + P_{in} / P_{sat}} \approx q_{lin} + q_{non} - \frac{q_{non}}{P_{sat}} P_{in} \tag{6.4}$$

where P_{in} denotes the input power, P_{sat} the saturation power of charcoal nano-particle. The normalized saturable absorbance of charcoal nano-particles is shown in Figure 6.4 (a) with a modulation depth of 36%. Fitting this curve obtains the linear loss of q_{lin}=0.37, the nonlinear loss of q_{non}=0.48, and the saturation power of P_{sat}=3.2mW which is a relatively low power for initiating the saturable absorption. The saturable transmittance is also shown in Figure 6.4 (b), with transmittance from 0.21 to 0.58 when increasing the input power from 0.5mW to 35mW.

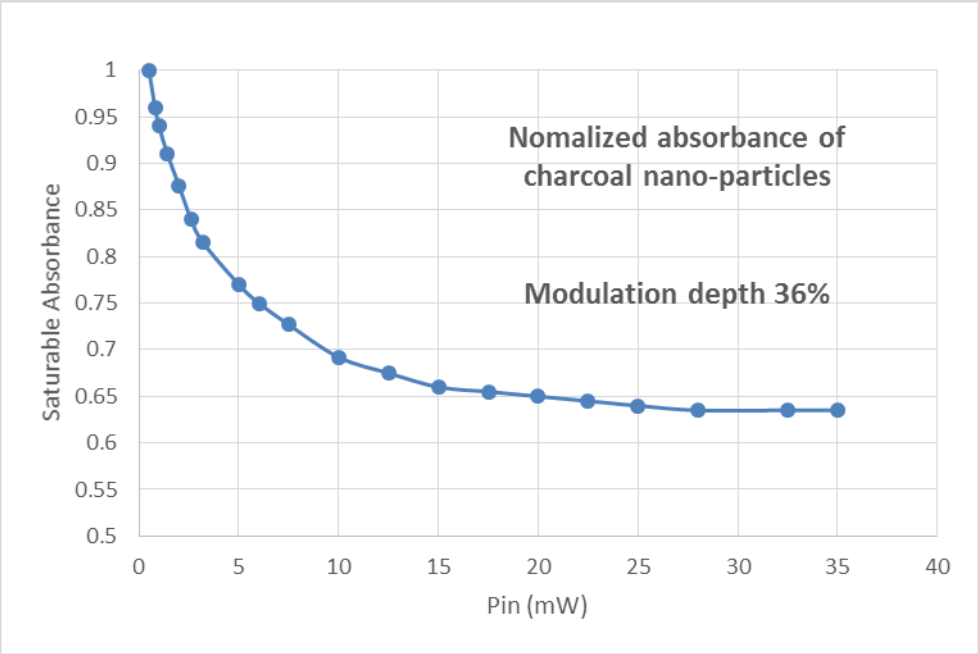

(a)

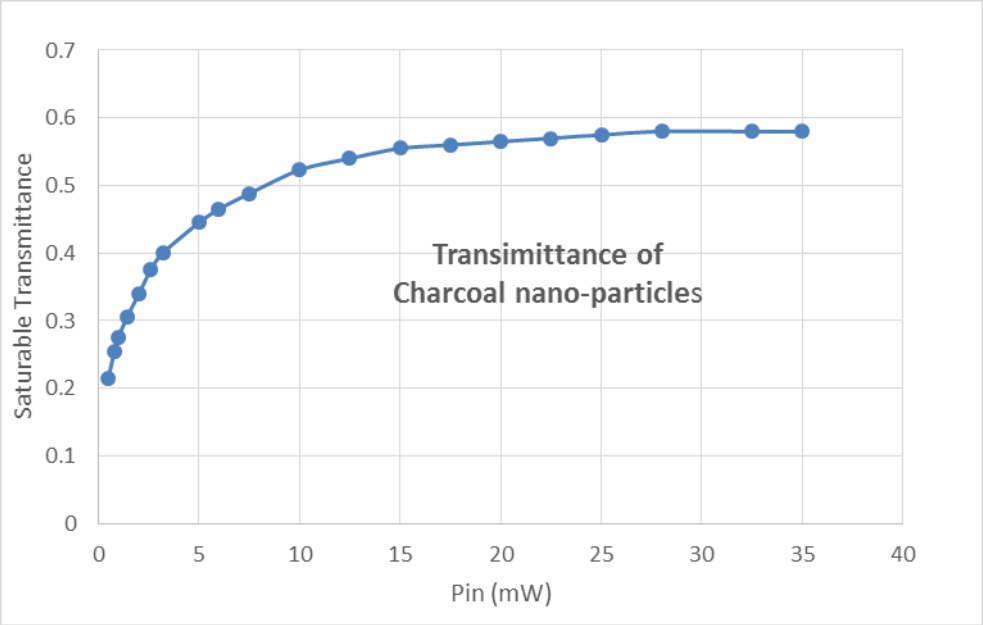

(b)

Figure 6.4: Saturable absorbance (a) and Transmittance (b) of charcoal nano-particle

6.5 Numerical Simulation

The mode locked pulse evolution of the fiber ring laser cavity in Figure 6.2 can be simulated by solving equations from 6.6 to 6.9. Equation 6.6 [26] is an extended nonlinear Schrödinger equation which was used to model the gain medium, EDF in Figure 6.2, of the fiber ring laser. In equation 6.6, A(z, T) is the slowing varying amplitude of the pulse envelope, β_2 and β_3 are the second and third order dispersion parameters, respectively. γ represents χ^3 nonlinearity parameter, and Ω_g is the gain bandwidth of the EDF. g is the gain of the EDF, which can be modeled by

$$g = g_0 / \left(1 + E / E_{sat-gain}\right) \tag{6.5}$$

where g_0 is the small signal gain, E is the energy of the pulse envelop. $E_{sat\text{-}gain}$ represents the gain saturation energy of the EDF. We used split-step Fourier method [27] to solve the equation (6.6) to simulate the pulse transmission in EDF. The values for β_2, β_3, γ and g_0 for EDF used in this numerical simulation are: -0.13×10^{-3} ps^2/m, 0.135×10^{-3} ps^3/m, $3.69W^{-1}km^{-1}$ and 2dB/m. We can also simulate the pulse evolution in single mode fiber (SMF) which composes the ring laser cavity by solving equation 6.6 if we set the gain parameter g as 0. . The values for β_2, β_3, γ and g_0 for SMF used in this numerical simulation are: -22.1×10^{-3} ps^2/m, 0.171×10^{-3} ps^3/m, $1.2W^{-1}km^{-1}$ and 0. The saturable absorption property of the charcoal nano-particles incorporated into the cavity was modeled by equation 6.7, where q_{lin} is 0.37, q_{non} is 0.38 and P_{sat} is 3.2mW which were obtained in section 6.4. We use a 90/10 coupler in our fiber ring laser system as in Figure 6.2, which can be simulated by solving equation 6.8 where R equals to 90%. The Lithium Niobate modulator can be simulated by solving equation 6.9 [28], where V_π is the required voltage for a π phase shift between two arms of the

modulator, V(t) is the voltage applied to the modulator. In our situation, the modulator is driven by a RF signal at frequency f_m. Thus, $V(t)=V_b+V_m\sin(\omega_m t)$ in which V_b is the DC voltage bias of the modulator, V_m is the amplitude of the RF signal. The numerical simulation was initiated by launching into the system a seed pulse with small amplitude. The pulse evolution within the ring cavity is then iteratively modeled until a steady state is reached after many roundtrips.

$$\frac{\partial A(z,T)}{\partial z}+\frac{i}{2}\beta_2\frac{\partial^2 A(z,T)}{\partial T^2}-\frac{1}{6}\beta_3\frac{\partial^2 A(z,T)}{\partial T^2}= \\ \frac{g}{2}A(z,T)+\frac{g}{2}\frac{1}{\Omega_g^2}\frac{\partial^2 A(z,T)}{\partial T^2}+i\gamma\left|A(z,T)\right|^2 A(z,T) \tag{6.6}$$

$$A(z.T)_{out}=A_{in}(z,T)\square T=A_{in}(z,T)(1-q_{lin}-\frac{q_{non}}{1+\frac{\left|A(z,T)\right|^2}{P_{sat}}}) \tag{6.7}$$

$$A(z,T)_{out}=R\square A_{in}(z,T) \tag{6.8}$$

$$A(z,T)_{out}=\cos\left(\frac{\phi(t)}{2}\right)A_{in}(z,\mathrm{T}) \quad \text{with} \quad \phi(t)=\pi\frac{V(t)}{V_\pi} \tag{6.9}$$

Figure 6.5 and Figure 6.7(a), (c) depict the simulated pulse development and the steady-state solutions of the output pulses, respectively. The FWHM is 5.4ps when operated without charcoal nano-particles, and narrowed to 3.1ps by using the charcoal nano-particles inside the cavity. It should be mentioned that the asymptotic state is independent on the seed pulse. Pulses having the same characteristics can be obtained as well when pumped with white noise in the simulation.

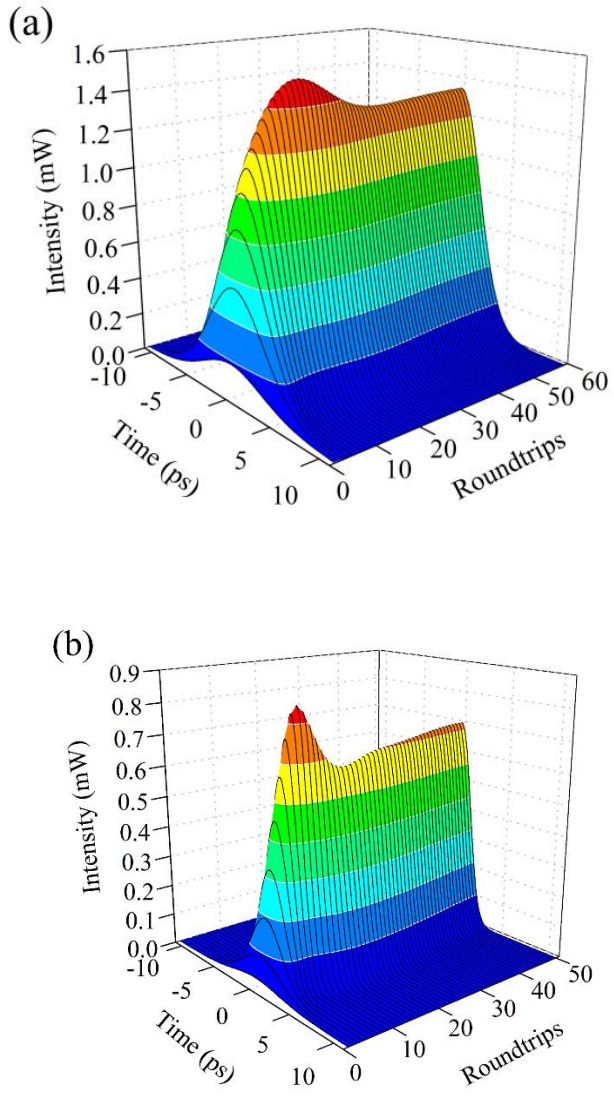

Figure 6.5. Simulated pulse generation from fiber lasers implementing (a) only rational harmonic active mode-locking and (b) with charcoal nano-paricles inside the ring cavity

6.6 Effects of charcoal nano-particles

Figure 6.6 shows the RF spectrum of the output pulse from the rational harmonic mode locking fiber ring laser with (b) or without (a) charcoal nano-particles in the cavity. Many side-bands are observed in Figure 6.6(a). The highest peak corresponds to the frequency of the fiber ring laser which is 20GHz. The separation between these sidebands is equal to the fundamental cavity frequency of the fiber ring laser f_c=2.8MHz so they are assumed to be the supermodes of the fiber ring laser. These supermodes cannot be removed by tuning the modulation frequency f_m and polarization controller in the cavity. However, no supermodes were observed in Figure 6.6(b) with the charcoal nano-particles inside the fiber ring laser cavity. The reduction of the supermodes in the RF spectrum can improve the stability of optical pulse generation in rational harmonic mode locking [4]. The reduced amplitude of the supermodes in the fiber ring laser is the result of the saturable absorption character of the charcoal nano-particles in the cavity.

Figure 6.7 (b) shows the experimental fiber ring laser pulse shape, autocorrelation pulse with pulse width ~ 5.6ps, without charcoal nano-particles inside the ring. This result is in good agreement with our numerical simulation result, which is shown in Figure 6.6(a). The charcoal nano-particles inside the cavity can greatly improve the pulse shortening mechanism of the fiber ring laser due to their saturable absorption character. Figure 6.6 (d) shows the experimental autocorrelation pulse with charcoal nano-particles inside the ring with pulse width ~3.2ps, about 57% of the pulse width without charcoal nano-particles in the ring cavity. This experimental result is also in good agreement with our numerical simulation result,

which is shown in Figure 6.6(c). Thus, with the charcoal nano-particles inside the ring, shorter pulses can be generated with improved stability.

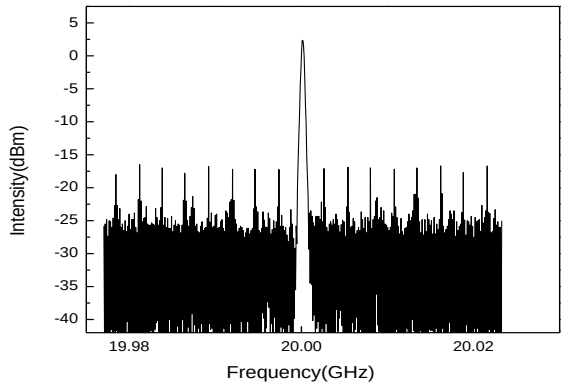

(a)

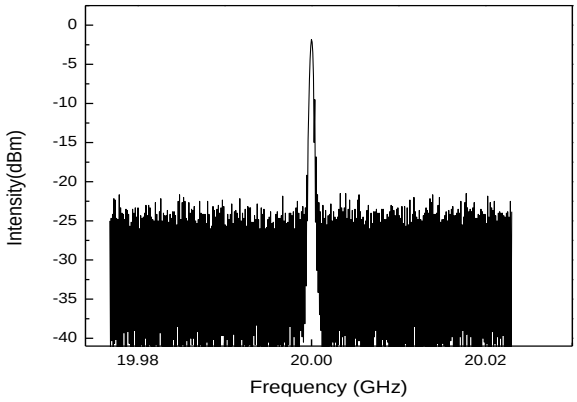

(b)

Figure 6.6: RF spectrum of rational harmonic mode locking at 20Gb/s. (a) without the charcoal nano-particles in the fiber ring laser cavity and (b) with the charcoal nano-particles in the fiber ring laser cavity.

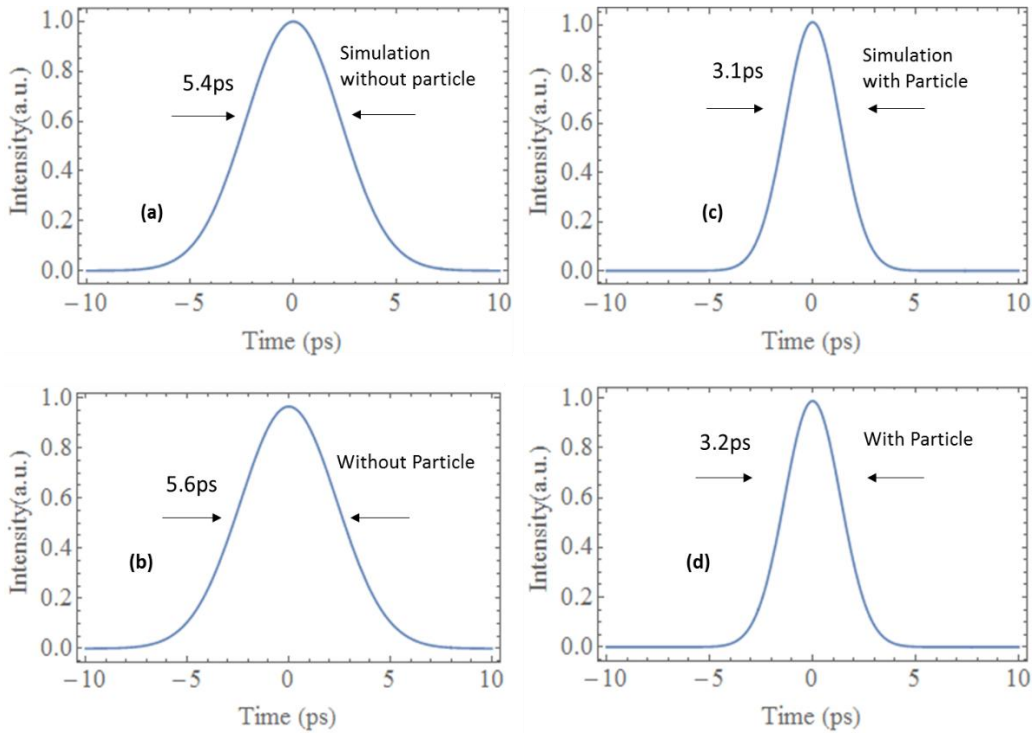

Figure 6.7: Pulse shape of the fiber ring laser. (a) Simulated pulse shape without nano-particles in the ring, pulse width ~ 5.4ps. (b) Autocorrelation pulse without nano-particles inside the ring, pulse width ~ 5.6ps. (c) Simulated pulse shape with nano-particles in the ring, pulse width ~ 3.1ps. (d) Autocorrelation pulse with nano-particles inside the ring, pulse width ~ 3.2ps.

6.7 Conclusion

In summary, we have successfully demonstrated a scheme to improve the stability and shorten the pulse width of a mode-locked fiber ring laser. The scheme uses charcoal nano-particles which are made through mechanical polishing from pencil as saturable absorbers inside the mode-locked fiber ring laser cavity. The size, composition and saturable absorbance of charcoal nano-particles are investigated in this chapter. Theoretical simulation results are also shown in good agreement with our experimental results. Using this scheme, we can remove the supermodes in the RF spectrum and shorten the pulse width to 3.2ps with compression ratio about 57%.

Appendix A Presentation and Publication

A.1 Conference Presentation and Proceedings:

1. **W. Li**, H. Hu, and N. K. Dutta, "Optical Latches using Optical Amplifiers," SPIE Defense, Security and Sensing, Baltimore, Maryland, April 2013

2. H. Hu, **W. Li**, and N. K. Dutta, "Wide-band Coherent Supercontinuum generation," SPIE Defense, Security and Sensing, Baltimore, Maryland, April 2013

3. **W. Li**, H. Hu, and N. K. Dutta "High Speed All-optical PRBS Generation using Binary Phase Shifted Keyed Signal based on QD-SOA," SPIE Optical Engineering and Application, San Diego, August 2014

4. H. Hu, **W. Li**, and N. K. Dutta, "Supercontinuum Generation in a Tapered Rib Waveguide," SPIE Optical Engineering and Application, San Diego, August 2014

5. H. Hu, **W. Li**, X. Zhang and N. K. Dutta, "Hybrid Mode-Locked Fiber Ring Laser Using Graphene and Charcoal Nanoparticles as Saturable Absorbers," SPIE Defense, Security and Sensing, Baltimore, Maryland, April 2015

6. X. Zhang, H. Hu, **W. Li**, and N. K. Dutta, "Supercontinuum generation in dispersion-varying microstructured optical fibers," SPIE Defense, Security and Sensing, Baltimore, Maryland, April 2015

A.2 Journal Publications:

1. S. Ma, **W. Li**, H. Hu, and N. K. Dutta, "High speed ultrashort-pulse fiber ring laser using photonic crystal fiber nonlinear optical loop mirror," Opt. Commun., 285 (12), 2832-2835 (2012)

2. **W. Li**, S. Ma, H. Hu, and N. K. Dutta, "All optical latches using quantum-dot semiconductor optical amplifier", Opt Commun., 285 (24), 5138-5143 (2012)

3. **W. Li**, S. Ma, H. Hu, and N. K. Dutta, "All-optical latches based on two-photon absorption in semiconductor optical amplifiers," J. of Opt. Soc. Am. B 29 (9), 2603-2609 (2012)

4. H. Hu, **W. Li**, S. Ma, and N. K. Dutta, "Coherence Properties of Supercontinuum Generated in Dispersion-Tailored Lead-Silicate Microstructured Fiber Taper," Fiber and Integrated Optics, 32 (3), 209-221 (2013)

5. H. Hu, **W. Li**, and N. K. Dutta, "Supercontinuum generation in dispersion-managed tapered-rib waveguide," Applied Optics, 52 (30), 7336-7341 (2013)

6. **W. Li,** H. Hu, and N. K. Dutta, "High speed all-optical encryption and decryption using quantum dot semiconductor amplifiers," Journal of Modern Optics, 60 (20),1741-1749, (2013)

7. H. Hu, **W. Li,** and N. K. Dutta, "Dispersion-engineered tapered planer waveguide for coherent supercontinuum generation," Opt Commun., 324, 252-257, (2014)

8. H. Hu, **W. Li,** X. Zhang, and N. K. Dutta, "Octave Spanning Mid-IR Supercontinuum Generation in Dispersion-Varying Planar Waveguides", 54, 3448-3454, Applied Optics, (2015)

9. X. Zhang, **W. Li**, H. Hu, and N. K. Dutta, "High speed all-optical encryption and

decryption based on two-photon absorption in semiconductor optical amplifiers" Journal of Optical Communications and Networking, 7(4), 276-285, (2015)

10. **W. Li**, H. Hu, X. Zhang, and N. K. Dutta, "High Speed all optical logic gates using binary phase shift keyed signal based On QD-SOA", International Journal of High Speed Electronics and Systems, 24, 150005, (2015)

Reference

Chapter 1

[1] F. P. Kapron, D.B. Keck, and R.D. Maurer, “Radiation losses in glass optical waveguides”, *Appl. Phys. Lett*. 17, 423 (1970).

[2] I. Hayashi, M. B. Panish, P. W. Foy, and S. Sumski, “Junction lasers which operate continuously at room temperature”, *Appl. Phys. Lett*. **17**, 109 (1970).

[3] R. J. Sanferrare, “Terrestrial Lightwave Systems”, *AT&T Tech. J*. **66**, 95 (1987)

[4] D. Gloge, A. Albanese, C. A. Burrus, *et al*, “High-speed digital lightwave communication using LEDs and PIN photodiodes at 1.3μm” *Bell Syst. Tech. J.* 59, 1365 (1980).

[5] G.P. Agrawal, Fiber-optic communication systems, John Wiley & Sons (2002).

[6] H. J. S. Dorren, M. T. Hill, Y. Liu, N. Calabretta, A. Srivatsa, F. M. Huijskens, H. de Waardt, and G. D. Khoe, “Optical packet switching and buffering by using all-optical signal processing methods,” *J. Lightw. Technol.*, vol. 21, no. 1, 2-12 (2003)

Chapter 2

[1] J. Kim, Y. Jhon, Y. Byun, S. Lee, D. Woo, and S. Kim, “All-optical XOR gate using semiconductor optical amplifiers without additional input beam,” IEEE Photon. Technol. Lett. **14**(10), 1436-1438 (2002).

[2] Q. Wang, G. Zhu, H. Chen, J. Jaques, J..Leuthold, A. B. Piccirilli, and N.K. Dutta, “Study of all-optical XOR using Mach-Zehnder interferometer and differential scheme,” IEEE J. Quantum Electron. **40**(6), 703-710 (2004).

[3] T. Houbavlis, K. Zoiros, A. Hatziefremidis, H. Avramopoulos, L. Occhi, G. Guekos, S. Hansmann, H. Burkhard, and R. Dall' Ara, "10 Gbit/s all-optical Boolean XOR with SOA fiber Sagnac gate," Electron. Lett. **35**(19), 1650 (1999).

[4] C. Bintjas, M. Kalyvas, G.Theophilopoulos, T. Stathopoulos, H. Avramopoulos, L.Occhi, L. Schares, G. Guekos, S. Hansmann, and R. Dall' Ara, "20Gb/s all optical XOR with UNI gate," IEEE Photon. Technol. Lett. **12**(7), 834-836 (2000).

[5] K, Chan, C. Chan, L. Chen, and F. Tong, "Demonstration of 20Gb/s all-optical XOR gate by four-wave mixing in semiconductor optical amplifier with RZ-DPSK modulated inputs," IEEE Photon. Technol. Lett. **16**(3), 897-899 (2004).

[6] Z. Li, Y. Liu, S. Zhang, H. Ju, H. de Waardt, G. D. Khoe, H.J. S. Dorren, and D. Lenstra, "All-optical logic gates using semiconductor optical amplifier assisted by optical filter," Electron. Lett. **41**(25), 1397 (2005).

[7] R. Webb, R. Manning, G. Maxwell, A. Poustie, "40 Gbit/s all-optical XOR gate based on hybrid-integrated Mach-Zehnder interferometer," Electronics Letters. 39(1), 79-81 (2003)

[8] S. Diez, C. Schubert, R. Ludwig, H. Ehrke, "160 Gbit/s all-optical demultiplexing using hybrid gain-transparent SOA Mach-Zehnder interferometer," Electronics Letters. 36(17), 1484-1486 (2000).

[9] T. Berg, and J. Mork, "Saturation and noise properties of quantum-dot optical amplifier," IEEE J. Quantum Electron. **40**(11), 1527-1539 (2004).

[10] P. Reithmaier, and G. Eisenstein, "Semiconductor optical amplifiers with nanostructured gain material," in *Frontiers in Optics*, OSA Technical Digest (CD) (Optical Society of America, 2008), paper FTuN1.

[11] P. Borri, and W. Langbein, J. M. Hvam, F. Heirichsdorff, M. H. Mao and D. Bimberg, "Ultrafast gain dynamics in InAs-InGaAs quantum-dot amplifiers," IEEE J. Quantum Electron. **12**, 594 (2000). Also, "Spectral hole-burning and carrier-heating dynamics in quantum-dot amplifiers: comparison with bulk amplifiers," Phys. Stat. Solidi. B **224**(2), 419-423 (2001).

[12] B. Lu, P. Yin, C. Lu and J. Cheng, "Binary optical switch and programmable optical logic gate based on the integration of GaAs/AlGaAs surface-emitting lasers and heterojunction phototransistors," IEEE Photon. Technol. Lett. 6(3), 398-401 (1994).

[13] S. Tripathy, S. Sahu, C. Mohapatro, S. Dash, "Implementation of optical logic gates using closed packed 2D-photonic crystal structure," Optics Communications, 285, 3234-3237 (2012).

[14] T. Akiyama, M. Sugawara and Y. Arakawa, "Quantum dot semiconductor optical amplifiers," Proc. of the IEEE, 95 (9), 1757-1766 (2007).

[15] N. Yasuoka, K. Kawaguchi, H. Ebe, T. Akiyama, M. Ekawa, K. Morito, M. Sugawara and Y. Arakawa, "Quantum-dot semiconductor optical amplifiers with polarization-independent gains in 1.5μm wavelength band", IEEE Photon. Technol. Lett. 20, 1908-1910 (2008).

[16] K. Mukai, Y. Nakata, H. Shoji, M. Sugawara, K. Ohtsubo, N. Yokoyama, and H. Ishikawa, "Lasing with low threshold current and high output power from columnar-shaped InAs-GaAs quantum dots." Electron. Lett. **34**(16), 1558 (1998).

[17] T. Akiyama, O. Wada, H. Kuwatsuka, T. Simoyama, Y. Nakata, K. Mukai, M. Sugawara, and H.Ishikawa, "Nonlinear processes responsible for non-degenerate four-wave mixing

in quantum dot optical amplifiers," Appl. Phys. Lett. **77**(12), 1753 (2000).

[18] T. Berg, S. Bischoff, I. Magnusdottir, and J. Mork, "Ultrafast gain recovery and modulation limitations in self-assembled quantum-dot devices," IEEE Photon. Technol. Lett. **13**(6), 541-543 (2001).

[19] J. Kim, and S. Chuang, "Small-signal cross-gain modulation of quantum-dot semiconductor optical amplifiers," IEEE J. Quantum Electron. **18**, 2538 (2006).

[20] T. Berg, and J. Mork, "Quantum dot amplifiers with high output power and low noise." Appl. Phys. Lett. **82**(18), 3083 (2003).

[21] S. Ma, H. Sun, Z. Chen, and N.K. Dutta, "High speed all-optical PRBS generation based on quantum-dot semiconductor optical amplifiers," Opt. Express **17**(21), 18469-18477 (2009).

[22] T. Akiyama, H. Kuwatsuka, T. Simoyama, Y. Nakata, K. Mukai, M. Sugawara, O. Wada, and H. Ishikawa, "Application of spectral-hole burning in the inhomogeneous broadened gain of self-assembled quantum dots to a multi-wavelength channel nonlinear optical device," IEEE Photonic. Tech. Letts. Vol. 12, 1301-1303 (2000).

[23] P. Borri, W. Langbein, F. Heinrichsdorff, M.-H. Mao, and Dieter Bimberg "Spectral Hole-Burning and Carrier-Heating Dynamics in InGaAs Quantum-Dot Amplifiers" IEEE, Selected topics in Quant. Elect. Vol. 6, 544-551 (2000).

[24] H. Dong, H. Sun, Q. Wang, N. K. Dutta, and J.Jaques, "All-optical logic AND operation at 80 Gb/s using semiconductor optical amplifier based on the Mach-Zehnder interferometer," Microw. Opt. Technol. Lett. **48**(8), 1672-1675 (2006).

[25] W. Li, S. Ma, H. Hu, and N. K. Dutta, "All-optical latches using quantum-dot

semiconductor optical amplifier", Opt Commun., 285 (24), 5138-5143 (2012).

[26] J.M. Vazquez, H. H. Nilsson, J. Zhang, and I. Galbraith, "Linewidth enhancement factor of quantum-dot optical amplifiers," IEEE J. Quantum Electron. **42**(10), 986-993 (2006).

[27] O. Qasaimeh, "Linewidth enhancement factor of quantum-dot lasers," Opt. Quantum Electron. **37**(5), 495-507(2005).

[28] G. P. Agrawal, Fiber-Optic Communication System, 3rd ed. Wiley, (2002).

Chapter 3

[1] J. Kim, Y. Jhon, Y. Byun, S. Lee, D. Woo, and S. Kim, "All-optical XOR gate using semiconductor optical amplifiers without additional input beam," IEEE Photon. Technol. Lett. 14(10), 1436-1438 (2002).

[2] Q. Wang, G. Zhu, H. Chen, J. Jaques, J..Leuthold, A. B. Piccirilli, and N.K. Dutta, "Study of all-optical XOR using Mach-Zehnder interferometer and differential scheme," IEEE J. Quantum Electron. **40**(6), 703-710 (2004).

[3] T. Houbavlis, K. Zoiros, A. Hatziefremidis, H. Avramopoulos, L. Occhi, G. Guekos, S. Hansmann, H. Burkhard, and R. Dall' Ara, "10 Gbit/s all-optical Boolean XOR with SOA fiber Sagnac gate," Electron. Lett. **35**(19), 1650 (1999).

[4] C. Bintjas, M. Kalyvas, G.Theophilopoulos, T. Stathopoulos, H. Avramopoulos, L.Occhi, L. Schares, G. Guekos, S. Hansmann, and R. Dall' Ara, "20Gb/s all optical XOR with UNI gate," IEEE Photon. Technol. Lett. **12**(7), 834-836 (2000).

[5] K, Chan, C. Chan, L. Chen, and F. Tong, "Demonstration of 20Gb/s all-optical XOR gate

by four-wave mixing in semiconductor optical amplifier with RZ-DPSK modulated inputs," IEEE Photon. Technol. Lett. **16**(3), 897-899 (2004).

[6] Z. Li, Y. Liu, S. Zhang, H. Ju, H. de Waardt, G. D. Khoe, H.J. S. Dorren, and D. Lenstra, "All-optical logic gates using semiconductor optical amplifier assisted by optical filter," Electron. Lett. **41**(25), 1397-1399 (2005).

[7] A. V. Uskov, T. W. Berg, J. Mork, "Theory of pulse-train amplification without patterning effects in quantum-dot semiconductor optical amplifiers," IEEE J. Quantum Electron. 40, 306-320 (2004).

[8] T. Akiyama, M. Sugawara, "Quantum-dot semiconductor optical amplifiers," Proc. IEEE 95, 1757-1766 (2007).

[9] H. Sun, Q. Wang, H. Dong, N.K. Dutta, "XOR performance of a quantum dot semiconductor optical amplifier based Mach-Zehnder interferometer," Opt. Express 13, 1892-1899 (2005).

[10] W. Li, H. Hu, and N. K. Dutta, "High speed all-optical encryption and decryption using quantum dot semiconductor optical amplifiers," Journal of Modern Optics 60.20 (2013): 1741-1749.

[11] H. J.S. Dorren, X. Yang, A. K. Mishra, Z. Li, H. Ju, H. de-Waardt, G. D. Khoe, T. Simoyama, H. Ishikawa, H. Kawashima, T. Hasama, "All-optical logic based on ultrafast gain and index dynamics in a semiconductor optical amplifier," IEEE J. Sel. Top. Quantum Electron. 10, 1079-1092 (2004).

[12] H. J.S. Dorren, X. Yang, D. Lenstra, H. de Waart, G. D. Khoe, T. Simoyama, H. Ishikawa, H. Kawashima, T. Hasama, "Ultrafast refractive-index dynamics in a multiquantum-well

semiconductor optical amplifier," IEEE Photonics Technol, Lett. 15, 792-794 (2003).

[13] M. Y. Hong, Y. H. Chang, A. Dienes, J.P. Heritage, P. J. Delfyett, S. Dijaili, F. G. Patterson, "Femtosecond self-and cross-phase modulation in semiconductor laser amplifier," IEEE J. Sel. Top. Quantum Electron. 2, 523-539 (1996).

[14] H. Folliot, M. Lynch, A. L. Bradley, T. Krug, L.A. Dunbar, J. Hegarty, J. F. Donegan, "Two-photon-induced photoconductivity enhancement in semiconductor microcavities: a theoretical investigation," J. Opt. Soc. Am. B 19, 2396-2402 (2002).

[15] H. Dong, H. Sun, Q. Wang, N.K. Dutta, and J. Jaques, "All-optical logic AND operation at 80 Gb/s using semiconductor optical amplifier based on the Mach-Zehnder interferometer, " Microwave and. Opt. Technol Lett. 48(8), 1672-1675 (2006).

[16] N.K. Dutta, Q. Wang, Semiconductor Optical Amplifiers, World Scientific, 2006.

[17] A. Meccozi, J. Mork, "Saturation effects in nondegenerate four-wave mixing between short optical pulses in semiconductor laser amplifiers," IEEE J. Sel. Top. Quantum Electron. 3, 1190-1207 (1997).

Chapter 4

[1] K. E. Stubkjaer, "Semiconductor optical amplifier-based all-optical gates for high-speed optical processing," IEEE J. Sel. Top. Quantum Electron. 6, 1428-1435 (2000).

[2] S.W. Golomb, "*Shift Register Sequences*," Holden-Day, (San Francisco, 1967).

[3] K. E. Zoiros, T. Houbavlis and M. Kalyvas. "Ultra-high speed all-optical shift registers and their applications in OTDM networks," Invited paper, Optical and Quantum

Electronics, 36 (11), 1005-1053 (2004).

[4] J.M. Senior, *Optical Fibre Communications* – Principles and Practice, (Prentice-Hall, London, 1985).

[5] T. Houbavlis, K. Zoiros, A. Hatziefremidis, H. Avramopoulous, L. Occhi, G. Guekos, S. Hansmann, H. Burkhard and R. Dall'Ara, "10 Gbit/s all-optical Boolean XOR with SOA fiber Sagnac gate", Electron. Lett. **35**, 1650-1652 (1999).

[6] C. Bintjas, M. Kalyvas, G. Theophilopoulos, T. Stathopoulos, H. Avramopoulous, L. Occhi, L. Schares, G. Guekos, S. Hansmann and R. Dall'Ara, " 20 Gb/s all-optical XOR with UNI gate," IEEE Photon. Technol. Lett. **12**, 834-836 (2000).

[7] T. Fjelde, D. Wolfson, A. Kloch, B. Dagens. A. Coquelin, I. Guillemot, F. Gaborit, F. Poingt and M. Renaud, "Demonstration of 20 Gbit/s all-optical logic XOR in integrated SOA-based interferometric wavelength converter", Electron. Lett., **36** (22), 1863-1864 (2000).

[8] H. Chen, G. Zhu, J. Jaques, J. Leuthold, A. B. Piccirilli, N. K. Dutta "All-optical logic XOR using a differential scheme and Mach-Zehnder interferometer" Electron. Lett. 38, 1271-1273 (2002).

[9] H. Sun, Q. Wang, H. Dong, D. K. Dutta, "XOR performance of a quantum dot semiconductor optical amplifier based Mach Zehnder interferometer" Opt. Express, 13(6), 1892-1899, (2005).

[10] Y. B. Ezra, B. I. Lembrikov and M. Haridim, "Ultrafast all-optical processor based on quantum-dot semiconductor optical amplifiers", IEEE J. Quantum Electron. 45, 34-41 (2009).

[11] H. Han, M. Zhang, P. Ye and F. Zhang, “Parameter design and performance analysis of a ultrafast all-optical XOR gate based on quantum dot semiconductor optical amplifiers in nonlinear mach-zehnder interferometer,” Opt. Commun., 281, 5140-5145 (2008).

[12] M. Sugawara, H. Ebe, N. Hatori, M. Ishida, Y. Arakawa, T. Akiyama, K. Otsubo, and Y. Nakata “Theory of optical signal amplification and processing by quantum-dot semiconductor optical amplifiers,” Phys. Rev. B **69**, 235332 (2004).

[13] H. Dong, H. Sun, Q. Wang, N. K. Dutta, and J.Jaques, “All-optical logic AND operation at 80 Gb/s using semiconductor optical amplifier based on the Mach-Zehnder interferometer,” Microw. Opt. Technol. Lett. **48**(8), 1672-1675 (2006).

[14] M. Kalyvas, K. Yiannopoulous, T. Houbavlis, and H. Avramopoulous, “Design algorithm of all optical linear feedback shift registers” Int. J. Electron. Commun., **57**, 328-332 (2003).

[15] N. K. Dutta, Q. Wang, Semiconductor optical amplifier, (World Scientific, Singapore, 2006).

[16] Churchhouse, Robert, *Codes and Ciphers: Julius Caesar, the Enigma and the Internet*, (Cambridge University Press,2002).

[17] Bruce Schneier, *Applied cryptography*, (John Wiley & Sons, Inc, 1996).

[18] K. Mukai, Y. Nakata, H. Shoji, M. Sugawara, K. Ohtsubo, N. Yokoyama and H. Ishikawa, “Lasing with low threshold current and high output power from columnar-shaped InAs-GaAs quantum dots,” Electron. Lett. **34**, 1588 (1998).

[19] T. Akiyama and O. Wada, “Nonlinear processes responsible for nondegenerate four-wave mixing in quantum-dot optical amplifiers”, App. Phys. Lett., **77**(12), 1753 (2000).

[20] T. Akiyama, M. Sugawara, and Y. Arakawa, “Quantum-dot semiconductor optical amplifiers”, Proceedings of the IEEE, **95(9)**, 1757, (2007).

[21] P. Ridha, L. Li, M. Rossetti, G. Patriarche, A. Fiore, “Polarization dependence of electroluminescence from closely-stacked and columnar quantum dots,” Opt. Quantum. Electron. 40(2-4), 239-248 (2008).

[22] T. Berg, S. Bischoff, I. Magnusdottir and J. Mork, “Ultrafast Gain Recovery and Modulation limitations in Self-Assembled Quantum-Dot Devices”, IEEE Photon. Tech. Lett., 13, 541 (2001).

[23] J. Kim and S. L. Chuang, “Small-signal cross-gain modulation of quantum-dot semiconductor optical amplifiers,” IEEE Photon. Technol. Lett. **18**, 2538-2540 (2006).

[24] P. Borri, W. Langbein, J. M. Hvam, F. Heirichsdorff, M. Mao and D. Bimberg, “Spectral Hole-Burning and Carrier-Heating Dynamics in Quantum-Dot Amplifiers: Comparison with Bulk Amplifiers”, Phys. Stat. Solidi. B, 224(2), 419-423, (2001).

[25] T. Akiyama, H. Kuwatsuka, T. Simoyama, Y. Nakata, K. Mukai, M. Sugawara, O. Wada and H. Ishikawa, “Appllication of Spectral-Hole Burning in the Inhomogeneous Broadened Gain of Self-Assembled Quantum Dots to a Multiwavelength-Channel Nonlinear Optical Device”, IEEE Photonics Technology Letters, 12, 1301, (2000).

[26] J. M. Vazquez, H. H. Nilsson, J. Zhang and I. Galbraith, “Linewidth enhancement factor of quantum-dot optical amplifiers”, IEEE J. Quantum Electron., 42, 986, (2006).

[27] O. Qasaimeh, “Linewidth enhancement factor of quantum-dot lasers”, Opt. Quant. Electron., 37, 495, (2005).

[28] W. Li, H. Hu, and N. K. Dutta, “High speed all-optical encryption and decryption using

quantum dot semiconductor amplifiers," Journal of Modern Optics,60 (20),1741-1749, (2013).

[29] A. Uskov, E. O'Reilly, M. Laemmlin, N. Ledentsov, and D. Bimberg, "On gain saturation in quantum dot semiconductor optical amplifiers," Opt. Commun. 248(1-3), 211-219 (2005).

Chapter 5

[1] G. P. Agrawal, Fiber-Optic Communication System, 3rd ed. Wiley, (2002).

[2] J. Kim, Y. Jhon, Y. Byun, S. Lee, D. Woo, and S. Kim, " All-optical XOR gate using semiconductor optical amplifiers without additional input beam," IEEE Photon. Technol. Lett. 14 (10), 1436-1438 (2002).

[3] Q. Wang, G. Zhu, H.Chen, J. Jaques, J. Leuthold, A. B. Piccirilli, and N. K. Dutta, "Study of all-optical XOR using Mach-Zehnder interferometer and differential shceme," IEEE J. Quantum Electron. Lett. 35(19), 1650 (1999).

[4] T. Houbavlis, K. Zoiros, A. Hatziefremidis, H. Avramopoulous, L. Occhi, G. Guekos, S. Hansmann, H. Burkhard and R. Dall'Ara, "10 Gbit/s all-optical Boolean XOR with SOA fiber Sagnac gate", Electron. Lett. **35**, 1650-1652 (1999).

[5] C. Bintjas, M. Kalyvas, G. Theophilopoulos, T. Stathopoulos, H. Avramopoulous, L. Occhi, L. Schares, G. Guekos, S. Hansmann and R. Dall'Ara, " 20 Gb/s all-optical XOR with UNI gate," IEEE Photon. Technol. Lett. **12**, 834-836 (2000).

[6] K, Chan, C. Chan, L. Chen, and F. Tong, "Demonstration of 20Gb/s all-optical XOR gate

by four-wave mixing in semiconductor optical amplifier with RZ-DPSK modulated inputs," IEEE Photon. Technol. Lett. 16(3), 897-899(2004).

[7] Z. Li, Y. Liu, S. Zhang, H. Ju, H. de Waardt, G. D. Khoe, H.J. S. Dorren, and D. Lenstra, "All-optical logic gates using semiconductor optical amplifier assisted by optical filter," Electron. Lett. 41(25), 1397 (2005).

[8] T. Akiyama, M. Sugawara, and Y. Arakawa, "Quantum-dot semiconductor optical amplifiers," Proc. IEEE 95(9), 1757-1766 (2007).

[9] T. Berg, and J. Mork, "Saturation and noise properties of quantum-dot optical amplifier," IEEE J. Quantum Electron. **40**(11), 1527-1539 (2004).

[10] P. Reithmaier, and G. Eisenstein, "Semiconductor optical amplifiers with nanostructured gain material," in Frontiers in Optics, OSA Technical Digest (CD) (Optical Society of America, 2008), paper FTuN1.

[11] P. Borri, and W. Langbein, J. M. Hvam, F. Heirichsdorff, M. H. Mao and D. Bimberg, "Ultrafast gain dynamics in InAs-InGaAs quantum-dot amplifiers," IEEE J. Quantum Electron. 12, 594 (2000).

[12] P. Borri, W. Langbein, J. M. Hvan, F. Heirichsdorff, M. Mao, and D. Bimberg, "Spectral hole-burning and carrier-heating dynamics in quantum-dot amplifiers: comparison with bulk amplifiers," Phys. Stat. Solidi. B 224(2), 419-423 (2001).

[13] W. Li, S. Ma, H. Hu, and N. K. Dutta, "All optical latches using quantum dot semiconductor optical amplifier," Optics Communications, 285 (24), 5138-5143 (2012).

[14] I.Kang, C. Dorrer, L. Zhang, M. Rasras, L. Buhl, A. Bhardwaj, S. Cabot, M. Dinu, X. Liu, M. Cappuzzo, L. Gomez, A.Wong-Foy, Y. F. Chen, S. Patel, D. T. Neilson, J. Jacques, C.

R. Giles, “Regenerative all optical wavelength conversion of 40-Gb/s DPSK signals using a semiconductor optical amplifier Mach-Zehnder interferometer,” ECOC 2005, paper Th4.3.3 (2005).

[15] I.Kang, C. Dorrer, Z. Liming, M. Dinu, M. Rasras, L. Buhl, S. Cabot, A. Bhardwaj, L. Xiang, M. A.Cappuzzo, L. Gomez, A. Wong-Foy, Y. F. Chen, N. K. Dutta, S. S. Patel, D. T. Neilson, C. R. Giles, A. Piccirilli, and J. Jaques, “Characterization of the dynamical processes in all-optical signal processing using semiconductor optical amplifiers,” IEEE J. Sel. Top. Quantum Electron. 14, 758-769 (2008).

[16] M. Kalyvas, K. Yiannopoulous, T. Houbavlis, and H. Avramopoulous, “Design algorithm of all optical linear feedback shift registers” Int. J. Electron. Commun., 57, 328-332 (2003).

[17] M. Sugawara, H. Ebe, N. Hatori, M. Ishida, Y. Arakawa, T. Akiyama, K. Otsubo, and Y. Nakata “Theory of optical signal amplification and processing by quantum-dot semiconductor optical amplifiers,” Phys. Rev. B 69, 235332 (2004).

[18] K. Mukai, Y. Nakata, H. Shoji, M. Sugawara, K. Ohtsubo, N. Yokoyama and H. Ishikawa, “Lasing with low threshold current and high output power from columnar-shaped InAs-GaAs quantum dots,” Electron. Lett. **34**, 1588 (1998).

[19] T. Akiyama and O. Wada, “Nonlinear processes responsible for nondegenerate four-wave mixing in quantum-dot optical amplifiers”, App. Phys. Lett., 77(12), 1753 (2000).

[20] P. Ridha, L. Li, M. Rossetti, G. Patriarche, A. Fiore, “Polarization dependence of electroluminescence from closely-stacked and columnar quantum dots,” Opt. Quantum. Electron. 40(2-4), 239-248 (2008).

[21] T. Berg, S. Bischoff, I. Magnusdottir and J. Mork, “Ultrafast Gain Recovery and Modulation limitations in Self-Assembled Quantum-Dot Devices”, IEEE Photon. Tech. Lett., 13, 541 (2001).

[22] J. Kim and S. L. Chuang, “Small-signal cross-gain modulation of quantum-dot semiconductor optical amplifiers,” IEEE Photon. Technol. Lett. **18**, 2538-2540 (2006).

[23] T. Akiyama, H. Kuwatsuka, T. Simoyama, Y. Nakata, K. Mukai, M. Sugawara, O. Wada and H. Ishikawa, “Appllication of Spectral-Hole Burning in the Inhomogeneous Broadened Gain of Self-Assembled Quantum Dots to a Multiwavelength-Channel Nonlinear Optical Device”, IEEE Photonics Technology Letters, 12, 1301, (2000).

[24] J. M. Vazquez, H. H. Nilsson, J. Zhang and I. Galbraith, “Linewidth enhancement factor of quantum-dot optical amplifiers”, IEEE J. Quantum Electron., 42, 986, (2006).

[25] O. Qasaimeh, “Linewidth enhancement factor of quantum-dot lasers”, Opt. Quant. Electron., 37, 495, (2005).

[26] A. Uskov, E. O’Reilly, M. Laemmlin, N. Ledentsov, and D. Bimberg, “On gain saturation in quantum dot semiconductor optical amplifiers,” Opt. Commun. **248**(1-3), 211-219 (2005).

[27] W. Li, H. Hu, N.K. Dutta, “High speed all-optical encryption and decryption using quantum dot semiconductor optical amplifiers” Journal of Modern Optics, Vol.20, 1741-1749 (2013).

Chapter 6

[1] Y. Hibino, “Photonic integration technologies for large-capacity telecommunication networks”, IEEE Photon. J., 2, 2, 269-272 (2010).

[2] H. Takara, S. Kawanishi, M. Sarawatari, and K. Noguchi, “Generation of highly stable 20GHz transform-limited optical pulses from actively mode-locked Er-doped fiber lasers with an all-polarization maintaining ring cavity”, *Electron. Lett.*, vol. 28, no. 22, 2095-2096 (1992).

[3] X. Shan and D. M. Apirit, “Novel method to suppress noise in harmonically mode-locked erbium fiber lasers”, *Electron. Lett.*, vol. 29, no. 11, 979-981(1993).

[4] C. Wu and N. K. Dutta, “High-repetition-rate optical pulse generation using a rational harmonic mode-locked fiber laser”, Journal of Quantum Electronics, vol. 36, no. 2, 145-150(2000).

[5] M. N. Vinoj and V. C. Kuriakose, “Generation of pedestal-free ultrashort soliton pulses and optimum dispersion profile in real dispersion-decreasing fibre”, J. of Opt. A: Pure and Appl. Optics, 6, 1, 63-70 (2004).

[6] G. R. Lin, Y. C. Lin, K. C. Lin, W. Y. Lee and C. L. Wu, “50 fs soliton compression of optical clock pulse recovered from NRZ data injected SOAFL”, Opt. Express, 18, 9, 9525-9530 (2010).

[7] K. Taira and K. Kikuchi, “Subpicosecond pulse generation using an electroabsorption modulator and double-stage pulse compressor”, IEEE Photon. Technol. Lett., 15, 9, 1288-1290 (2003).

[8] K. Taira and K. Kikuchi, “Picosecond pulse generation with high extinction ratio employing electroabsorption modulator, fiber compressor and self-phase modulation-based reshaper,” Electron. Lett., 40, 1, 15-16 (2004).

[9] Y. Ozeki, S. Takasaka, T. Inoue, K. Igarashi, J. Hiroishi, R. Sugizaki, M. Sakano and S. Namiki, “Nearly exact optical beat-to-soliton train conversion based on comb-like profiled fiber emulating a polynomial dispersion decreasing profile,” IEEE Photon. Technol. Lett., 17, 8, 1698-1700 (2005).

[10] Y. Ozeki, S. Takasaka, J. Hiroishi, R. Sugizaki, T. Yagi,M. Sakano and S. Namiki, “Generation of 1 THz repetition rate, 97 fs optical pulse train based on comb-like profiled fibre,” Electron. Lett., 41, 19, 1048-1050 (2005).

[11] C. De Dios and H. Lamela, “Compression and Reshaping of Gain-Switching Low-Quality Pulses Using a Highly Nonlinear Optical Loop Mirror,” IEEE Photon. Technol. Lett., 22, 6, 377-379 (2010).

[12] M. D. Pelusi, Y. Matsui, and A. Suzuki, “Pedestal suppression from compressed femtosecond pulses using a nonlinear fiber loop mirror,” IEEE J. of Quantum Electron., 35, 6, 867-874 (1999).

[13] K. Smith, N. J. Doran and P. G. J. Wigley, “Pulse shaping, compression and pedestal suppression employing a nonlinear-optical loop mirror,” Opt. Lett., 15, 22, 1294-1296 (1990).

[14] S. Yamashita, “A tutorial on nonlinear photonic applications of carbon nanotube and graphene,” J. Lightwave Technol. 30(4), 427-447 (2012).

[15] B.V. Cunning, C. L. Brown, and D. Kielpinski, “Low-loss flake-graphene saturable absorber mirror for laser mode-locking at sub-200-fs pulse duration,” Appl. Phys. Lett. 99(26), 261109(2011).

[16] G. Sobon, J. Sotor, and K. M. Abramski, “All-polarization maintaining femtosecond Er-doped fiber laser mode-locked by graphene saturable absorber,” Laser Phys. Lett. 9(8), 581-586(2012).

[17] D. Popa, Z. Sun, F. Torrisi, T. Hasan, F. Wang, and A. C. Ferrara, “Sub 200fs pulse generation from a graphene mode-locked fiber laser,” Appl. Phys. Lett. 97(20), 203106 (2010).

[18] J. Xu, S. Wu, H. Li, J. Liu, R. Sun, F. Tan, H. Yang, and P. Wang, “Dissipative solition generation from a graphene oxide mode-locked Er-doped fiber laser,” Opt. Express. 20(21), 23653-23658(2012).

[19] Z.B. Liu, X. He, and D. N. Wang, “Passively mode-locked fiber laser based on a hollow-core photonic crystal fiber filled with few-layered graphene oxide solution,” Opt. Lett. 36(16), 3024-3026(2011).

[20] Y. H. Lin and G.-R. Lin, “Kelly sideband variation and self four-wave-mixing in femtosecond fiber soliton laser mode-locked by multiple exfoliated graphite nano-particles,” Laser Phys. Lett. 10(4), 045109 (2013).

[21] V. V. Singh, G. Gupta, A. Batra, A. K. Nigam, M. Boopathi, P. K. Gutch, B. K. Tripathi, A. Srivastava, M. Samuel, G. S. Agarwal, B. Singh, and R. Vijayaraghava, “Greener electrochemical synthesis of high quality graphene nanosheets directly from pencil and its SPR sensing application,” Adv. Funct. Mater. 22(11), 2352-2362(2012).

[22] Y. H. Lin, Y. C. Chi, and G.-R. Lin, “Nanoscale charcoal powder induced saturable absorption and mode-locking of a low-gain erbium-doped fiber-ring laser,” Laser Phys. Lett. 10(5), 055105 (2013)

[23] N. K. Dutta, “ Fiber amplifiers and fiber lasers”, World Scientific (2014)

[24] Y. H. Lin, Y. C. Chi, and G-R. Lin, “Nanoscale charcoal powder induced saturable absorption and mode-locking of a low-gain erbium-doped fiber-ring laser,” Laser Phys. Lett. 10(5), 055105(2013)

[25] Z. Q. Li, C. J. Lu, Z. P. Xia, Y. Zhou, and Z. Luo, “X-ray diffraction patterns of graphite and turbostratic carbon,” Carbon 45(8), 1686-1695 (2007)

[26] J. W. Jeon, J. Lee, and J. H. Lee, “Numerical study on the minimum modulation depth of a saturable absorber for stable fiber laser mode locking,” J. Opt. Soc. Am. B, 32(1), 31-37 (2015)

[27] G. P. Agrawal, *Nonlinear fiber optics*, 4th Ed., (Elsevier, 2007)

[28] H. M. Chen, “A study of high repetition rate pulse generation and all-optical add/drop multiplexing,” PhD thesis, Chapter 4, 68 (2002)